

Copyright
by
Kyungjin Ahn
2005

The Dissertation Committee for Kyungjin Ahn
certifies that this is the approved version of the following dissertation:

**The Nature and Consequences of Cosmological Halo
Formation: Dark Matter and the Dark Ages**

Committee:

Paul R. Shapiro, Supervisor

Hugo Martel

Eiichiro Komatsu

Volker Bromm

J. Craig Wheeler

**The Nature and Consequences of Cosmological Halo
Formation: Dark Matter and the Dark Ages**

by

Kyungjin Ahn, B.S.

Dissertation

Presented to the Faculty of the Graduate School of
The University of Texas at Austin
in Partial Fulfillment
of the Requirements
for the Degree of

Doctor of Philosophy

The University of Texas at Austin

December 2005

Dedicated to my family members here and there; Byungsang Ahn, Jeonghee
Hwang, Suejin Ahn, Younga Lee, Byul Ahn and Miriam Sol Ahn

Acknowledgments

First, I am deeply indebted to my wife, Younga, who had an uneasy summer season due to her guilt of having an aging graduate student as her hubby. At this right moment my writing this acknowledgment, she may be preparing warm breakfast for two children. I am guilty of depriving her of all the summer fun.

Younga, I met you only seven years ago, but I should have met you much earlier. When you are away, I think about you. When you are near, I see you. You are my heart, my soul, my canvas, my wine, my potato chip, my sun. I appreciate my Parents-in-law for accepting me as Son-in-law, and supporting me.

I wish to thank Father and Mother, who have raised and guided me on this hostile planet Earth. Hatred and poverty caused by its own inhabitants is the most difficult thing I can bear. Without them, I could not have survived it. Their life was a grand symphony. Now, here is my humble rose to you.

My lovely kids! How pretty (and noisy) you are! Please grow healthy, because you are precious.

My sister Suejin, replacing her brother who escaped from all the hassle in the home country. Let's have So-Ju when I get back.

I wish to thank my advisor and mentor Paul Shapiro. He has taught

me how to be a scientist. I would never forget those moments in the Subway store, where I always enjoyed the ham-and-astronomy sub. It enriched my brain and the stomach. Addicted to that taste, I will be always hungry for science.

I also want to thank my colleagues. Marcelo Alvarez, you always amaze me by your brightness and speed. Hugo Martel, dear connoisseur of music, food, and science. Ilian Iliev, iron chef of astronomy. Eiichiro Komatsu, fast and furious.

Finally I want to thank my friends: Youngho, Jaekwon, Kwangwoon, Woongjae, Insoo, Soyoung, Hwang, Yongbin, Chisup, Sunghwan, Yongsoon, Sora, and all the others. I also thank my friends in the Astronomy department here in Austin, Stephanie, Martin, Shizuka, Jeongeun (who left), Zhu, and all the others. Thank you my friends.

The Nature and Consequences of Cosmological Halo Formation: Dark Matter and the Dark Ages

Publication No. _____

Kyungjin Ahn, Ph.D.

The University of Texas at Austin, 2005

Supervisor: Paul R. Shapiro

Dark matter particles and baryons constitute a significant fraction of the mass of the universe. Dark matter (DM) halos are the scaffolding around which galaxies and clusters are built. They form when the gravitational instability of primordial density fluctuations causes regions which are denser than average to slow their cosmic expansion, recollapse, and virialize. Baryons provide valuable information about the universe by emitting observable electromagnetic waves, while undergoing complicated hydrodynamic and radiative processes. Understanding the role of baryons and dark matter in structure formation is thus a prerequisite for probing the nature of our universe. We describe here our broad attempts to derive and give physical insight to the theory of cosmological structure formation, first by focusing on dark matter halo formation and the nature of dark matter. We show that many of the results of N-body simulations of cosmological structure formation can be easily understood by the “fluid approximation” we have developed, where the usual

fluid conservation equations are used to describe collisionless halo dynamics. We then study the self-interacting dark matter hypothesis by comparing our results to observations of dark-matter dominated halos. We also find that an alternative dark matter candidate, the thermal relic, can be the origin of the “missing” γ -ray background at 1–20 MeV and 511 keV line emission from the Galactic center, if the dark matter particle mass is about 20 MeV. Turning our attention to baryonic structure formation in the high redshift universe, we then use high-resolution cosmological N-body and hydrodynamic simulations of structure formation at high redshift ($z > 6$) to predict the signal of the 21cm line radiation from neutral hydrogen gas in the cosmic “dark ages”, before reionization. We predict that the largest contribution to the 21cm signal is due to gas in collapsed minihalos. Finally, we focus on the radiative feedback effects of the first stars to question whether the second generation star formation is promoted by such feedback effects. We find that such star formation may be promoted as a result of radiation-induced implosion of minihalos in the vicinity of the first stars.

Table of Contents

Acknowledgments	v
Abstract	vii
List of Tables	xiii
List of Figures	xiv
Chapter 1. Introduction	1
Chapter 2. Formation and Evolution of Cold Dark Matter (CDM) Halos	3
2.1 Toward an Analytical Understanding of Cold Dark Matter Halo N-body Simulations	3
2.2 Fluid Approximation	8
2.2.1 Fluid approximation of collisionless CDM dynamics . . .	9
2.3 Halo Formation by Self-Similar Infall	17
2.3.1 Halo formation from scale-free linear perturbations . . .	17
2.3.2 Halo formation from peaks of the Gaussian random noise primordial density fluctuations	19
2.3.3 Self-similar halos: an analytical model for CDM N-body results	20
2.4 Halo Formation by Non-Self-Similar Infall: Mass Assembly History and the Origin of CDM N-body Halo Profiles	26
2.4.1 Models and initial conditions	26
2.4.2 Halted infall model	28
2.4.3 Radial orbits model	31
2.4.4 Fluid approximation model	31
2.4.5 Results	32

Chapter 3. Nature of Dark Matter	35
3.1 Self-Interacting Dark Matter	35
3.1.1 Introduction	35
3.1.2 Fluid approximation of SIDM halos	44
3.1.2.1 The effect of SIDM collisionality	44
3.1.2.2 Shock jump conditions	46
3.1.3 Self-similar model for SIDM halos in the matter-dominated era	47
3.1.3.1 Self-similarity of SIDM halos	47
3.1.3.2 Basic equations and problem solving scheme	48
3.1.4 Self-similar halos with conduction($\varepsilon = 1/6$): an analytical Model for SIDM halos	53
3.1.4.1 Low- Q regime	53
3.1.4.2 High- Q regime	54
3.1.5 Meaning of the collisionality parameter Q	57
3.1.6 Importance of cosmological infall	60
3.1.7 Application	60
3.1.7.1 Collisionality parameter as a function of σ and M	60
3.1.7.2 Comparison with N-body simulation results	63
3.1.7.3 Rotation curve fitting	65
3.1.7.4 High value of σ : Contradiction with SIDM N-body simulation results?	69
3.1.8 Conclusion/Discussion	71
3.2 511keV Dark Matter and the γ -ray background	81
3.2.1 Missing Gamma Ray Background Problem	81
3.2.2 Dark Matter Annihilation Signal?: Galactic Radiation	81
3.2.3 Background from Continuum Annihilation Signal	83
Chapter 4. 21cm Background from the Cosmic Dark Ages	94
4.1 Introduction	94
4.2 The Calculation	97
4.2.1 Physics of 21 cm signal from neutral hydrogen	97
4.2.2 Semi-analytic calculations	99

4.2.3	Numerical Simulations	102
4.2.3.1	Semi-Analytical Calculation of the Halo Contribution	104
4.3	Results	106
4.3.1	Numerical 21 cm Brightness Temperature from Minihalos vs. IGM	106
4.3.2	Refined Estimate of the Simulated Minihalo 21 cm Signal	109
4.3.3	Convergence	112
4.4	Conclusions	113
Chapter 5. Second-Generation Star Formation In the Early Universe		116
5.1	Introduction	116
5.2	1-D spherical, radiation hydrodynamics code with primordial chemistry network	119
5.2.1	Hydrodynamic Conservation Equations	119
5.2.2	Gravity	120
5.2.3	heating / cooling	121
5.2.4	Radiative transfer	124
5.2.4.1	Internal source	124
5.2.4.2	External source	126
5.2.5	Nonequilibrium chemistry	131
5.2.6	Code test	132
5.3	Initial Setup	133
5.4	Result	136
5.4.1	Optically thin limit: case study for initially ionized halo	136
5.4.2	Feedback effect during the lifetime of the source	137
5.4.2.1	I-front trapping	137
5.4.2.2	Formation of the D-type I-front	139
5.4.2.3	Hydrogen Molecule Formation in Front of the I-Front	141
5.4.2.4	Fate of the Neutral Gas After Source Turns Off: Collapse of the Protostellar Region	145
5.4.3	Fate of the Ionized Gas After Source Turns Off: Evolution After Death of the Source	153
5.5	Discussion	155

Appendices	159
Appendix A. Mass - Wavenumber relation	160
Appendix B. Finite Differencing in the 1-D Spherical, Radiation-Hydrodynamics Code	162
B.1 Time Steps	162
B.2 Radiative Rate Coefficients	163
B.3 Nonequilibrium Chemistry	166
B.4 Heating/Cooling and Hydrodynamics	167
Bibliography	169
Index	186
Vita	188

List of Tables

3.1	Central parameters and the shock location for different Q solutions. This table lists the whole range of Q	55
3.2	Best-fitting concentration parameter of the Burkert profile and χ^2/ν . χ^2/ν is normalized by the value found for Q_{th} solution, $(\chi^2/\nu)_{Q_{\text{th}}} = 2.06 \times 10^{-4}$, the minimum.	68

List of Figures

2.1	Self-similar collisionless halo formation for $\varepsilon = 1$: Phase-space diagram of Bertschinger (1985) solution as an illustration of the “skewless distribution” assumption. Along the line A there are a large number of shell-crossings, which are almost symmetric around $\langle v_r \rangle$, and along the line C, as there is only one stream line, it is intrinsically skewless. On the contrary, there are only three stream lines along the line B, so the assumption is not good in the region inside and close to the outermost caustics. Tangential velocity distribution would have a similar behavior when tangential motion is allowed.	13
2.2	Self-similar collisionless halo formation for $\varepsilon = 1$: Comparison of the skewless-fluid approximation to the exact collisionless Bertschinger solution. Solid lines represent the solution obtained from the fluid approximation in the radial direction, while dotted lines represent the collisionless Bertschinger solution. Spikes in the density plot simply represent infinite values, corresponding to caustics, and therefore there is no physical significance in the height of these spikes. However, spikes in the velocity plot are finite and real. Note that solid lines do not represent the $\gamma = 5/3$ fluid Bertschinger solution.	15
2.3	Same as Figure 2.2, but $\varepsilon = 1/6$. Note again that the solid line was not generated from the $\gamma = 5/3$ fluid approximation, but rather from the radial-only fluid approximation described by equations (2.16 - 2.18).	16
2.4	Effective index of the power spectrum ($P(k) \propto k^{n_{\text{eff}}}$) vs. halo mass for the Λ CDM universe. Appendix describes how n_{eff} is calculated. The solid line is derived from the HS approach, which we use in this work. The dotted line is derived from σ_M	21

2.5	Comparison of self-similar halo profile without conduction with N-body results for CDM halos: (top panel) Density (in units of cosmic mean density) vs. radius (in units of current turnaround radius) for similarity solution ($Q = 0$; $\varepsilon = 1/6$) (solid), the best-fitting NFW profile ($c = 3$), Moore profile ($c = 1.6$) and several $\alpha\beta\gamma$ profiles ($\alpha = 1$, $\beta = 3$) for different values of γ , $\gamma = 1.3$ (best fit), 1.02, 1.16, as labeled. Diemand et al. (2004) find N-body results for CDM halos best fit by $(\alpha, \beta, \gamma) = (1, 3, \gamma = 1.16 \pm 0.14)$ (shaded region); (bottom panel) fractional deviation of the N-body results from similarity solution. Note that $\lambda = \lambda_s \simeq 0.09$ corresponds to $r_s = r_{564} \simeq 0.6 r_{200}$	23
2.6	(left) Density profile from halted infall model along with best-fitting NFW profile for this profile at present. Inset in upper-right shows same over much larger range. (right) Evolution of NFW concentration parameter in the halted infall model, compared with empirical relation of Wechsler et al. (2002) for CDM N-body halos. Different line types indicate different ranges $x_{\text{in}} < x < 1$, within which halo was fit to an NFW profile, where $x \equiv r/r_{\text{vir}}$, $r_{\text{vir}} \equiv r_{200}$	27
2.7	Evolution of mass for the radial orbits (top) and fluid approximation (bottom) simulations, compared with the empirical relation of Wechsler et al. (2002) for CDM N-body results. Shown above each are the fractional deviations $\Delta \equiv (M_{\text{exact}} - M)/M$	28
2.8	Density profile at the end of the radial orbit simulation.	29
2.9	(top) Density profile at the end of the isotropic fluid calculation. (bottom) Circular velocity profile.	30
2.10	Evolution of concentration parameter with scale factor in the isotropic fluid calculation.	32
3.1	Similarity solution dimensionless profiles for low- Q regime. $Q = 0$ means “no conduction,” i.e. “adiabatic” post-shock gas. As Q increases, core density decreases and core temperature increases. Dimensionless similarity variables follow the definitions in Bertschinger (1985).	54
3.2	Similarity solution dimensionless profiles for the high- Q regime. Profiles are indistinguishable from those in Figure 3.1, even though the Q values are quite different. The effect of Q is reversed compared to the low- Q regime: as Q increases, core density increases and core temperature decreases.	56

- 3.3 The parameter η versus dimensionless radius λ , where $\eta = \lambda_{\text{mfp}}/(\sqrt{a}H)$, the ratio of mean free path to gravitational scale height, for different values of Q . From top to bottom, each curve corresponds to $Q/Q_{\text{th}} = 1.23 \cdot 10^{-3}, 9.77 \cdot 10^{-3}, 6.16 \cdot 10^{-2}, 1, 17, 59.4,$ and $186,$ respectively. The constant $a = 2.26.$ 58
- 3.4 Number of scattering that an SIDM particle experiences during the age of the universe in dimensionless radius λ . From bottom to top, each curve corresponds to $Q/Q_{\text{th}} = 1.23 \cdot 10^{-3}, 9.77 \cdot 10^{-3}, 6.16 \cdot 10^{-2}, 1, 17, 59.4,$ and $186,$ respectively. 59
- 3.5 Left: Q vs. mass of halos at their typical formation epoch for different σ . From bottom to top, curves correspond to $\sigma = 0.56, 5.6, 218.5, 1.2 \times 10^4, 2.7 \times 10^4$ respectively. They all correspond to $1\text{-}\sigma_M$ density peaks (σ_M means the standard deviation of the density fluctuations filtered on mass scale M at the collapse epoch); Right: Q vs. mass of halos at their formation epoch for $\nu\text{-}\sigma_M$ ($\nu=1, 2, 3$) fluctuations with $\sigma = 218.5 \text{ cm}^2\text{g}^{-1}$. Cluster-sized halos observed at present will be clustered around the crossing point of the $3\text{-}\sigma_M$ line and $z_{\text{coll}} = 0$ line. 64
- 3.6 Rotation curve fitting. The upper left panel compares several different Q -solutions to the Burkert profile, normalized to r_{564} . The lower left panel shows the best-fitting solution to the Burkert profile, namely the Q_{th} solution. The right panel compares various halo models to the Burkert profile, normalized to r_{max} . It has the Q_{th} profile in r and v in units of $r_{\text{max,Burkert}} = 0.835 r_{564,\text{SIDM}}$ and $v_{\text{max,Burkert}} = 1.01 v_{564,\text{SIDM}}$, respectively, for the same profile as plotted in the lower left panel. In both boxes, the top panel shows the relative difference of a given profile, $(v - v_{\text{Burkert}})/v_{\text{Burkert}}$. The line types of the upper right panel follows the meaning of those in the lower right panel. 67
- 3.7 Comparison of length scales for the $Q = Q_{\text{th}}$ case. The mean free path λ_{mfp} is comparable to the gravitational scale height H in the core region. However, the ratio of the mean free path to the gravitational scale height becomes larger as the radius increases. See also Figure 3.3, which includes other values of $Q.$ 77
- 3.8 Cosmic γ -ray background from dark matter annihilation. The dotted, short-dashed, and long-dashed lines show $m_X = 10, 20,$ and $50 \text{ MeV},$ respectively. The curves which sharply cut off at 511 keV represent background light from line emission (Ahn & Komatsu 2005), while the others which extend to higher energy represent the internal bremsstrahlung. 87

3.9	The total cosmic γ -ray background produced by dark matter annihilation, AGNs (Ueda et al. 2003), and Type Ia supernovae (Ahn et al. 2005). The dotted, short-dashed, and long-dashed lines show $m_X = 10, 20,$ and 50 MeV, respectively. The supernova contribution depends on the observed supernova rate, and we consider the best-fit rate (upper panel) as well as the 2σ upper limit (lower panel). The data points of HEAO-1 A4 MED (Gruber et al. 1999), SMM (Watanabe et al. 1999), and COMPTEL (Kappadath et al. 1996) experiments are also shown.	88
3.10	The best-fit model of the cosmic γ -ray background. The model assumes (a) $m_X = 20$ MeV, (b) the mean dark matter clumping factor is twice as large as predicted by the NFW profile (due to either a steeper profile or the presence of substructures), and (c) line emission is solely produced via positronium formation. The dashed lines show each contribution separately.	89
4.1	Analytical prediction for the mean 21 cm differential brightness temperature due to collisionally-decoupled minihalos and an unperturbed IGM. Shown are the results based on the Press-Schechter (solid) and the Sheth-Tormen (dotted) mass functions for halos and the contribution from the IGM gas with cosmic mean density and temperature (dashed). In the bottom panel we show the minihalo collapse fraction, again based on the Press-Schechter (solid) and the Sheth-Tormen (dotted) mass functions.	101
4.2	Map of the differential brightness temperature δT_b (mK) for the the 21 cm signal obtained from our highest resolution simulation, C4. Rows, top to bottom, show redshifts $z=30, 20,$ and 10 . columns, left to right, represent contributions from minihalos, the IGM and the total signal. Note that the scale is linear for the upper two rows of images, but logarithmic for the bottom row.	105
4.3	21 cm mean brightness temperature evolution. (a)(left) Evolution of the total 21-cm signal vs. redshift. All data points are directly calculated from our simulation box, with the assumption that optical depth is negligible throughout the box and using simulation C4. (b)(right) δT_b vs. redshift below $z = 20$. Plotted are the contributions from minihalos (labeled Halos, circles), the IGM (triangles) and the total (squares).	107
4.4	Semi-analytical minihalo signal vs. IGM signal. The 21 cm flux from each halo in the simulation is found by modeling the halos as described in § 4.2.3.1, to estimate the halo 21 cm signal more accurately. Same notation as in Figure 4.3. The 21 cm minihalo emission increases compared to the raw minihalo signal in figure 4.3. The IGM signal remains the same.	108

4.5	(a)(top) Differential brightness temperature of the 21 cm signal from minihalos for semi-analytical model (dotted: with Press-Schechter mass function; dashed: with Sheth-Tormen mass function), simulation C4 numerical result (squares) and semi-analytical calculation (§ 4.2.3.1) based upon simulation C4 mass function (triangles). (b)(bottom) Minihalo collapse fraction from simulation C4 (squares) and analytical mass functions (linetypes follow those of the top panel).	110
4.6	Differential brightness temperature signals for simulations C1 (squares), C2 (triangles) and C3 (circles) in units of the corresponding signal obtained from simulation C4. Shown are the total (top panel), halos only (middle panel) and IGM only (bottom panel) 21 cm signal.	111
4.7	Relative contributions of minihalos and diffuse IGM gas to the total 21-cm background. The top panel shows the results obtained directly from simulations (C1: triangle, long-dashed; C2: square, short-dashed; C3: pentagon, dotted; C4: circle, solid). The bottom panel shows the results which were semi-analytically refined (§ 4.2.3.1; point- and line-types follow those of the top panel).	114
5.1	Geometry for radiative transfer for an isotropic background of mean intensity $J_\nu(r_{\text{halo}})$ (denoted by $J(\nu)$ in this figure). $\Delta_{jj'k}$, a distance traveled through shell j' by an incoming ray bound for shell j at an angle θ_k , is used to get column densities of various species.	128
5.2	Schematic description of an external source illuminating a target halo at distance D . Geometrical dilution of the flux, if the size of the target halo is much smaller than D , is negligible across the target region, and the flux $F_\nu(r)$ can be approximated as $\frac{L_\nu}{4\pi D^2} e^{-\tau_\nu(>r)}$, where $\tau_\nu(>r)$ is the cumulative optical depth along the line of sight (dashed line) from radius r (point x) to the source (black solid circle on the right). r_{tr} is the truncation radius, or the outermost “edge” of the target halo. . . .	130
5.3	Radial profiles of density and velocity of an initially fully-ionized TIS halo at different times: $t = 0$ (thin solid), t_* (dotted) and $2t_*$ (thick solid).	138
5.4	Radial profiles of x_{H} at time $t = t_* = 2.5$ Myr, for C180 (solid), C360 (dotted), C540 (short-dashed), C1000 (long-dashed) and C5000 (dot-dashed). From this point on, we keep this definition of line types unless otherwise noted. The crossing point of each curve through the thin solid line defines the I-front, where $x_{\text{H}} = 0.5$	140

5.5	Radial profiles of the baryon mass density and the neutral hydrogen abundance at $t = 0.5 t_*$. The existence of the density “bump” ahead of the I-fronts clearly indicates that the I-fronts are D-type. Thin solid lines in both panels represent the initial value at time $t = 0$. Low density in the ionized region is caused by evaporation.	142
5.6	Same as Figure 5.5, but for $t = t_*$	143
5.7	Radial profiles of density, temperature, and H_2 abundance at $t = 0.5 t_*$. Thin solid lines represent the initial value at $t = 0$. H_2 shell formation is universal in all cases.	146
5.8	Same as figure 5.7, but for $t = t_*$	147
5.9	Radial profile of abundance of primordial gas species, for case C540 at $t = 0.5 t_*$. Labels are self-explanatory; electron abundance x_e is represented by the dotted curve, which closely follows the HII abundance. The flux is coming from the right hand side, so this figure can be compared to the mirror image of Figure 3 in Ricotti et al. (2001).	148
5.10	Radial profiles of molecule fraction (top) and the molecule column density (bottom) for case C180 at $t = 0.5 t_*$ (triangle) and at $t = t_*$ (hexagon).	149
5.11	Structure of target halos at their onset of collapse, defined as the first moment when a certain point has reached $\rho_{\text{onset}} \equiv 50\rho_{0,\text{init}}$, where $\rho_{0,\text{init}}$ is the central density at $t = 0$	151
5.12	Onset of collapse (t_{coll}) and the net baryon mass collapsing ($M_{\text{baryon, coll}}$). Note that $t_* = 2.5 \text{ Myr}$ and $M_{\text{baryon, halo}} = 3.3 \times 10^4 M_{\odot}$	152
5.13	Structure of the target halo after the onset of collapse of the neutral core. It is clearly seen that the evaporating wind is detached from the collapsing core. Compare each case to the initial condition (thin solid line). Case C5000 is not plotted here, because the small time step due to the collapsing outer skin (Fig. [5.11]) prevented us from advancing the computation to the degree of central collapse shown in this figure.	154

Chapter 1

Introduction

Our current understanding of the evolution of the universe is based upon the Friedmann-Robertson-Walker (FRW) cosmological model. This “standard” model provides successful explanation of the global, homogeneous and isotropic properties of our universe. On the other hand, strong inhomogeneity exists in relatively small scales, in the form of stars, galaxies, and clusters.

An amazing connection between this local inhomogeneity and the global homogeneity is explained by the inflation scenario. According to the quantum field theory, absolute vacuum or absolute zero energy does not exist, but this vacuum state is full of oscillating “fields”. At the onset of the creation of the universe, a peculiar coexistence of the positive energy and the negative pressure is possible. This condition is suitable to drive an explosive expansion of the universe with the extreme degree of homogeneity and isotropy. At the same time, the oscillating vacuum fluctuations seed a fluctuating density field which can be described in non-quantum mechanical way. Under this initial Gaussian random density fluctuation, newly created dark matter particles and baryons react gravitationally to amplify the fluctuation and ultimately form nonlinear structures we observe today.

Dark matter particles and baryons are the building blocks of the universe, by which cosmological structures form. Understanding the formation and evolution of the cosmological structures is invaluable for probing the nature of our universe as well as providing valuable information for astrophysics. In this dissertation, we describe our broad attempts to understand the cosmological structure formation. In the following Chapters, we describe (1) our analytical model for the cold dark matter structure formation, (2) the effect of the microscopic nature of the dark matter on the structure formation and cosmological background radiation, (3) the 21cm radiation from high redshift cosmological objects, and (4) the local radiative feedback effects of the first stars that are built up by the primordial baryonic species.

Chapter 2

Formation and Evolution of Cold Dark Matter (CDM) Halos

2.1 Toward an Analytical Understanding of Cold Dark Matter Halo N-body Simulations

Numerical N-body simulations of structure formation in the Cold Dark Matter (CDM) universe show a cosmic web of lumps, filaments, and sheets. This web evolves in a self-similar way, with smaller mass structures forming first and merging to form larger-mass structures later, in a continuous sequence of mass assembly. At each epoch, the web produces gravitationally-bound, quasi-spherical “halos” in virial and hydrostatic equilibrium. These virialized halos are the sites of galaxy and cluster formation. Their universal equilibrium structure is a fundamental prediction of the CDM model, but our knowledge is limited to the numerical N-body results, with very little analytical understanding. We shall describe our attempts to fill this gap in what follows.

Most of the progress to date on the formation and evolution of virialized, dark-matter dominated halos in a CDM universe has been via numerical N-body simulations of collisionless dark matter involving Gaussian random noise initial conditions. According to those N-body simulations, the

spherically-averaged mass distribution inside halos is universal, with a density profile which declines with radius, approaching $\rho \propto r^{-3}$ at large radii, flattening near the center to $\rho(r) \propto r^{-\alpha}$ with $\alpha < 2$. Two “universal” profiles bracket the results (NFW, Navarro, Frenk, & White 1997; Moore, Moore et al. 1998). The NFW (Moore) profile has an inner density profile $\rho \propto r^{-1}(r^{-1.5})$. The actual value of α is still uncertain, even though the N-body results have advanced to the point of including millions of simulation particles within the virial radius of a given halo (e.g. Fukushige & Makino 2001, 2003; Fukushige, Kawai, & Makino 2004; Griffiths et al. 1996; Jing & Suto 2000, 2002; Klypin et al. 2001; Power et al. 2003). Since the true inner profile may not be a power-law, comparisons of the inner slope for different simulation results are typically referred to a particular radius (e.g. $r = 0.01r_{\text{vir}}$, where r_{vir} is some measure of the outer radius of the virialized region). The N-body results generally support the conclusion that the same halo density profile applies to objects as different as dwarf galaxies and galaxy clusters, independent of halo mass, of the shape of the density fluctuation power spectrum, and of the background cosmology. This universality is apparent when comparisons of different halo profiles are made with density expressed in units of the density $\rho_{-2} \equiv \rho(r_{-2})$ at the radius r_{-2} at which each profile has a logarithmic slope of -2 , while radii for each halo are expressed in units of r_{-2} (Navarro et al. 2004). An exception to this universality is claimed by Ricotti (2003), who reports that the value of α depends upon halo mass, shallower for dwarf galaxies than for clusters, reflecting the different slopes of the power spectrum at the different

scales represented by these objects, but Colín et al. (2004) has challenged this claim.

Much attention has been focused on the N-body results for this inner slope, since the observed rotation curves of dark-matter dominated dwarf and low surface brightness (LSB) disk galaxies tend to favor mass profiles with a flat-density core unlike the singular profiles of the CDM N-body simulations (e.g. de Blok et al. 2001; de Blok & Bosma 2002; Flores & Primack 1994; Moore 1994; Simon et al. 2003; but, for a different view, see also Swaters et al. 2003a,b). On the cluster scale, too, there is some evidence from observations of strong gravitational lensing of background galaxies by foreground clusters which favors a flatter inner halo density profile than is found by the CDM N-body simulations (e.g. Gavazzi et al. 2003; Sand et al. 2004; Tyson, Kochanski, & dell’Antonio 1998; but see also Czoske et al. 2002). However, the halo mass fraction contained within the disputed inner cusp is actually quite small, so there may yet be dynamical processes not fully accounted for in the pure N-body simulations which can affect this small central mass without disturbing the overall universality of the rest of the profile.

Along with their universal mass profiles, CDM N-body halos also exhibit several universal properties in their phase-space distributions. Over most of the halo volume inside the virial radius, the DM particles are approximately isothermal – i.e. their velocity dispersion is fairly constant with radius – with only a relatively small dip in “temperature” toward the center (e.g. Frenk et al. 1999; Tormen, Bouchet, & White 1997). Halo particle velocities are also

approximately isotropic, with only a mild radial bias in the outer halo, which gives way to increasing isotropy toward the center (e.g. Carlberg et al. 1997; Colín, Klypin, & Kravtsov 2000; Eke, Navarro, & Frenk 1998; Fukushige & Makino 2001). The spherically-averaged mass motion at each radius is quite small and “subsonic;” the halo is not only in a state of global virial equilibrium but is close to hydrostatic equilibrium at each radius, too – i.e. it satisfies the spherical Jeans equation (e.g. Tormen et al. 1997).

Individual halos in CDM N-body simulations evolve over time, on average, through a continuous sequence of universal-shaped mass profiles of increasing total mass (Tasitsiomi et al. 2004; van den Bosch 2002; Wechsler et al. 2002). This Lagrangian mass evolution can be characterized by a universal mass accretion history: $M(a)/M(a_f)$, where a is the cosmic scale factor and a_f is some particular value of a , such as that at which $d \ln M / d \ln a = 2$ (Wechsler et al., 2002). As the mass of each halo grows with time due to the average effect of mergers and smooth infall, so does the concentration parameter c of its density profile, where $c \equiv r_{\text{vir}}/r_{-2}$, roughly as $c(a)/c(a_f) \propto a/a_f$ for $a/a_f > 1$ (Wechsler et al., 2002), after hovering at low values $c \leq 3 - 4$ during the initial phase of most rapid mass assembly prior to a_f (Tasitsiomi et al., 2004).

This description of the CDM halos of N-body simulations is a spherically-averaged one, which neglects many details. There is some scatter in the N-body results about this average description, of course. Individual halos are not truly spherically symmetric, either, but only approximately so. The ne-

glect of net angular momentum is probably not a bad first approximation, since the specific angular momentum is typically found to be far below that required for rotational support (e.g. Barnes & Efstathiou 1987; Bullock et al. 2001b)¹. However, the spherically-averaged description also averages out the small-scale density inhomogeneities inside each halo. This small-scale inhomogeneity may play an important role in the underlying dynamics which leads to halo formation and evolution in these N-body simulations. Regardless of its dynamical significance, this halo substructure has also been the subject of special attention for its own sake, once it was noticed that the number of subhalos which typically survive their merger into a larger halo in the N-body results is much larger than the number of galaxies observed within the Local Group (e.g. Klypin et al. 1999, Moore et al. 1999a).

While N-body simulations have made the universal equilibrium structure of halos described above a fundamental prediction of the CDM model, much less progress has been made on the analytical side, to derive and understand the numerical results and extend them beyond the range of numerical simulation. Our purpose in what follows is to summarize our own attack on this problem. In § 2.2, we describe the “fluid approximation”, the 1D, spherically-symmetric, dynamical model which we derived from the Boltzmann equation. In the following sections (§ 2.3, § 2.4), we use this method to study the formation and evolution of CDM halos in the cosmological context. Thus, we

¹The specific angular momentum profile, $j(M)$, of individual CDM halos averaged over spherical shells encompassing mass M , also has a universal shape, which has been fitted by $j(M) \propto M^s$ with $s = 1.3 \pm 0.3$ Bullock et al. (2001a).

show that this simple analytical model indeed provides valuable insights into the understanding of numerical results. We will re-visit this formalism in § 3.1 and Chapter 5.

2.2 Fluid Approximation

We show that fluid conservation equations for a gas with adiabatic index $\gamma = 5/3$ are a good approximation to the dynamics of both CDM and SIDM halos. This approach has been used in the literature of stellar dynamics (e.g. Larson 1970; Lynden-Bell & Eggleton 1980; Bettwieser 1983) for the study of the gravothermal catastrophe, where particles (stars) experience gravitational two-body interactions. The authors integrated the Boltzmann equation with a collision term due to gravitational two-body interactions, to obtain a set of moment equations. They then truncated, under reasonable assumptions, the hierarchy of such moment equations such that only fluid-like conservation equations remain. The effect of gravitational two-body interactions was naturally approximated as an effective heat conduction. In the CDM literature, Teyssier, Chieze, & Alimi (1997) and Subramanian, Cen, & Ostriker (2000) followed a similar approach for the study of CDM halos. Contrary to systems described by stellar dynamics where the number of particles is small, gravitational two-body interactions are completely negligible for CDM halos. The authors integrated collisionless Boltzmann equation to obtain a set of moment equations, and truncated its hierarchy as done for stellar dynamics. This results in fluid conservation equations for collisionless systems. This idea may

bother some readers since, strictly speaking, the collisionless nature of CDM prohibits the use of such an approximation. Collisionless particles have, in principle, an infinite set of moment equations when the Boltzmann equation is integrated (BBGKY hierarchy; e.g. Binney & Tremaine 1987). However, a couple of simple assumptions enable us to treat CDM halo dynamics with the usual fluid conservation equations. This section is devoted to the derivation of the fluid approximation, which we will apply in the following sections of this Chapter.

We develop this model under certain conditions. First, spherical symmetry is assumed. The initial condition is given by a spherically symmetric overdense region, and the subsequent evolution does not break the symmetry. Second, the infall of matter is assumed to be continuous. This can be achieved if we assume a smooth initial overdensity profile. Third, we restrict our attention to the matter-dominated era such that the cosmic mean density $\rho_b \propto t^{-2}$. This condition is true in the Λ CDM universe if the redshift is restricted to be $1 \lesssim z \lesssim z_{\text{eq}}$, where z_{eq} is the redshift for the matter-radiation equality.

2.2.1 Fluid approximation of collisionless CDM dynamics

Let us describe the fluid approximation for a self-gravitating, weakly collisional system in spherical symmetry. We define the average physical quantities as follows:

$$\rho = \int f d^3v, \tag{2.1}$$

$$\langle A \rangle \equiv \frac{\int A f d^3v}{\int f d^3v} = \frac{1}{\rho} \int A f d^3v, \quad (2.2)$$

$$u \equiv \langle v_r \rangle, \quad (2.3)$$

$$p_r \equiv \rho \langle (v_r - \langle v_r \rangle)^2 \rangle, \quad (2.4)$$

$$p_\theta \equiv \rho \langle (v_\theta - \langle v_\theta \rangle)^2 \rangle = \rho \langle v_\theta^2 \rangle, \quad (2.5)$$

$$p_\phi \equiv \rho \langle (v_\phi - \langle v_\phi \rangle)^2 \rangle = \rho \langle v_\phi^2 \rangle, \quad (2.6)$$

where f is the distribution function defined such that $f(\mathbf{r}, \mathbf{v})d^3rd^3v =$ mass within infinitesimal volume d^3rd^3v at (\mathbf{r}, \mathbf{v}) , ρ is the density, $\langle A \rangle$ is the average value of a certain quantity A , u is the radial bulk velocity, p_r is the “effective radial pressure”, and p_θ is the “effective tangential pressure”. Note that $\langle v_\theta \rangle = \langle v_\phi \rangle = 0$ and $p_\theta = p_\phi$ because of spherical symmetry. Anisotropy in the velocity dispersion occurs in general – i.e. $p_r \neq p_\theta$ or anisotropy parameter $\beta \neq 0$ where $\beta \equiv 1 - \frac{p_\theta}{p_r}$ – implying that we should treat p_r and p_θ separately. In a highly collisional system, which is well described by fluid conservation equations, $p_r = p_\theta$ and the usual pressure $p = p_r = p_\theta$.

A self-gravitating system of collisionless particles can be described by the collisionless Boltzmann equation

$$\frac{df}{dt} = 0, \quad (2.7)$$

where $\frac{d}{dt}$ is the phase-space Lagrangian time-derivative, given by

$$\frac{d}{dt} = \frac{\partial}{\partial t} + \mathbf{v} \cdot \frac{\partial}{\partial \mathbf{r}} + \mathbf{a} \cdot \frac{\partial}{\partial \mathbf{v}}. \quad (2.8)$$

Throughout this work, we will use the Newtonian approximation: when a system is much larger than its Schwarzschild radius and much smaller than the horizon size, motions of particles and the temperature of the system become non-relativistic. In this limit, we can use the non-relativistic Boltzmann transport equation. This equation can then be written more explicitly in spherical coordinates. For a system in spherical symmetry, $f = f(|\mathbf{r}|, \mathbf{v})$, and equation (2.7) reads

$$\begin{aligned}
0 = & \frac{\partial f}{\partial t} + v_r \frac{\partial f}{\partial r} + \left(\frac{v_\theta^2 + v_\phi^2}{r} - \frac{\partial \Phi}{\partial r} \right) \frac{\partial f}{\partial v_r} \\
& + \frac{1}{r} (v_\phi^2 \cot \theta - v_r v_\theta) \frac{\partial f}{\partial v_\theta} \\
& - \frac{v_\phi}{r} (v_r + v_\theta \cot \theta) \frac{\partial f}{\partial v_\phi},
\end{aligned} \tag{2.9}$$

where Φ satisfies the Poisson equation $\nabla^2 \Phi = 4\pi G \rho$ (Binney & Tremaine 1987). By multiplying equation (2.9) by $\int d^3v v_r^m v_\theta^n$, where m, n are integer numbers, we can form a set of moment equations. Moment equations from the lowest order are

$$\frac{\partial \rho}{\partial t} + \frac{\partial}{\partial r} (r^2 (\rho u)) = 0, \tag{2.10}$$

$$\frac{\partial}{\partial t} (\rho u) + \frac{\partial}{\partial r} (p_r + \rho u^2) + \frac{2}{r} (p_r - p_\theta + \rho u^2) = -\rho \frac{Gm}{r^2}, \tag{2.11}$$

$$\rho \frac{D}{Dt} \left(\frac{p_r}{2\rho} \right) + p_r \frac{\partial u}{\partial r} = \Gamma_1, \tag{2.12}$$

$$\rho \frac{D}{Dt} \left(\frac{p_\theta}{2\rho} \right) + \frac{p_\theta u}{r} = \Gamma_2, \tag{2.13}$$

⋮

where m is the mass enclosed by a shell at radius r , $\frac{D}{Dt} \equiv \frac{\partial}{\partial t} + u \frac{\partial}{\partial r}$, and

$$\begin{aligned} \Gamma_1 &= \frac{\rho}{r} \langle 2(v_r - \langle v_r \rangle) v_\theta^2 \rangle \\ &\quad - \frac{1}{2r^2} \frac{\partial}{\partial r} (r^2 \rho \langle (v_r - \langle v_r \rangle)^3 \rangle), \end{aligned} \quad (2.14)$$

$$\Gamma_2 = -\frac{1}{4r^4} \frac{\partial}{\partial r} (r^4 \rho \langle (v_r - \langle v_r \rangle) v_\theta^2 \rangle). \quad (2.15)$$

Equations (2.10) - (2.13) are conservation equations of mass, momentum, “radial” energy, and angular momentum respectively. Note that equations (2.10) - (2.15) are all in exact form, and the hierarchy of equations is not closed in principle.

Now we make a further simplification that the distribution of v_r is skewless – v_θ and v_ϕ are naturally skewless because of spherical symmetry. In other words, we assume that v_r has a symmetric distribution around $\langle v_r \rangle$. It is not straightforward to show that Γ_1 and Γ_2 are negligible in equations (2.12) and (2.13). However, we demonstrate that the assumption of “skewlessness” in the fluid approximation yields results which are in good agreement with the purely collisionless CDM structure, for specific examples². As shown in the Bertschinger (1985) solution, for instance, collisionless particles (shells) form a quasi-symmetric winding structure in the phase space as shown in Figure 2.1. This indicates that we may neglect terms which arise as a result of skewness. Equations (2.10) - (2.12) with the condition $p_\theta = 0$ and $\Gamma_1 = \Gamma_2 = 0$,

²Subramanian et al. (2000) argue that an initially skewless distribution function f will remain skewless even after evolution. It is true if one is interested in the fine-grained distribution, or each stream line. However, if one considers coarse-grained quantities as defined by equation (2.2), the contribution from multiple stream lines should be counted and the overall distribution is not skewless, in general.

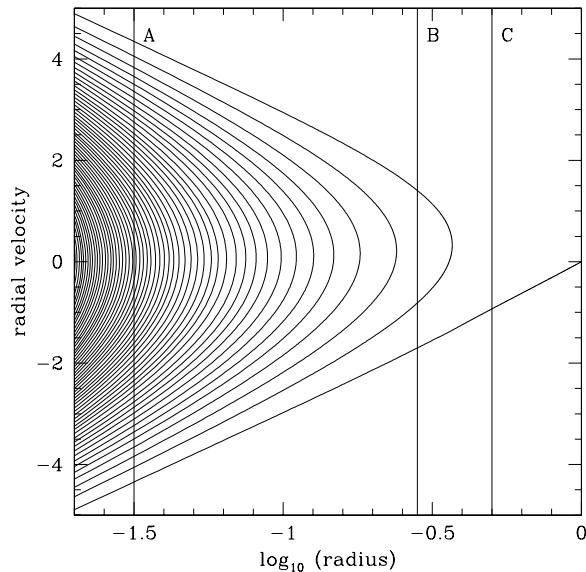


Figure 2.1: Self-similar collisionless halo formation for $\varepsilon = 1$: Phase-space diagram of Bertschinger (1985) solution as an illustration of the “skewless distribution” assumption. Along the line A there are a large number of shell-crossings, which are almost symmetric around $\langle v_r \rangle$, and along the line C, as there is only one stream line, it is intrinsically skewless. On the contrary, there are only three stream lines along the line B, so the assumption is not good in the region inside and close to the outermost caustics. Tangential velocity distribution would have a similar behavior when tangential motion is allowed.

$$\frac{\partial \rho}{\partial t} + \frac{\partial}{\partial r}(r^2(\rho u)) = 0, \quad (2.16)$$

$$\frac{\partial}{\partial t}(\rho u) + \frac{\partial}{\partial r}(p_r + \rho u^2) + \frac{2}{r}(p_r + \rho u^2) = -\rho \frac{Gm}{r^2}, \quad (2.17)$$

$$\rho \frac{D}{Dt} \left(\frac{p_r}{2\rho} \right) + p_r \frac{\partial u}{\partial r} = 0, \quad (2.18)$$

can be used to solve purely radial problems, such as the spherical infall problems with similarity solutions by Bertschinger (1985, $\varepsilon = 1$) and Fillmore &

Goldreich (1984, with $\varepsilon = 1/6$). As seen in Figure 2.2, the solution to equations (2.16) - (2.18) is in good agreement with the true solution. We have also found, as seen in Figure 2.3, an excellent agreement between the collisionless solution and the one produced by a radial fluid approximation in the case of $\varepsilon = 1/6$ (the $\varepsilon = 1/6$ case is of main interest in this work). The difference observed at caustics – places where the density becomes infinite – is negligible, because caustics do not affect the overall dynamics of the halo. Since the skew-free assumption naturally neglects dynamically unimportant structure (e.g. caustics) while accurately reproducing the profile of the exact solution in these radial cases, it may also be applied to describe CDM halos, in which particles have a tangential motion as well.

The final assumption is that inside the virialized structure (i.e. post-shock region) the velocity dispersion is isotropic, or $p_r = p_\theta$. This is an empirical assumption: CDM halos in cosmological N-body simulations show mild anisotropy. For instance, Carlberg et al. (1997) show that CDM halos in their numerical simulation can be well-fitted by a fitting formula

$$\beta(r) = \beta_m \frac{4r}{r^2 + 4}, \quad (2.19)$$

where r is in units of r_{200} , and $\beta_m = [0.3 - 0.5]$ (see also, e.g., Thomas et al. 1998 and Colín et al. 2000). As we will show in the following sections, our similarity solutions have a virial radius $r_{564} \simeq 0.6 r_{200}$, which then results in the maximum anisotropy $\beta \sim [0.17 - 0.28]$. This fact enables us to use $\beta = 0$ to a good approximation.

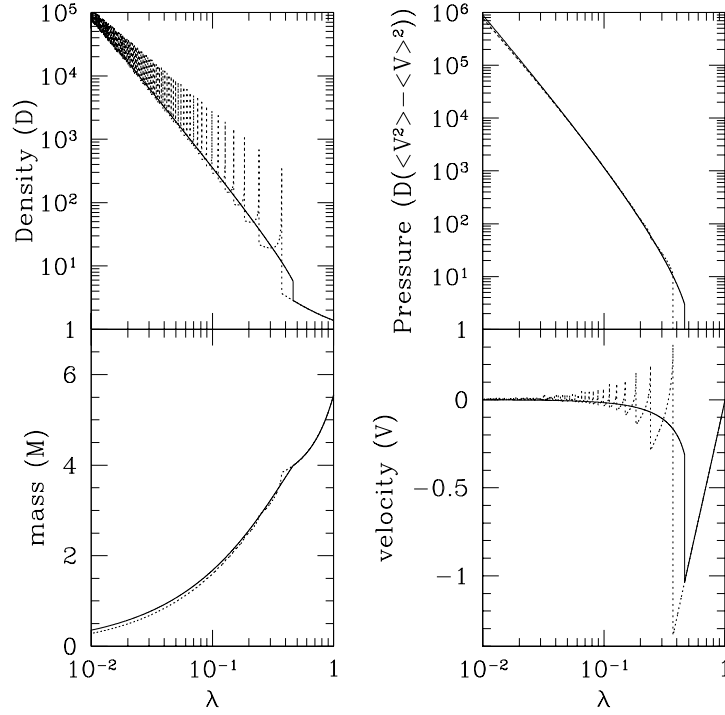


Figure 2.2: Self-similar collisionless halo formation for $\varepsilon = 1$: Comparison of the skewless-fluid approximation to the exact collisionless Bertschinger solution. Solid lines represent the solution obtained from the fluid approximation in the radial direction, while dotted lines represent the collisionless Bertschinger solution. Spikes in the density plot simply represent infinite values, corresponding to caustics, and therefore there is no physical significance in the height of these spikes. However, spikes in the velocity plot are finite and real. Note that solid lines do not represent the $\gamma = 5/3$ fluid Bertschinger solution.

With these assumptions (spherical symmetry, skew-free velocity distribution, and isotropic velocity dispersion), the usual fluid conservation equations are obtained. They are

$$\frac{\partial \rho}{\partial t} + \frac{\partial}{\partial r}(r^2(\rho u)) = 0, \quad (2.20)$$

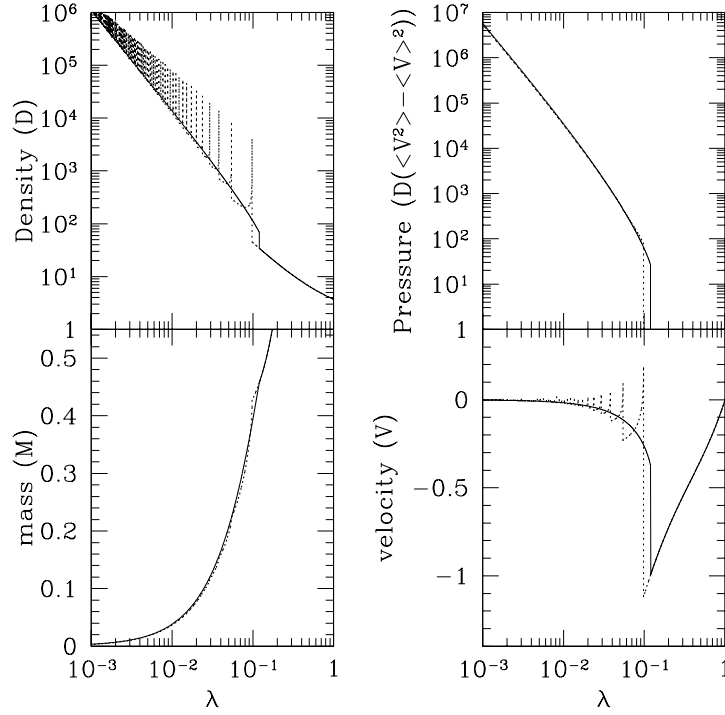


Figure 2.3: Same as Figure 2.2, but $\varepsilon = 1/6$. Note again that the solid line was not generated from the $\gamma = 5/3$ fluid approximation, but rather from the radial-only fluid approximation described by equations (2.16 - 2.18).

$$\frac{\partial}{\partial t}(\rho u) + \frac{\partial}{\partial r}(p + \rho u^2) + \frac{2}{r}\rho u^2 = -\rho \frac{Gm}{r^2}, \quad (2.21)$$

$$\frac{D}{Dt}\left(\frac{3p}{2\rho}\right) = -\frac{p}{\rho} \frac{\partial}{r^2 \partial r}(r^2 u), \quad (2.22)$$

which are identical to the fluid conservation equations for a $\gamma = 5/3$ gas in spherical symmetry. Resemblance of these equations to fluid equations indicate that we can expect an effective “shock” even for a collisionless system because of the hyperbolicity of these equations. This is also illustrated in Figure 2.1. For instance, the density jump occurs when one moves from the

“pre-shock” region (line C; one stream line) to the “post-shock” region (line B; three stream lines). However, one should be careful in using this formalism because the approximation becomes worse where there are only a small number of phase-space windings.

2.3 Halo Formation by Self-Similar Infall

2.3.1 Halo formation from scale-free linear perturbations

In the Einstein-de Sitter (EdS) background universe, an initial linear perturbation whose mass profile is spherically symmetric and has a scale-free, power-law form

$$\frac{\delta M}{M} \propto M^{-\varepsilon} \quad (2.23)$$

results in structure formation which is self-similar (FG). Each spherical mass shell around the center expands until it reaches a maximum radius (turnaround radius r_{ta}), and re-collapses. For a given ε , we have

$$r_{\text{ta}} \propto t^{\xi}, \quad (2.24)$$

where

$$\xi = \frac{2}{3} \left(\frac{3\varepsilon + 1}{3\varepsilon} \right). \quad (2.25)$$

Since there are no characteristic length or time scales for this problem other than the turn-around radius r_{ta} and the Hubble time t , the gravitational collapse which ensues from this scale-free initial condition must be self-similar as long as the background universe is Einstein-de Sitter, in the absence of physical processes which introduce additional scales (e.g. SIDM collisionality)

In general, if the unperturbed matter is a cold fluid, the infall which results from this perturbation is highly supersonic and is terminated by a strong accretion shock which thermalizes the kinetic energy of collapse. The accretion shock radius is guaranteed by self-similarity to be a fixed fraction of $r_{\text{ta}}(t)$ at all times. The mean density of the postshock region is, therefore, always a fixed multiple of the cosmic mean matter density. For most cases of interest, this postshock region is close to hydrostatic. For a collisionless gas, a similar description applies as long as the infalling matter initially had small (or zero) random motions. In that case, each mass shell collapses supersonically as a single stream until it encounters a region of shell-crossing and density caustics, which encompasses all previously collapsed (i.e. interior) mass shells. All collapsed mass shells inside this region oscillate about the center. The radius of this region of shell-crossing, given by the outermost density caustic, is analogous to the shock radius in the fluid case.

Results for the purely collisionless case were presented for arbitrary values of ε by FG, and for $\varepsilon = 1$ by Bertschinger (1985) (where the latter included a fluid component, as well). Figures 2.2 and 2.3 show the exact similarity solutions for the purely collisionless cases with $\varepsilon = 1$ and $\varepsilon = 1/6$, respectively. As we describe below in §2.3.2, these values roughly bracket the range relevant to cosmological halos in a CDM universe.

2.3.2 Halo formation from peaks of the Gaussian random noise primordial density fluctuations

The theory of halo formation from peaks in the density field which result from Gaussian-random-noise initial density fluctuations draws an interesting connection between the average density profile around these peaks and the shape of the fluctuation power spectrum. According to HS, local maxima of Gaussian random fluctuations in the density can serve as the progenitors of cosmological structures. They show that rare density peaks ($\nu \geq 3$, where ν corresponds to $\nu\sigma_M$ peak) have a simple power-law profile³

$$\Delta_0(r) \propto r^{-(n+3)}, \quad (2.26)$$

where $\Delta_0(r)$ is the accumulated overdensity inside radius r , and n is the effective index of the power spectrum $P(k)$ approximated as a power-law $P(k) \propto k^n$ at wavenumber k which corresponds to the halo mass as described in Appendix A⁴. The overdensity $\Delta_0(r)$ is equivalent to the fractional mass perturbation $\delta M/M$ inside radius r ,

$$\Delta_0(r) = \delta M/M \propto M^{-\frac{n+3}{3}}. \quad (2.27)$$

³Bardeen et al. (1986) also get a similar result: local density maxima have a triaxial profile, but as ν increases it becomes more and more spherical with a profile converging to equation (2.26).

⁴The average linear overdensity profile, equation (2.26), holds for any value of ν . For small ν , however, random dispersion around this average profile becomes substantial, limiting the generality of equation (2.26).

From equations (2.23) and (2.27), we deduce that the power-law power spectrum naturally generates a scale-free initial condition with

$$\varepsilon = (n + 3)/3. \quad (2.28)$$

According to this model, as described in Appendix A, halos of a given mass M originate from density perturbations given by equation (2.27) with n determined by the primordial power spectrum after it is transferred according to the parameters of the background universe and the nature of the dark matter. We plot this effective n as a function of halo mass in Figure 2.4 for the current Λ CDM universe. The value of $n \simeq -2.5$ is a reasonable approximation for galactic halos (i.e. $n \simeq -2.5 \pm 0.1$ for $M \simeq 10^{8 \pm 2} M_\odot$, while $n \simeq -2.5 \pm 0.2$ for M in the range from $10^3 M_\odot$ to $10^{11} M_\odot$). For halos in the cluster mass range, $M \sim 10^{15} M_\odot$, $n \simeq -1.5$.

2.3.3 Self-similar halos: an analytical model for CDM N-body results

We describe properties of the similarity solution for $\varepsilon = 1/6$ scale-free gravitational collapse of CDM halos. The set of equations for this case, and the method to obtain the solution will be described in § 3.1.3.2, in conjunction with the similarity solution for SIDM halos. CDM similarity solution can be interpreted as a special case with zero heat conduction (§ 3.1.3.2).

As we shall show in what follows, the adiabatic infall solution for $\varepsilon = 1/6$ case resembles standard CDM halos in many respects. First, it has a density cusp with a logarithmic slope $\simeq -1.27$ for $4 \times 10^{-3} < r/r_{200} < 1.4 \times$

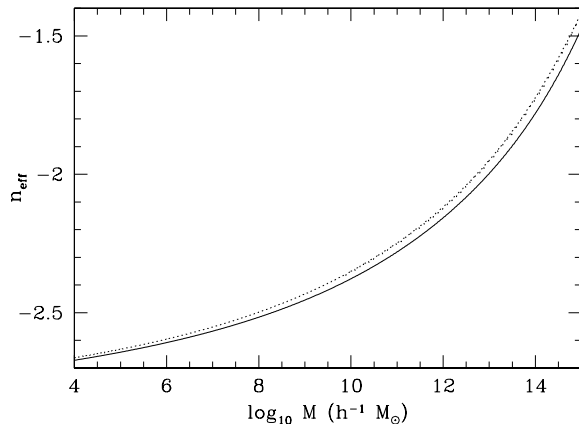


Figure 2.4: Effective index of the power spectrum ($P(k) \propto k^{n_{\text{eff}}}$) vs. halo mass for the Λ CDM universe. Appendix describes how n_{eff} is calculated. The solid line is derived from the HS approach, which we use in this work. The dotted line is derived from σ_M .

10^{-2} , where r_{200} is the radius in which the average density is $200\rho_b$, if the density is extrapolated beyond r_s with the NFW profile that best-fits this adiabatic solution (Fig. 2.5). Note that it is possible to have a slope shallower than -2 because particle velocities are allowed to have a tangential component. If no tangential motion is allowed, the value -2 is the shallowest slope possible for collisionless dark matter halos (Richstone & Tremaine 1984; Teyssier et al. 1997; Bertschinger 1998).

Second, the temperature profile is very similar to that of CDM halos. The temperature is zero at the center, rises to a maximum at some λ , and then falls to a nonzero value at the shock. An important point is that the temperature inversion exists. In case SIDM is considered (§3.1), the addition

of conductivity helps to form soft cores. Without the temperature inversion, addition of conductivity will worsen the situation by initiating gravothermal catastrophe, rather than generating a soft core.

The average density inside the shock radius is found to be $564\rho_b$ for the adiabatic solution. This value is larger than the average density ($\simeq 200$) usually adopted by convention to identify virialized CDM halos in N-body simulations. In terms of radius, $r_s = r_{564} \simeq 0.6r_{200}$. Our similarity solution, therefore, yields a shock at a smaller value of radius than is typically used to characterize the virial radius of CDM halos in N-body simulations. However, as long as we focus on the properties inside r_{564} , the adiabatic solution is a good fit to CDM halos as we shall see below. As seen in Figure 2.5, except for the innermost central region where the ambiguity of density slope exists between -1 (Navarro et al., 1997) and -1.5 (Moore et al., 1998), our adiabatic solution agrees with the NFW profile and the Moore profile to within 10%, depending on the concentration parameter. Compared to halo profiles studied by Diemand, Moore, & Stadel (2004), the agreement is even better (Fig. [2.5]). We also find that a local logarithmic slope slowly changes to shallower values as one approaches the center, which agrees with the trend reported by Navarro et al. (2004). We demonstrate this as follows.

We compare the adiabatic solution with the CDM N-body halo profiles mentioned above: i.e. the NFW profile,

$$\rho_{\text{NFW}} = \frac{\rho_{\text{sc}}}{(r/r_{\text{sc}})(1+r/r_{\text{sc}})^2}, \quad (2.29)$$

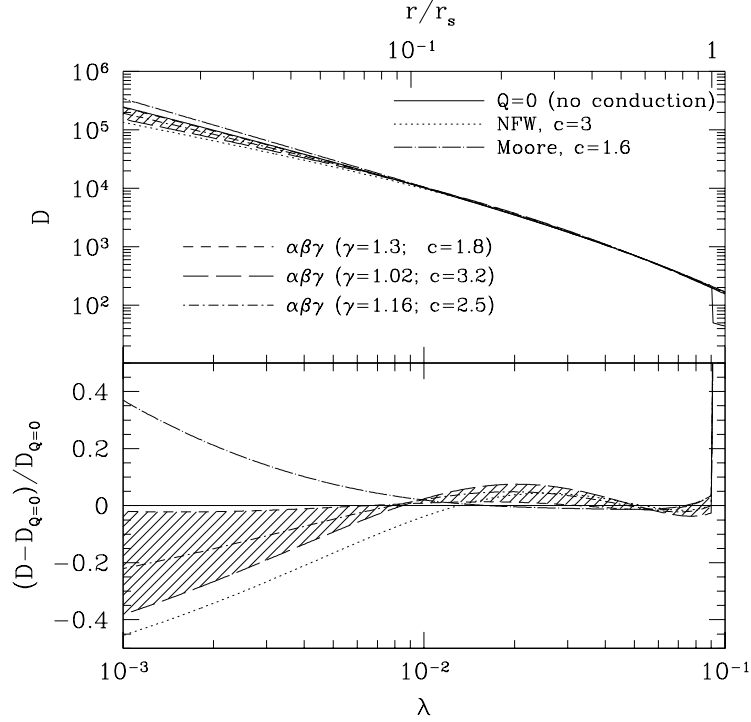


Figure 2.5: Comparison of self-similar halo profile without conduction with N-body results for CDM halos: (top panel) Density (in units of cosmic mean density) vs. radius (in units of current turnaround radius) for similarity solution ($Q = 0$; $\varepsilon = 1/6$) (solid), the best-fitting NFW profile ($c = 3$), Moore profile ($c = 1.6$) and several $\alpha\beta\gamma$ profiles ($\alpha = 1$, $\beta = 3$) for different values of γ , $\gamma = 1.3$ (best fit), 1.02, 1.16, as labeled. Diemand et al. (2004) find N-body results for CDM halos best fit by $(\alpha, \beta, \gamma) = (1, 3, \gamma = 1.16 \pm 0.14)$ (shaded region); (bottom panel) fractional deviation of the N-body results from similarity solution. Note that $\lambda = \lambda_s \simeq 0.09$ corresponds to $r_s = r_{564} \simeq 0.6 r_{200}$.

the Moore profile,

$$\rho_M = \frac{\rho_{sc}}{(r/r_{sc})^{1.5} (1 + (r/r_{sc})^{1.5})}, \quad (2.30)$$

and the $\alpha\beta\gamma$ profile (e.g. Diemand et al. 2004),

$$\rho_{\alpha\beta\gamma} = \frac{\rho_{\text{sc}}}{(r/r_{\text{sc}})^\gamma (1 + (r/r_{\text{sc}})^\alpha)^{(\beta-\gamma)/\alpha}}, \quad (2.31)$$

by finding the best-fitting parameters. The NFW and Moore profiles have two free parameters (ρ_{sc} and r_{sc}), while the $\alpha\beta\gamma$ profile has three (ρ_{sc} , r_{sc} , and γ) when α and β are fixed as in Diemand et al. (2004). We depict this comparison in Figure 2.5, with the “concentration parameter” – defined by $c \equiv r_{200}/r_{\text{sc}}$ – used to find the best-fitting N-body halo profiles. For $\alpha\beta\gamma$ profiles, we use the best-fitting profiles by Diemand et al. (2004), namely $\alpha = 1$, $\beta = 3$, $\gamma = 1.16 \pm 0.14$. Among these profiles, the $\alpha\beta\gamma$ profile with $\alpha = 1$, $\beta = 3$ and $\gamma = 1.3$ provides the best agreement with the adiabatic solution.

The relatively low concentration parameter, $c \simeq 3$, required for the best-fitting NFW profile deserves attention with respect to cosmological mass accretion rate. This value is a bit small compared to the typical concentration parameters, $c \sim [4-20]$, observed at $z = 0$ in N-body simulations. Recent high resolution N-body simulation results, however, report such low concentration parameters if CDM halos are observed at higher redshifts (e.g. Tasitsiomi et al. 2004). Individual halos in CDM N-body simulations evolve over time, on average, through a continuous sequence of universal-shaped mass profiles of increasing total mass (Tasitsiomi et al. 2004; Alvarez, Ahn, & Shapiro 2003). This Lagrangian mass evolution can be characterized by a universal mass accretion history:

$$M(a) = M_\infty \exp(-2a_f/a), \quad (2.32)$$

where a is the cosmic scale factor and a_f is some particular value of a , such as that at which $d \log M / d \log a = 2$ (Alvarez et al. 2003). As the mass of each halo grows with time due to the average effect of mergers and smooth infall, so does the concentration parameter c of its density profile, roughly as $c(a)/c(a_f) \propto a/a_f$ for $a/a_f > 1$ (Alvarez et al. 2003), after hovering at low values $c \approx 2 - 4$ during the initial phase of most rapid mass assembly prior to a_f (Tasitsiomi et al. 2004). Our similarity solution has $\frac{d \log M}{d \log a} = 6$, and this corresponds to $a = a_f/3$. As our solution corresponds to a very early epoch in the halo formation history, or a fast accretion rate, such a low concentration parameter is a natural outcome.

In summary, we have shown that the adiabatic solution for $\varepsilon = 1/6$ approximates the N-body CDM halo profiles well, thus providing physical insights about their origin. Quantitatively, our analysis here is still limited by the assumption of self-similarity: the non-self-similar *evolution* of the CDM halo structure observed in N-body simulations cannot be explained by a constant logarithmic mass accretion rate $\frac{d \log M}{d \log a} = 6$. In the next section, we will adopt a time-varying logarithmic mass accretion rate observed in N-body simulations in order to see whether the evolution of CDM halo structure is also determined by its mass accretion history.

2.4 Halo Formation by Non-Self-Similar Infall: Mass Assembly History and the Origin of CDM N-body Halo Profiles

N-body simulations of CDM have not only found a universal halo density profile, but have also found that the masses and concentrations of individual N-body CDM halos grow over time according to simple universal formulae by Wechsler et al. (2002). In what follows we use the fluid approximation to show that this universal time-dependent halo density profile can be understood as the dynamical outcome of continuous infall according to the universal mass accretion history (Alvarez et al., 2003).

2.4.1 Models and initial conditions

We attempt to understand the form and evolution of dark matter halos with three spherically-symmetric models; halted infall, radial orbits, and a fluid approximation. Each model assumes that the mass M_{vir} within an overdensity Δ_{vir} follows the relation given by Wechsler et al. (2002)

$$M_{\text{vir}}(a) = M_{\infty} \exp[-Sa_{\text{f}}/a], \quad (2.33)$$

where S is the logarithmic mass accretion rate $d\ln M_{\text{vir}}/d\ln a$ when $a = a_{\text{f}}$. Here and in Wechsler et al. (2002), $S = 2$. Such a relation is claimed to be a good fit to the evolution of halos of different masses and formation epochs. We use $\Delta_{\text{vir}} = 200$, so that the halo has a mass M_{200} and radius r_{200} . We have found an initial perturbation profile consistent with equation (2.33) (for EdS),

$$\frac{\delta M}{M} \equiv \frac{M - \bar{M}}{\bar{M}} = \delta_{\text{i}} \ln \left[\frac{M}{bM_{\infty}} \right], \quad (2.34)$$

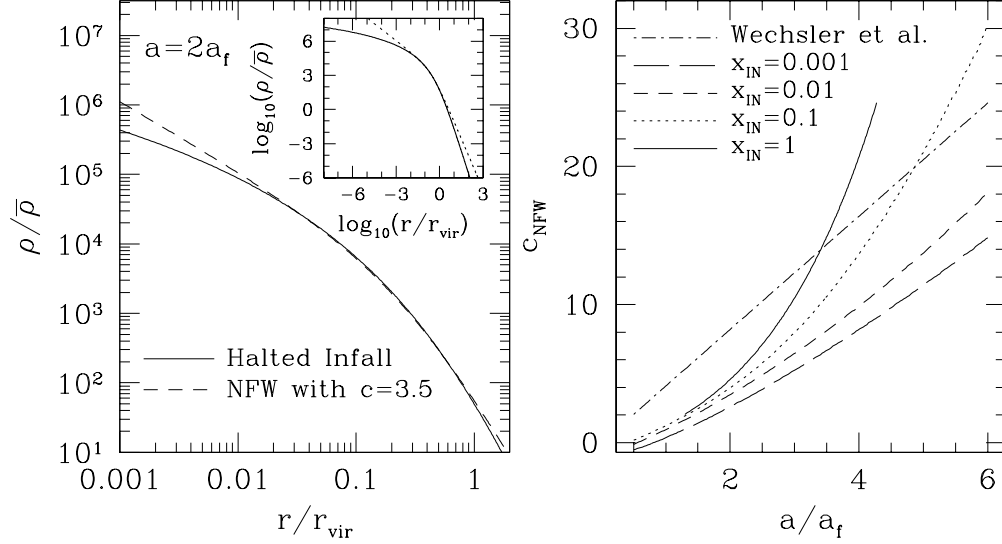


Figure 2.6: (left) Density profile from halted infall model along with best-fitting NFW profile for this profile at present. Inset in upper-right shows same over much larger range. (right) Evolution of NFW concentration parameter in the halted infall model, compared with empirical relation of Wechsler et al. (2002) for CDM N-body halos. Different line types indicate different ranges $x_{\text{in}} < x < 1$, within which halo was fit to an NFW profile, where $x \equiv r/r_{\text{vir}}$, $r_{\text{vir}} \equiv r_{200}$.

where δ_i depends on the initial scale factor a_i , a_f , and δ_{vir} , and \bar{M} is the unperturbed mass. The parameter $b = 1$ if pressure or shell crossing are not present outside of r_{vir} . If they are present outside the halo however, the initial perturbation is not guaranteed to lead to the correct mass accretion rate. In our radial orbit and fluid approximation calculations below, where shell crossing and pressure are indeed present outside of r_{vir} , we have found that the resulting mass is close to that of equation (2.33) if b is allowed to vary as a fitting parameter ($b = 1(0.7)$ in the fluid approximation (radial orbits)

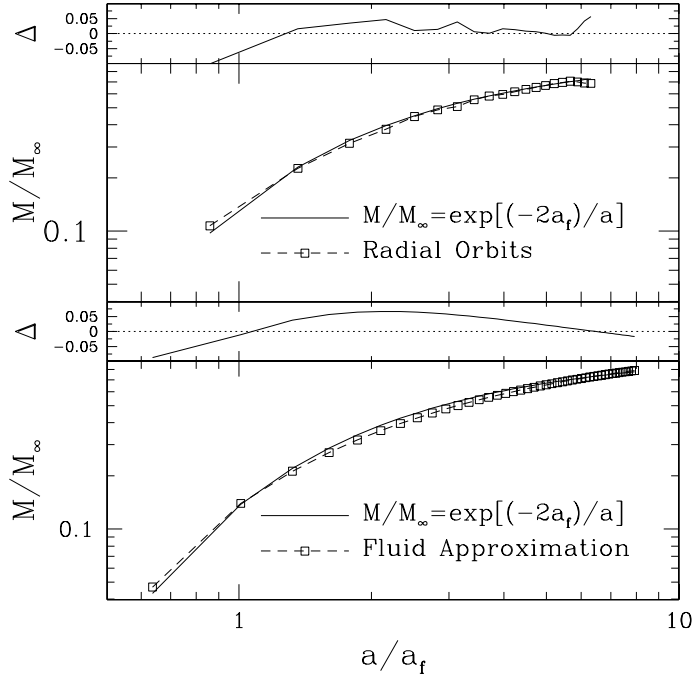


Figure 2.7: Evolution of mass for the radial orbits (top) and fluid approximation (bottom) simulations, compared with the empirical relation of Wechsler et al. (2002) for CDM N-body results. Shown above each are the fractional deviations $\Delta \equiv (M_{\text{exact}} - M)/M$.

calculations).

2.4.2 Halted infall model

In the simplest model, we have assumed that infalling shells come to an abrupt halt upon crossing into the halo, so that the velocity is zero for $r < r_{\text{vir}}$. The mass of the halo is

$$M_{\text{vir}}(a) = \frac{4\pi}{3} \delta_{\text{vir}} \bar{\rho} r_{\text{vir}}^3, \quad (2.35)$$

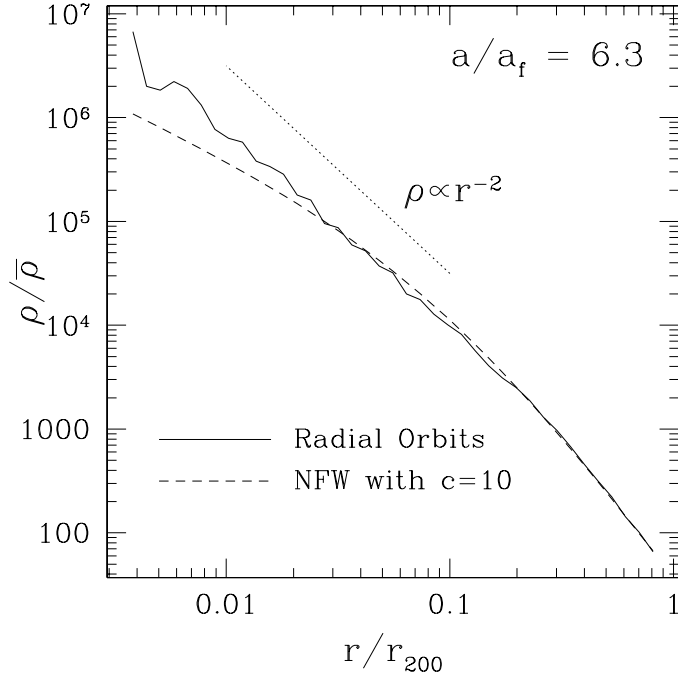


Figure 2.8: Density profile at the end of the radial orbit simulation.

where $\bar{\rho}$ is the cosmic mean mass density at that epoch. Mass continuity implies the density ρ_{vir} just inside the virial radius is related to the rate of halo mass and radius increase according to

$$\frac{dM_{\text{vir}}}{da} = 4\pi\rho_{\text{vir}}r_{\text{vir}}^2 \frac{dr_{\text{vir}}}{da}. \quad (2.36)$$

Differentiating equation (2.35) and combining with equations (2.33) and (2.36), one obtains

$$\frac{\rho_{\text{vir}}}{\bar{\rho}_0} = \delta_{\text{vir}}a^{-3} \left[1 + \frac{3a}{Sa_f} \right]^{-1}, \quad (2.37)$$

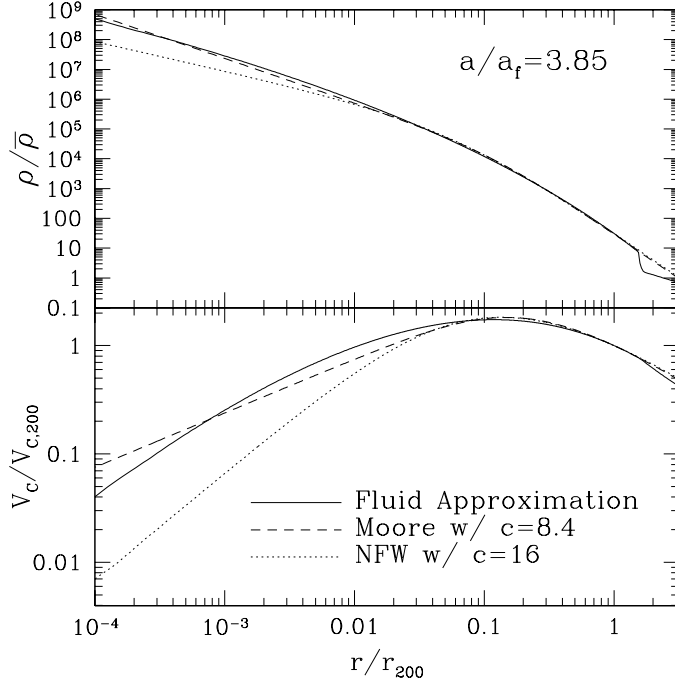


Figure 2.9: (top) Density profile at the end of the isotropic fluid calculation. (bottom) Circular velocity profile.

where $\bar{\rho}_0$ is the mean background density at $a = 1$. The virial radius is given by

$$\frac{r_{\text{vir}}}{r_{\text{vir},0}} = a \exp \left[\frac{-S a_f}{3} \left(\frac{1}{a} - 1 \right) \right]. \quad (2.38)$$

Equations (2.37) and (2.38) are parametric in a , implying a radial density profile $\rho(r) = \rho_{\text{vir}}(r_{\text{vir}})$ that is frozen in place as matter crosses r_{vir} . Taking the limit in which $a \rightarrow \infty$, the outer density profile approaches $\rho \propto r^{-4}$ at late times, consistent with finite mass, while the inner slope becomes asymptotically flat. The NFW profile is

$$\frac{\rho(x)}{\bar{\rho}} = \frac{\delta_{\text{vir}} g(c)}{3x(1+cx)^2}, \quad (2.39)$$

where

$$g(c) = \frac{c^2}{\ln(1+c) - c/(1+c)}, \quad (2.40)$$

and $x \equiv r/r_{\text{vir}}$. Combining equations (2.37) and (2.39) with $x = 1$, yields an equation for the evolution of concentration with scale factor (see Fig. 2.6),

$$\frac{a}{a_{\text{f}}} = S \left[\frac{(1+c)^2}{g(c)} - \frac{1}{3} \right]. \quad (2.41)$$

2.4.3 Radial orbits model

We use a finite-difference spherical mass shell code to follow the evolution of a small amplitude initial perturbation given by equation (2.34), which is chosen so that the resulting virial mass will evolve according to equation (2.33). The shell code has an inner reflecting core and the results presented here used 20,000 shells. The resulting evolution of halo mass and the comparison of the halo density profile with the NFW profile are shown in Figures 2.8 and 2.9.

2.4.4 Fluid approximation model

As mentioned earlier in §2.2, the collisionless Boltzmann equation in spherical symmetry yields fluid conservation equations ($\gamma = 5/3$) when random motions are isotropic. Halos in N-body simulations have somewhat radially-biased random motion, but the bias is small, especially in the center. Outside the virialized halo, in the infall region, the radial bias is irrelevant, since the motion is highly supersonic and random motions do not affect the dynamics there. This isotropic fluid model is therefore a better approximation to halo

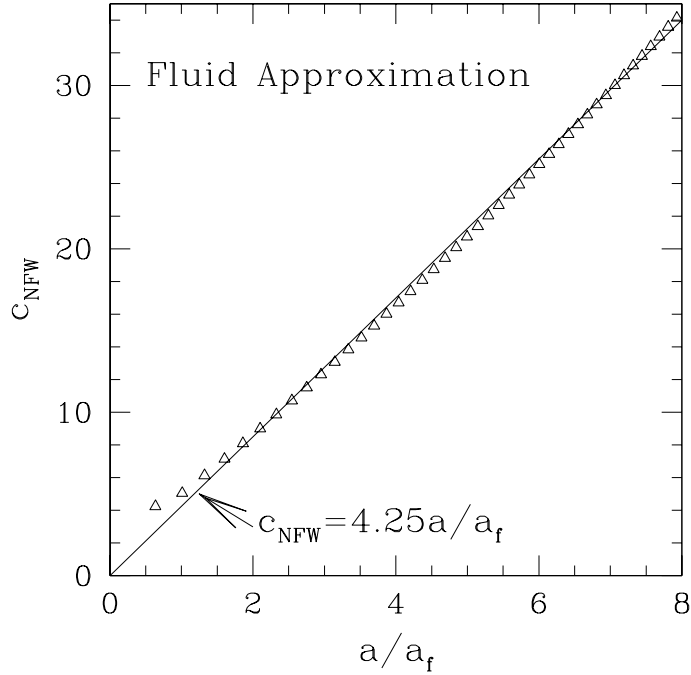


Figure 2.10: Evolution of concentration parameter with scale factor in the isotropic fluid calculation.

formation in N-body simulations than one with purely radial motion. We use a 1-D, spherical, Lagrangian hydrodynamics code as in Thoul & Weinberg (1995), using 1,000 zones logarithmically spaced in mass. The initial conditions were chosen in the same way as those for the radial orbit model (Eq. (2.34)), with zero initial temperature. Results are plotted in Figures 2.7-2.10.

2.4.5 Results

Our results can be summarized as follows:

- The halted infall model of §2.4.2 does not reproduce the linear evolution

of concentration parameter with scale factor reported by Wechsler et al. (2002), but can be fit by an NFW profile over a limited range of radii and scale factors (Fig. 2.6).

- We have derived an initially linear perturbation profile that is a good model for the spherically-averaged initial condition that leads to the Lagrangian mass evolution of CDM halos found in N-body simulations by Wechsler et al. (2002).
- Starting from this perturbation, the radial orbit model of section 2.4.3 fails to reproduce the inner slope of the NFW profile, approaching $\rho \propto r^{-2}$ instead, consistent with the argument of Richstone & Tremaine (1984) (Fig. 2.8).
- The fluid approximation of §2.4.4, however, leads to a halo that is well-fitted by the NFW and Moore profiles for all radii resolved by N-body simulations ($r/r_{200} \geq 0.01$) (Fig. 2.9).
- In addition, the evolution of the NFW concentration parameter in the fluid approximation is a close match to that of Wechsler et al. (2002), with $c_{\text{NFW}} = 4.25a/a_f$ a good fit (Fig. 2.10); $c_{\text{NFW}} = 4.1a/a_f$ was the relation reported by Wechsler et al. (2002).

The fluid approximation model reproduces the N-body results remarkably well, once the mass accretion history is given. We are thus led to conclude that complicated merging processes are not necessary in order to understand

the overall structure and evolution of the halo mass distribution, and that it is largely determined by the mass accretion history.

Chapter 3

Nature of Dark Matter

3.1 Self-Interacting Dark Matter

3.1.1 Introduction

The cold dark matter (CDM) model provides a successful framework for understanding the formation and evolution of structure in our universe. According to this model, gravity amplifies primordial density fluctuations, and structure forms by hierarchical clustering: small objects form first, later merging to form larger objects. The most promising candidate for CDM is the weakly interacting massive particle (WIMP). In this picture, the microscopic interaction between CDM particles is negligible (collisionless), and they interact only by gravity. However, this assumption has not been fully verified and it is fair to say that the microscopic nature of CDM is still unknown. It is important, therefore, to explore the consequences of varying this underlying assumption about CDM in the hope that astronomical observations can be used to place meaningful constraints.

The possible variation of the microscopic nature of cold dark matter is closely linked to the problems of the CDM model. Despite its success, the CDM model has several problems which exist mostly in the small scale regime (see, for example, Moore 2001). Among these problems, much attention has

been focused on the N-body simulation results for the inner density slope, since the observed rotation curves of dark-matter dominated dwarf and low surface brightness (LSB) disk galaxies tend to favor mass profiles with a flat-density core unlike the singular profiles of the CDM N-body simulations (e.g. Flores & Primack 1994; Marchesini et al. 2002). The latter are generally characterized by an empirical fitting formula for the spherically averaged density profiles in those N-body results, either the Navarro-Frenk-White (NFW) profile (Navarro et al. 1997), for which $\rho \propto r^{-1}$ as $r \rightarrow 0$, or the Moore profile (Moore et al. 1999b), for which $\rho \propto r^{-1.5}$ instead¹. It was controversial whether the observed data was resolved well enough to indicate a soft core (e.g. see van den Bosch & Swaters 2001 for possible beam smearing effect on the data), but observations have built up which favor the soft core even after eliminating the beam smearing effect (e.g. Marchesini et al. 2002 and references therein). After much more work on the N-body simulations of CDM, the discrepancy between these data and the numerical halo profiles remains significant (see, for instance, Navarro et al. 2004)

This apparent discrepancy between the N-body simulation results and observations of dwarf galaxy rotation curves has raised a question about the nature of dark matter, including the assumption that CDM is collisionless.

¹Recently, Hayashi et al. (2004) and Navarro et al. (2004) reported that the logarithmic slope of the spherically averaged density profile of dark matter halos in their Λ CDM simulations, $-\mathrm{d} \ln \rho / \mathrm{d} \ln r$, decreases monotonically towards the center. This change of slope, however, does not seem to fully account for the observed rotation curves. Navarro et al. (2004) conclude, by surveying several simulation results by different groups, that neither the typical NFW profile nor the Moore profile provides a good fit, but one needs a little more complex form such as the one by Navarro et al. (2004).

People have suggested solutions to this discrepancy which either preserves the collisionless nature of the dark matter or else adopts a new picture. In the former category are explanations which attribute the discrepancy to astrophysical processes beyond the pure N-body dynamics (e.g. El-Zant, Shlosman, & Hoffman 2001; Weinberg & Katz 2002) or to a primordial power spectrum tilted away from the Harrison-Zel'dovich shape (e.g. Zentner & Bullock 2002). In the latter category, the proposal of self-interacting dark matter (SIDM) by Spergel & Steinhardt (2000) has received a lot of attention. In this picture, microscopic interaction between dark matter particles is non-negligible and can affect the dynamics of halo formation. Since the actual identity and microscopic nature of CDM is still unknown, it is important to explore the consequences of such hypotheses in the hope that astronomical observations can be used to place meaningful constraints.

The problem of SIDM halo formation has so far been studied primarily by numerical N-body experiments. Some of the first attempts to calculate the effect of the elastic scattering of SIDM on halo structure formation involved *isolated* halos which were assumed initially to follow the equilibrium profiles (e.g. NFW profile) found in collisionless N-body simulations of standard CDM (Burkert 2000; Kochanek & White 2001; both start from the Hernquist profile (Hernquist 1990) which is a good approximation to the NFW profile). Kochanek & White (2001), for instance, found that SIDM halos can form flat density cores within a relaxation time as expected, but also that the lifetime of such flat cores is only a few relaxation times. They concluded, therefore,

that most galactic halos would have undergone core collapse.

The effect of SIDM collisionality on halo structure has also been studied by Balberg, Shapiro, & Inagaki (2002, BSI hereafter) by solving 1D, quasi-static fluid equations. These authors also considered *isolated* halos like those in the N-body experiments mentioned above, adopting 1D, spherical symmetry, with non-cosmological boundary conditions. They treated the dynamics of SIDM by a fluid approximation developed previously in the study of stellar dynamics, derived from the Boltzmann equation, in which they modified the heat conduction term to handle the elastic scattering of the SIDM particle-particle interaction. They solved the spherically-symmetric, virialized “gravothermal fluid” equations of Lynden-Bell & Eggleton (1980), which include mass conservation, hydrostatic equilibrium, an equation for heat conduction, and the first law of thermodynamics. According to these equations, the halo is time-dependent because heat conduction causes it to evolve through a continuous sequence of hydrostatic equilibria. An analytical self-similar solution to these equations was found in the limit of large scattering mean free path – the limit where the mean free path is much larger than the size of the halo – following the derivation of Lynden-Bell & Eggleton (1980) for globular clusters. The BSI solution shows that secular evolution always takes a configuration in the long mean free path limit and drives it into the short mean free path regime. In order to track the evolution into the short mean free path regime, as well, BSI then used their similarity solution as the initial condition for a numerical solution of the same gravothermal fluid equations, but for finite scattering

cross-section. This approach made it possible to follow core collapse to a much more advanced stage than the N-body experiments could. From this, they concluded that the ultimate core collapse time was much larger than the relaxation time in the core, long enough even to exceed a Hubble time in some cases². Their estimated core collapse time is $t_{\text{coll}} \simeq 290 t_r$, which contradicts the result found by Burkert (2000) and Kochanek & White (2001) that the core collapse time was only a few relaxation times.

This apparent discrepancy in core collapse timescale between the study by BSI and the numerical N-body experiments (Burkert 2000; Kochanek & White 2001) may be attributed to the fact that their adopted initial conditions were different. In BSI, as mentioned, the initial condition was tuned to be in the extremely long mean free path limit, $\lambda_{\text{mfp}}/H \gg 1$, where λ_{mfp} is the mean free path and H is the gravitational scale height or roughly the halo size. This occurs when the system is either dilute enough or the scattering cross section (per unit mass) σ is small enough, since $\lambda_{\text{mfp}} \propto 1/(\sigma\rho)$. According to BSI, most of the collapse time is spent to reach the condition $\lambda_{\text{mfp}}/H \simeq 1$, and the halo density profile always has a flat core. By contrast, Kochanek & White (2001) started with a cuspy profile with parameters which corresponded to a condition $\lambda_{\text{mfp}}/H \simeq 0.1 - 3.0$. In this case, SIDM halo cores can quickly reach $\lambda_{\text{mfp}}/H \simeq 1$ or they are already in the short mean free path limit, which then requires only a few relaxation times for core collapse.

²In a follow-up paper, the authors showed how this process could lead to the formation of seeds for super-massive black holes (Balberg & Shapiro 2002).

In what follows, we will cover the whole range of σ and show that the observed dwarf-galaxy rotation curves are best-fit when the SIDM interaction has its maximal effect, which occurs when $\lambda_{\text{mfp}}/H \simeq 1$, so the regime of greatest interest may be that of Kochanek & White (2001). If so, then most isolated halos would, indeed, suffer core collapse within a Hubble time. However, the shared limitation of the analyses of BSI, Burkert (2000) and Kochanek & White (2001), that of non-cosmological boundary conditions, is a severe one. Cosmological infall may inhibit core collapse. If cosmological infall can delay core collapse substantially, previous estimates based on isolated halo models would change by shifting the time of the onset of core collapse until cosmological infall becomes negligible.

The effect of cosmological boundary conditions on SIDM halo formation has been studied numerically by cosmological N-body simulations, in which Gaussian random noise initial conditions for CDM were incorporated. Early work along these lines attempted to derive the maximal effect of collisionality by adopting the fully collisional limit which corresponds to ordinary gas dynamics (Yoshida et al. 2000a; Moore et al. 2000). The surprising result they reported was that simulations yielded density profiles with central cusps even steeper – with logarithmic slope close to -2 – than those in collisionless N-body simulations. Subsequent cosmological N-body experiments which treated the SIDM elastic scattering in more detail, however, reported that halo density profiles were flatter than those of either fully collisional or purely collisionless simulations (Yoshida et al. 2000b; Davé et al. 2001; Colín et al.

2002). They found that values of σ in the range $\sigma \simeq [0.1 - 5] \text{ cm}^2 \text{ g}^{-1}$ (the range of preferred σ varies among these works, but within less than an order of magnitude) produced SIDM halos with sufficient profile flattening to account for dwarf galaxy rotation curves, which did not suffer from the rapid core collapse identified in the earlier N-body experiments for isolated halos. Davé et al. (2001) speculated that this might be the result of cosmological infall, which was absent from the calculations of isolated halos. In addition, Yoshida et al. (2000b) found that SIDM collisions in cluster-sized halos would be more frequent than in dwarf-sized halos, thus producing relatively larger cores in clusters, while observations tend to show that dwarfs and LSBs show relatively larger cores than clusters. This led them to suggest that the scattering cross section be velocity-dependent ($\sigma \propto 1/v$) so that more massive halos would have a smaller degree of density profile flattening. Later, Colín et al. (2002) tested this hypothesis and confirmed that it could match observed core sizes from dwarfs to galaxy clusters.

Further study of the formation and evolution of SIDM halos is warranted to resolve the issues raised by previous work and put the subject on a firmer theoretical footing. On the one hand, the numerical N-body simulations and 1D semi-analytical treatment mentioned above of isolated halos with non-cosmological boundary conditions are unable to address the important effects of cosmological infall. On the other hand, the fully cosmological N-body simulations which have been performed of halos that arise during large-scale structure formation in the SIDM model have so far been limited by numerical

resolution and dynamic range. As a result, simulation results published to date do not attempt a detailed enough comparison with observed galactic rotation curves to determine if SIDM halos can really match them or to give a very reliable constraint on the SIDM cross section. Such simulations do not afford enough insight into the underlying dynamical processes which govern the halo structure, either. Finally, the wide range of typical collapse epochs expected in a CDM universe for the wide range of halo masses extending from dwarf galaxies to clusters suggests that the effect of the SIDM interaction may be halo-mass-dependent; this dependence has not yet been adequately explored.

Towards this end, we have derived a fully cosmological model for the origin and evolution of CDM halos in the presence of nongravitational collisionality (i.e. elastic scattering). We have combined the fluid approximation of BSI with the spherical infall model for cosmological perturbation growth to yield fully time-dependent, detailed similarity solutions for SIDM halos, for arbitrary degree of collisionality. We shall apply these solutions to test the hypothesis that cosmological infall retards the core collapse of SIDM halos, and compare the predicted SIDM halo profiles with the mass profiles inferred from dwarf galaxy rotation curves. This will enable us to place much better quantitative constraints on the SIDM cross section and better assess the validity of the SIDM model.

Subsequent to the original suggestion by Spergel & Steinhardt (2000) and the exploration described above of the halo structure which results, related work has focused on constraining the SIDM hypothesis by its implica-

tions for other astrophysical phenomena or attributing density flattening to more complicated CDM dynamics or gas dynamical feedback effects within the standard CDM picture. There seem to be strong observational constraints on the possible range of σ . Gnedin & Ostriker (2001) ruled out a range of σ , $\sigma = [0.3 - 10^4] \text{ cm}^2 \text{ g}^{-1}$, based on their calculation of the evaporation time of the dark matter halos of elliptical galaxies in the clusters. Natarajan et al. (2002) rule out all values of $\sigma > 42 \text{ cm}^2 \text{ g}^{-1}$ by comparing the predicted truncation radii of SIDM halos inside clusters by ram-pressure stripping to those of observed halos which they obtain using cluster gravitational lensing observations. Hennawi & Ostriker (2002) conclude that if $\sigma \gg 0.02 \text{ cm}^2 \text{ g}^{-1}$, the supermassive black holes in the centers of galactic halos would be more massive than observed. Along the line of explaining flattened cores within the standard CDM picture (see Primack 2003 for recent review), El-Zant et al. (2004), as in El-Zant et al. (2001), investigate the effect of dynamical friction by clumpy substructure associated with baryonic dissipation and show that a flat core can be generated. Weinberg & Katz (2002) and Holley-Bockelmann, Weinberg, & Katz (2003) claim that soft cores can be induced by the presence of a CDM bar structure. Hayashi et al. (2004) argue that the gas rotation speed in a galactic disk may be different from the dark matter circular velocity, which would, therefore, be wrongfully interpreted as implying the existence of soft cores. Dynamical feedback effects from supernova explosions is another possibility (Navarro, Eke, & Frenk 1996). Observationally, related to the missing satellite problem, the gravitational lensing flux anomaly seems to require clumpy,

dark substructures (Metcalf & Zhao 2002; Dalal & Kochanek 2002; Keeton, Gaudi, & Petters 2003; Mao et al. 2004), even though no firm conclusion has been established yet.

Nevertheless, we believe that SIDM is still a viable candidate for dark matter. As we shall discuss below in §3.1.8, the previous analyses restricting σ are subject to significant caveats. It is meaningful to study this subject because it can shed light on the nature of dark matter whose origin we do not know yet, and simply because CDM problems are far from reaching a firm conclusion. Also, the research effort on SIDM has not yet reached the level of that on collisionless CDM.

3.1.2 Fluid approximation of SIDM halos

We use the “fluid approximation”, which we have described in § 2.2, to derive a cosmological model for formation and evolution of SIDM halos. Toward this end, in § 3.1.2.1, we describe how the fluid conservation equations (eqs. [2.20] - [2.22]) can be modified to incorporate the effect of SIDM collisionality. We then describe, in § 3.1.2.2, the shock jump conditions in the presence of SIDM collisionality.

3.1.2.1 The effect of SIDM collisionality

We first formulate the effect of SIDM collisionality. We adopt a simple, heuristic approach to account for the heat conduction as a result of finite cross-section. This will change the energy conservation equation (equ. [2.22])

to

$$\frac{D}{Dt}\left(\frac{3p}{2\rho}\right) = -\frac{p}{\rho} \frac{\partial}{r^2 \partial r}(r^2 u) - \nabla \cdot \mathbf{f}, \quad (3.1)$$

where \mathbf{f} is the heat flux.

The heat flux resulting from SIDM interaction has been derived by BSI. We briefly describe its derivation. When the scattering mean free path is much smaller than the system size (short mean free path limit, or diffusion limit), the heat flux (equivalent to $\frac{L}{4\pi r^2}$ in BSI) reads

$$\mathbf{f}_{\text{smfp}} = -\frac{3b}{2\sigma} \sqrt{\frac{p}{\rho}} \frac{\partial}{\partial r} \left(\frac{p}{\rho} \right) \hat{r}, \quad (3.2)$$

where b is an effective impact parameter of order unity, which is 1.002 for elastic scattering of hard spheres. On the contrary, when the mean free path is much larger than the system size (long mean free path limit), the proper length scale of heat transfer is not the mean free path (a multiple of the system size) but the system size, while the time scale is still the relaxation time. This results in

$$\mathbf{f}_{\text{lmfp}} = -\frac{3}{2} ab\sigma \sqrt{\frac{p}{\rho}} \frac{p}{4\pi G} \frac{\partial}{\partial r} \left(\frac{p}{\rho} \right) \hat{r}, \quad (3.3)$$

where $a = 2.26$ for elastic scattering of hard spheres.

In the end, we use a hybrid expression which is roughly valid in the intermediate regime as well as in two extreme regimes (short mean free path

limit and long mean free path limit)³,

$$\mathbf{f} = -\frac{3}{2}ab\sigma\sqrt{\frac{p}{\rho}}\left(a\sigma^2 + \frac{4\pi G}{p}\right)^{-1}\frac{\partial}{\partial r}\left(\frac{p}{\rho}\right)\hat{r}. \quad (3.4)$$

Throughout this work, we adopt $a = 2.26$ and $b = 1.002$.

3.1.2.2 Shock jump conditions

As we have shown in § 2.2, fluid conservation equations can be used and we expect an accretion “shock” to occur. Across the shock, the matter, momentum and energy fluxes should all be continuous. Mathematically, a flux is a term acted upon by $\frac{\partial}{\partial r}$ in the conservation equations expressed in Eulerian coordinates.

In the adiabatic case⁴, therefore, we obtain the usual adiabatic shock jump conditions from equations (2.20) - (2.22):

$$[\rho\bar{u}] = 0, \quad (3.5)$$

$$[p + \rho\bar{u}^2] = 0, \quad (3.6)$$

$$\left[\rho\bar{u}\left(\frac{3p}{2\rho} + \frac{1}{2}\bar{u}^2 + \frac{p}{\rho}\right)\right] = 0, \quad (3.7)$$

where $[A] \equiv A(\text{preshock}) - A(\text{postshock})$, \bar{u} ($= u - u_s$) is the bulk radial velocity in the shock frame, and equation (3.7) comes from equation (2.22) if expressed in Eulerian coordinates by converting $\frac{D}{Dt}$ into $\frac{\partial}{\partial t} + u\frac{\partial}{\partial r}$.

³Note that the intermediate regime described by equation (3.4) is indeed a mere interpolation of two different regimes. We believe, however, that this is a good approximation: the intermediate value should not be too different from this smooth and continuous interpolation of two regimes.

⁴We will use the term “adiabatic” for the case where there is no heating mechanism (e.g. conductive heating due to elastic scattering) other than the shock heating.

For an SIDM case, as the heat conduction is included, the energy jump condition will instead be

$$\left[\rho \bar{u} \left(\frac{3p}{2\rho} + \frac{1}{2} \bar{u}^2 + \frac{p}{\rho} + f \right) \right] = 0, \quad (3.8)$$

where $\mathbf{f} = f \hat{r}$.

3.1.3 Self-similar model for SIDM halos in the matter-dominated era

In this section we first show that formation and evolution of SIDM halos in galactic scale are well approximated by self-similar equations. We then apply the fluid approximation to the problem and derive a set of ordinary differential equations. We will explain in detail how to solve these equations with proper boundary conditions.

3.1.3.1 Self-similarity of SIDM halos

In §2.3.2, we described how a self-similar collapse model fits in cosmology by relating the logarithmic slope of the power spectrum, n , to the initial linear overdensity profile parametrized by ε . We, therefore, should first know what n is relevant to the problem we solve.

When collisionality of particles enters the system, its corresponding length scale comes into play, which in general does not grow in proportion to r_{ta} . Similarly, a new time scale will enter the system. However, we can still make the system self-similar after the addition of collisionality by some fine-tuning. The conductive heating term $\nabla \cdot \mathbf{f}$ enters the energy equation, and

it should have a time dependence same as that of the adiabatic change of the thermal energy $\rho \frac{d}{dt} \left(\frac{3p}{2\rho} \right)$. Noting that $\rho \frac{d}{dt} \left(\frac{3p}{2\rho} \right) \propto r_{\text{ta}}^2 t^{-5}$ and $\nabla \cdot \mathbf{f} \propto r_{\text{ta}}^3 t^{-7}$, the condition

$$\xi = 2, \quad \varepsilon = \frac{1}{6} \quad (3.9)$$

preserves self-similarity of the system. This condition, $\varepsilon = 1/6$, is equivalent to $n = -2.5$, which can be seen from equation (2.28). The turnaround radius and mass grow in time as

$$r_{\text{ta}} \propto t^2, \quad M \propto t^4. \quad (3.10)$$

Now we find an intriguing coincidence. As described in §2.3.2, $n = -2.5$ is a good approximate value for halos of galactic mass. SIDM halos in galactic scales are, therefore, well described by self-similar equations. The following sections are dedicated to the detailed description of SIDM similarity solutions.

3.1.3.2 Basic equations and problem solving scheme

Under the condition of self-similarity, one can convert seemingly time-dependent equations into ordinary differential equations by properly scaling physical parameters. The turnaround radius r_{ta} is a natural choice for a length scale. With time t and the turnaround radius r_{ta} , we define dimensionless physical quantities – radius, velocity, density, pressure, mass and heat flux – as follows:

$$\lambda = r/r_{\text{ta}}, \quad (3.11)$$

$$V(\lambda) = v / \left(\frac{r_{\text{ta}}}{t} \right), \quad (3.12)$$

$$D(\lambda) = \rho/\rho_b, \quad (3.13)$$

$$P(\lambda) = p/\left[\rho_b\left(\frac{r_{\text{ta}}}{t}\right)^2\right], \quad (3.14)$$

$$M(\lambda) = m/\left(\frac{4\pi}{3}\rho_b r_{\text{ta}}^3\right), \quad (3.15)$$

$$F(\lambda) = f/\left[\rho_b\left(\frac{r_{\text{ta}}}{t}\right)^3\right]. \quad (3.16)$$

Collapsing shells, which are assumed to be cold initially, obey Newton's law

$$\frac{d^2r}{dt^2} = -\frac{Gm}{r^2} \quad (3.17)$$

where m is the mass enclosed by radius r . For the initial density perturbation defined by equation (2.23), this Newtonian motion can be described by a set of parametric equations, as follows (Abadi, Bower, & Navarro 2000; see also Bertschinger 1985, for case of $\varepsilon = 1$):

$$\lambda = \sin^2(\theta/2) \left(\frac{\theta - \sin \theta}{\pi}\right)^{-\xi}, \quad (3.18)$$

$$V(\lambda) = \lambda \frac{\sin \theta(\theta - \sin \theta)}{(1 - \cos \theta)^2}, \quad (3.19)$$

$$D(\lambda) = \frac{9}{2} \frac{(\theta - \sin \theta)^2}{(1 - \cos \theta)^3(1 + 3\varepsilon\chi)}, \quad (3.20)$$

$$M(\lambda) = \lambda^3 \frac{9}{2} \frac{(\theta - \sin \theta)^2}{(1 - \cos \theta)^3}, \quad (3.21)$$

where $\chi = 1 - (3/2)(V(\lambda)/\lambda)$. Equations (3.18) - (3.21) therefore describe preshock motion.

The postshock motion of shells is described by full hydrodynamic equations. Equations (2.20), (2.21), (3.1), (3.4) and the definition of the infinitesimal mass $dm = 4\pi r^2 dr$ can be written with these dimensionless quantities as a set of ordinary differential equations:

$$(V - 2\lambda)D' + DV' + \frac{2DV}{\lambda} - 2D = 0, \quad (3.22)$$

$$(V - 2\lambda)V' + V = -\frac{P'}{D} - \frac{2M}{9\lambda^2}, \quad (3.23)$$

$$(V - 2\lambda) \left(\frac{P'}{P} - \frac{5D'}{3D} \right) = -\frac{10}{3} - \frac{2(F\lambda^2)'}{3P\lambda^2}. \quad (3.24)$$

$$F = -\frac{3ab}{2Q'} \left(a + \frac{2}{3Q'^2 P} \right)^{-1} \sqrt{\frac{P}{D}} \frac{d}{d\lambda} \left(\frac{P}{D} \right), \quad (3.25)$$

$$M' = 3\lambda^2 D, \quad (3.26)$$

where the prime indicates differentiation with respect to λ , and the nondimensional collisionality parameter Q' is defined as $Q' \equiv \sigma \rho_b r_{\text{ta}}$. We will later use a nondimensional constant $Q \equiv \sigma \rho_b r_s = \lambda_s Q'$, which is more directly related to the collision rate of an SIDM particle in a virialized structure with the shock radius r_s . For instance, the number of collisions a particle experiences in a time Δt is given as $N \equiv \sigma \rho v_{\text{rel}} \Delta t$ (e.g. Burkert 2000). The conversion of Q into N is straightforward:

$$N = \frac{\rho}{\rho_b} \frac{v_{\text{rel}} \Delta t}{r_s} Q = a \sqrt{\frac{p}{\rho}} \frac{\rho}{\rho_b} \frac{\Delta t}{r_s} Q. \quad (3.27)$$

Here we used the relation $v_{\text{rel}} = a \sqrt{p/\rho}$, where $a = 2.26$ again, which relates the average thermal velocity to the relative velocity for particles interacting elastically as hard spheres (eqs. [7.10.13], [12.2.12] in Reif 1965).

Different solutions arise for different values of $Q(Q')$. To solve the coupled ordinary differential equations (eqs. [3.22] - [3.26]), we need to connect the preshock values given by equations (3.18) - (3.21 with $\xi = 2$) to the postshock values. This is described by the shock jump conditions (eqs. [3.5], [3.6], and [3.8]) and the continuity of mass, which are expressed by nondimensional variables as

$$D_2 = \left(1 - \frac{2F_2}{P_2(V_1 - 2\lambda_s)}\right)^{-1} 4D_1, \quad (3.28)$$

$$P_2 = \left(\frac{3}{4} + \frac{F_2}{2P_2(V_1 - 2\lambda_s)}\right) D_1(V_1 - 2\lambda_s)^2, \quad (3.29)$$

$$V_2 = 2\lambda_s + \left(1 - \frac{2F_2}{P_2(V_1 - 2\lambda_s)}\right) \frac{1}{4}(V_1 - 2\lambda_s), \quad (3.30)$$

$$M_2 = M_1, \quad (3.31)$$

where the subscript 1 denotes preshock values, while 2 denotes postshock values. Note that $P_1 = 0$ and $F_1 = 0$ because we assume cold infall. Note also that without terms containing F_2 , equations (3.28) - (3.31) are identical to the adiabatic jump conditions for $\gamma = 5/3$ gas (see eqs. [6a] - [6d] in Abadi et al. 2000). These additional terms arise because of finite conductivity in the postshock region. Finally, the inner boundary conditions are

$$M(\lambda = 0) = 0, \quad (3.32)$$

$$V(\lambda = 0) = 0, \quad (3.33)$$

and

$$F(\lambda = 0) = 0. \quad (3.34)$$

In principle, the fluid equations (eqs. [3.22] - [3.26]), preshock equations (eqs. [3.18] - [3.21]), jump conditions (eqs. [3.28] - [3.31]), and inner boundary conditions (eqs. [3.32] - [3.34]) yield a unique solution. This solution was obtained numerically, by iteration, as follows. We arbitrarily chose the shock location λ_s (close to that of the adiabatic solution), central density $D(0)$ and central pressure $P(0)$. We then integrated differential equations from $\lambda = 0$ outward, using the LSODE (Livermore Solver for Ordinary Differential Equations), in which case variables behaved well. At the chosen shock location, we then obtained preshock values using the jump condition. If these values differed from those obtained from equations (3.18) - (3.21), we went back and chose a different λ_s , $D(0)$, and $P(0)$. We iterated this process until the jump condition was satisfied to a given error tolerance. This way we could get approximate solutions for several selected values of Q (listed in Table 3.1), all of which satisfied the shock jump conditions (eqs. [3.28] - [3.31]) to less than 0.1% error. This was a very tedious and time-consuming job, but automation of the iterations made it possible to achieve this goal.

In practice we could not perform integration from $\lambda = 0$ because the differential equations have a coordinate singularity at the center. Instead, we performed the integration from some small λ , using asymptotic forms for $\lambda \ll 1$: $D \simeq D(0)$, $P \simeq P(0)$, $V \simeq \frac{2}{3}\lambda$, $M \simeq D(0)\lambda^3$, and $F \simeq -\frac{5}{3}P(0)\lambda$.

3.1.4 Self-similar halos with conduction($\varepsilon = 1/6$): an analytical Model for SIDM halos

3.1.4.1 Low- Q regime

We define the low- Q regime as $Q \leq Q_{\text{th}} = 7.35 \times 10^{-4}$. All the solutions have an isothermal, flat-density core, except for extremely small Q , where the system undergoes adiabatic collapse just as it would in the absence of SIDM conductivity. In this regime, as Q increases, the core density and pressure decrease. In other words, higher SIDM collisionality corresponds to a flatter core. This trend is also observed in the temperature profile. As Q increases, heat is more effectively transferred into the center to equalize the temperature. Dependence of the central density, temperature and the location of the shock on Q is listed in Table 3.1 (see also Fig. [3.1]).

This regime roughly corresponds to the long mean free path limit. In this case, the heat flux is an increasing function of the SIDM cross section σ (eq. [3.3]). As an increase in Q is achieved by an increase in σ , the heat flux also increases correspondingly. In §3.1.5, a more detailed description will be given about the quantitative relation between the low(high)- Q regime to the long(short) mean free path limit.

In §3.1.7.2, we will also show that cosmological SIDM N-body simulations to date have been performed only in the low- Q regime. They see a monotonic behavior of the halo profile depending on σ – as σ increases, core density decreases. In the next section, we will show that there is an additional regime, the high- Q regime, where this behavior is reversed.

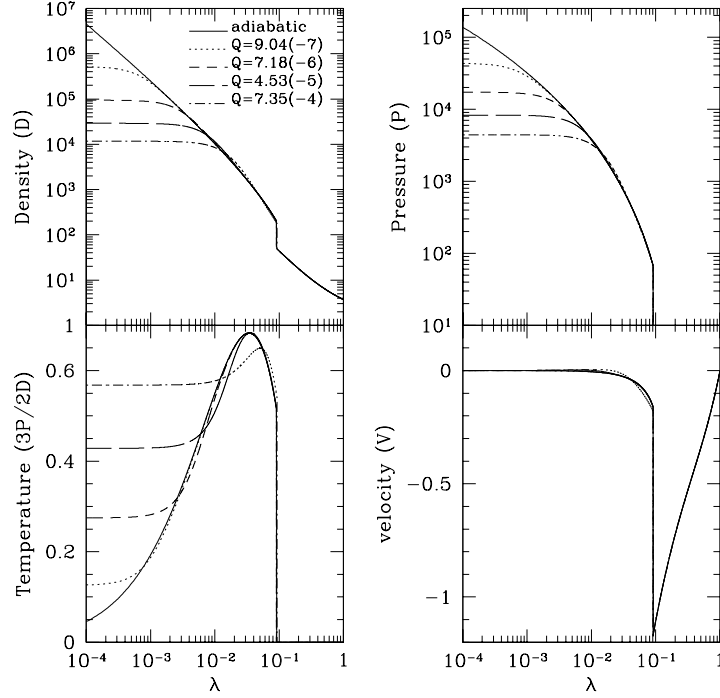


Figure 3.1: Similarity solution dimensionless profiles for low- Q regime. $Q = 0$ means “no conduction,” i.e. “adiabatic” post-shock gas. As Q increases, core density decreases and core temperature increases. Dimensionless similarity variables follow the definitions in Bertschinger (1985).

3.1.4.2 High- Q regime

In the high Q regime, solutions have $Q \geq Q_{\text{th}} = 7.35 \times 10^{-4}$. Once again, all the solutions have an isothermal, flat-density core, except for an extremely high Q case. In the high- Q regime, however, as Q (or σ) increases, the core density increases (Fig. [3.2]; Table 3.1), contrary to the behavior observed for the low- Q regime. Therefore, Q_{th} gives the solution with the minimum possible core density $\rho_{\text{core}} \simeq 10^4 \rho_b$.

Table 3.1: Central parameters and the shock location for different Q solutions. This table lists the whole range of Q .

Q	Q/Q_{th}	$D(0)$	$\frac{3P(0)}{2D(0)}$	λ_s
0	0	∞	0	9.0434(-2)
9.04(-7)	1.23(-3)	5.199(5)	1.258(-1)	9.0434(-2)
7.18(-6)	9.77(-3)	9.426(4)	2.747(-1)	9.0434(-2)
4.53(-5)	6.16(-2)	2.914(4)	4.289(-1)	9.060(-2)
7.35(-4)	1	1.169(4)	5.681(-1)	9.260(-2)
1.25(-2)	1.70(1)	2.882(4)	4.346(-1)	9.623(-2)
4.37(-2)	5.95(1)	9.515(4)	2.540(-1)	9.294(-2)
1.37(-1)	1.86(2)	5.199(5)	1.062(-1)	9.133(-2)
∞	∞	∞	0	9.0434(-2)

This behavior occurs because the core of the halo is now in the short mean free path regime. In this case, contrary to the low- Q regime, the hybrid conduction term, equation (3.4), converges to the expression valid in the short mean free path limit, equation (3.2). An increase in Q or σ , therefore, results in a decrease in \mathbf{f} . Physically, the mean free path decreases as Q or σ increase, and it results in reducing the heat conduction.

For an extremely high Q (or σ), we found that the solution becomes identical to that of the adiabatic infall case. This result agrees qualitatively with the result by Yoshida et al. (2000a) and Moore et al. (2000), where they performed a smoothed particle hydrodynamics simulation, corresponding to the fluid limit of an infinite cross section. What they found in halos was a density cusp instead of a flat-density core. Quantitatively, our result does not fully agree with their result in which they find a profile even steeper than that of the collisionless case. As pointed out by Yoshida et al. (2000a), this

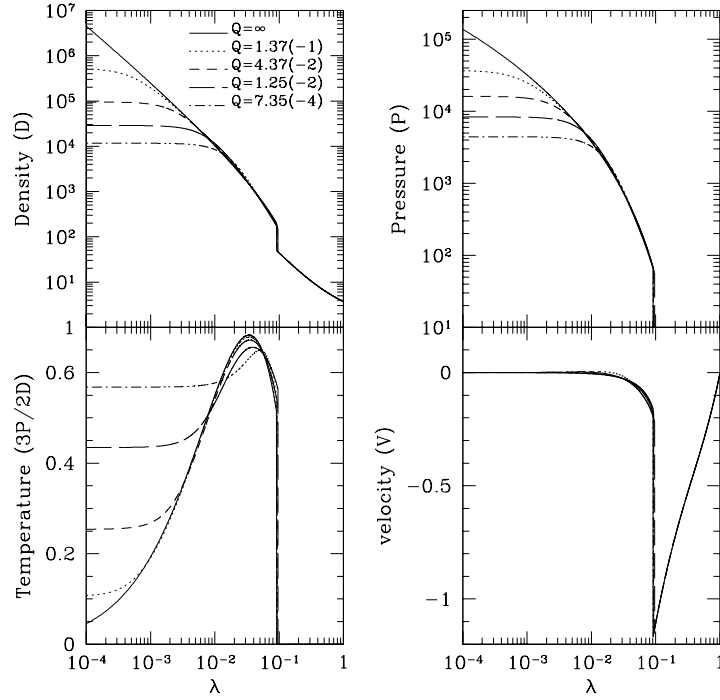


Figure 3.2: Similarity solution dimensionless profiles for the high- Q regime. Profiles are indistinguishable from those in Figure 3.1, even though the Q values are quite different. The effect of Q is reversed compared to the low- Q regime: as Q increases, core density increases and core temperature decreases.

may be attributed to the fact that small-scale shocks arise in the case of the fluid regime, thus increasing the entropy and ultimately steepening the central density. Our model is based upon an assumption that mass accretion is smooth and, therefore, cannot reproduce this effect.

3.1.5 Meaning of the collisionality parameter Q

We have showed that solutions are parametrized by the collisionality parameter Q , and also that there exist two regimes divided by a threshold value Q_{th} . To understand the physical meaning of Q , we now describe two relevant quantities: mean free path and the number of scatterings an SIDM particle experiences per Hubble time.

We first show that the ratio of the mean free path to the gravitational scale height (to be explained below) in the center is very closely related to Q , and it provides a very clean explanation of the behavior of the similarity solution. In previous sections, we explained the opposite trends observed in the two different regimes in terms of the heat flux \mathbf{f} (equ. [3.4]). The dependence of \mathbf{f} is determined by the ratio $\eta^2 \equiv (4\pi G/p)/(a\sigma^2)$: $\mathbf{f} \propto \sigma$ for $\eta^2 \gg 1$, and $\mathbf{f} \propto 1/\sigma$ for $\eta^2 \ll 1$. We find that, indeed, η is the ratio of two length scales, the mean free path and the gravitational scale height. The gravitational scale height (BSI),

$$H \equiv \sqrt{\sigma_V^2/(4\pi G\rho)} = \sqrt{p/(4\pi G\rho^2)}, \quad (3.35)$$

is a rough measure of the size of a given self-gravitating system, where σ_V^2 is the velocity dispersion – also note, however, that equation (3.35) determines the *local* gravitational scale height. In terms of the mean free path $\lambda_{\text{mfp}} \equiv 1/(\rho\sigma)$ and $a = 2.26$ as in equation (3.3), $\eta = \lambda_{\text{mfp}}/(\sqrt{a}H)$. We find that $\eta = 1$ at the center for $Q = Q_{\text{th}}$. η at the center monotonically increases as Q increases. The low- Q regime then corresponds to a condition $\eta > 1$, and the high- Q to

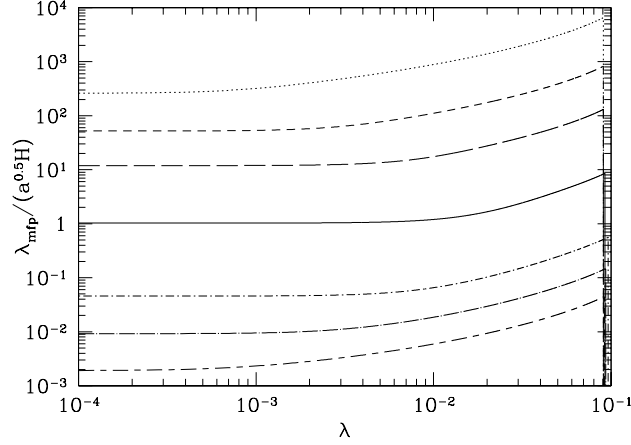


Figure 3.3: The parameter η versus dimensionless radius λ , where $\eta = \lambda_{\text{mfp}}/(\sqrt{a}H)$, the ratio of mean free path to gravitational scale height, for different values of Q . From top to bottom, each curve corresponds to $Q/Q_{\text{th}} = 1.23 \cdot 10^{-3}$, $9.77 \cdot 10^{-3}$, $6.16 \cdot 10^{-2}$, 1, 17, 59.4, and 186, respectively. The constant $a = 2.26$.

a condition $\eta < 1$. Dependence of η on Q , as well as its radial variance, is plotted in Figure 3.3.

The number of scatterings that an SIDM particle experiences during the age of the universe, which we denote by N , is also an interesting quantity. As higher Q means a more frequent scattering, N also shows a monotonic dependence on Q (Fig. [3.4]) as η does. According to equation (3.27), it can be shown that N is expressible in terms of dimensionless quantities as

$$N = N_{0,\text{th}} \sqrt{\frac{DP}{(DP)_{0,\text{th}}}} \left(\frac{Q}{Q_{\text{th}}} \right) = a \sqrt{DP} Q / \lambda_s, \quad (3.36)$$

where the subscript “0,th” refers to the value at $r = 0$ for $Q = Q_{\text{th}}$, and $N_{0,\text{th}} = 129$. It is interesting to see that $N_{0,\text{th}} \approx 100$ is required to achieve the

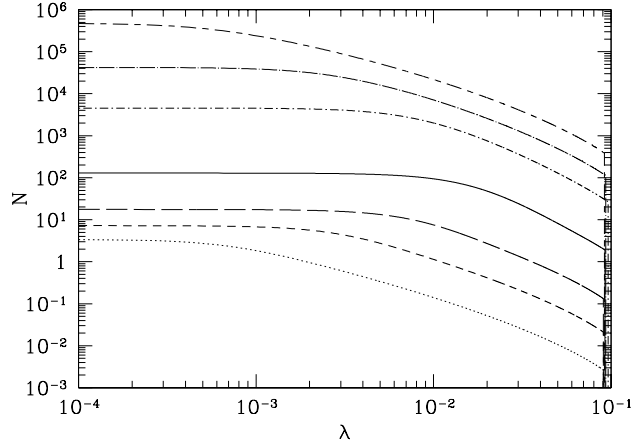


Figure 3.4: Number of scattering that an SIDM particle experiences during the age of the universe in dimensionless radius λ . From bottom to top, each curve corresponds to $Q/Q_{\text{th}} = 1.23 \cdot 10^{-3}$, $9.77 \cdot 10^{-3}$, $6.16 \cdot 10^{-2}$, 1, 17, 59.4, and 186, respectively.

maximal conductivity, namely $Q = Q_{\text{th}}$. We will handle the significance of this quantity in §3.1.7.2, when we compare our result to SIDM N-body simulation results.

Finally, we stress the importance of the radial variance of η and N . When $Q/Q_{\text{th}} \ll 1$ or $Q/Q_{\text{th}} \gg 1$, the system can be said, in a global sense, to reside in the long mean free path limit or in the short mean free path limit, respectively. When $Q/Q_{\text{th}} \approx 1$, however, such a global definition is not valid. In the $Q = Q_{\text{th}}$ solution, for instance, $\eta = 1$ at the center while $\eta \approx 10$ at the shock. N varies from ~ 100 at the center to ~ 2 at the shock. This example shows that a global assumption of the short (or long) mean free path limit is not always valid, which requires a more careful attention when $Q \simeq Q_{\text{th}}$. We

will handle this issue again in §3.1.8, with respect to the estimate on the ram-pressure stripping of substructure in a cluster environment made by Furlanetto & Loeb (2002a) and Natarajan et al. (2002).

3.1.6 Importance of cosmological infall

The SIDM core grows in size as a fixed fraction of the turnaround radius, as guaranteed from the beginning because of the self-similarity of the system.

Therefore, this model shows that cosmological infall at a certain rate can completely inhibit the gravothermal catastrophe of the core by constantly pumping hot material into the halo. This contradicts the prediction made in previous studies that the core would suffer gravothermal catastrophe in a Hubble time (e.g. Burkert 2000). Even when the infall rate is smaller than that required for our similarity solution ($M \propto t^4$), it will inhibit the core collapse to some extent. Only when the infall rate drops to a point where a system can be considered isolated will previous estimates of the timescale of collapse be valid. The net effect is a substantial delay of the collapse phase.

3.1.7 Application

3.1.7.1 Collisionality parameter as a function of σ and M

So far, we have described solutions in terms of Q . Now we seek a way to apply our solutions to practical problems. This is done by obtaining the dependence of Q on the scattering cross section σ and the mass of halos M .

From the Press-Schechter formalism, we find $Q = Q(\sigma, M)$ for “typical” halos of mass M , which collapse when $\sigma_M = \delta_{\text{crit}}$ (σ_M is the standard deviation of the density fluctuations at the collapse epoch $z_{\text{coll}}(M)$ according to linear perturbation theory after the density field is filtered on the scale M ; δ_{crit} is the value of overdensity linearly extrapolated to a moment when the nonlinear overdensity becomes infinite.) Usually these are called $1\text{-}\sigma_M$ fluctuations.

As the $\varepsilon = 1/6$ adiabatic infall solution has a shock at r_{564} , the mass contained inside r_{564} , M_{564} , is smaller than M_{200} , which is typically quoted in the literature. In other words, the shock location is displaced from r_{200} substantially. As r_s is a function of M and z_{coll} , in order to get $Q = Q(M, z_{\text{coll}})$, we first should relate M_{564} to M . We therefore need a model whose density profile extends at least to r_{200} . We use the “truncated isothermal sphere” (TIS) model (Shapiro, Iliev, & Raga 1999; Iliev & Shapiro 2001) for this purpose, for the following reasons: (1) it has a unique density profile, (2) all physical quantities are fully determined by the values of M and z_{coll} , (3) it has been proven to agree well with CDM prediction in many aspects, and (4) the average quantity (i.e. the average temperature) inside its own r_{564} is in a good agreement with that of our similarity solutions and of CDM N-body halos⁵. We use a convenient set of formulae given by Iliev & Shapiro (2001) to get $r_s = r_{564}(M)$ for a given halo of mass M at its collapse epoch. In this model,

⁵We find the same level of agreement between our similarity solutions and the N-body halos as was found between the TIS and N-body halos in Shapiro et al. (1999, see the mass-temperature relation in § 8.4).

the mass of the halo M is enclosed by the “truncation radius” r_t , given by

$$r_t = 187.2 \left(\frac{M}{10^{12} h^{-1} M_\odot} \right)^{1/3} \Omega_0^{-1/3} (1 + z_{\text{coll}})^{-1} h^{-1} \text{kpc}, \quad (3.37)$$

and we find that

$$M_{564} = 0.587M, \quad (3.38)$$

and

$$\begin{aligned} r_{564} &= 0.514 r_t \\ &= 96.22 \left(\frac{M}{10^{12} h^{-1} M_\odot} \right)^{1/3} \Omega_0^{-1/3} (1 + z_{\text{coll}})^{-1} h^{-1} \text{kpc}. \end{aligned} \quad (3.39)$$

Note that M in this model is equivalent to M_{130} . Equations (3.37), (3.38), and (3.39) are valid only when the universe is in the matter-dominated era. The mean matter density is in general given by

$$\rho_b(z) = \Omega_0 \rho_{0,\text{crit}} (1 + z)^3 = 1.88 \times 10^{-29} \Omega_0 (1 + z)^3 h^2 \text{g/cm}^3. \quad (3.40)$$

When the scattering cross section σ is a constant, Q also remains constant in a matter-dominated era where $\rho_b \propto t^{-2}$ if $\varepsilon = 1/6$ (or $r_s \propto t^2$). From the equations above, we find that

$$\begin{aligned} Q &= Q_{\text{th}} \left(\frac{\Omega_0}{0.27} \right)^{2/3} \left(\frac{\sigma}{218.5 \text{ cm}^2 \text{g}^{-1}} \right) \left(\frac{M}{10^{10} h^{-1} M_\odot} \right)^{1/3} \\ &\quad \times \left(\frac{h}{0.7} \right) \left(\frac{1 + z_{\text{coll}}}{1 + 2.09} \right)^2. \end{aligned} \quad (3.41)$$

Note that typical ($1\text{-}\sigma_M$ fluctuation) halos of $M = 10^{10} h^{-1} M_\odot$ collapse at $z_{\text{coll}} = 2.09$ in the currently-favored Λ CDM universe with $h = 0.7$, $\Omega_0 = 0.27$,

$\Omega_\Lambda = 0.73$ and $\sigma_8 = 0.9$. If we restrict the mass range of halos such that the high mass end will still collapse in the matter-dominated era – $z_{\text{coll}} \gtrsim 1$ – and the low mass end roughly satisfies the self-similarity, we should choose halos with masses $M \simeq [10^6 - 10^{12}] h^{-1} M_\odot$. In this mass range, equation (3.41) reads

$$Q \simeq [1.68 - 9.31] \times 10^{-4} \left(\frac{\sigma}{218.5 \text{ cm}^2 \text{ g}^{-1}} \right) \quad (3.42)$$

for a Λ CDM universe (see Fig. 3.5): for $\sigma = 218.5 \text{ cm}^2 \text{ g}^{-1}$, $Q = 1.68 \times 10^{-4}$ corresponds to $M = 10^6 h^{-1} M_\odot$, while $Q = 9.31 \times 10^{-4}$ corresponds to $M = 10^{11.62} h^{-1} M_\odot$. Here we applied the Press-Schechter formalism to obtain $z_{\text{coll}}(M)$. However, just for comparison, we also calculated Q for halos with $M \gtrsim 10^{12} h^{-1} M_\odot$, which typically have collapsed only recently. Such massive halos must be rare, high- σ fluctuations in order to collapse by the present, and we cannot apply our similarity model to these halos because their mass assembly deviates substantially from self-similar evolution. Note that the rarer the objects are, the higher the collapse redshift z_{coll} is, which in turn makes Q larger in equation (3.41). This trend can be seen in Figure 3.5.

3.1.7.2 Comparison with N-body simulation results

Consider the range of σ identified in the cosmological N-body simulation of SIDM by Davé et al. (2001): $\sigma = [0.56 - 5.6] \text{ cm}^2 \text{ g}^{-1}$. In a Λ CDM universe, this range of σ in equation (3.42) then yields the range

$$\begin{aligned} Q &\simeq [4.31 \times 10^{-7} - 2.39 \times 10^{-5}] \\ &\simeq [5.86 \times 10^{-4} - 3.25 \times 10^{-2}] Q_{\text{th}} \end{aligned} \quad (3.43)$$

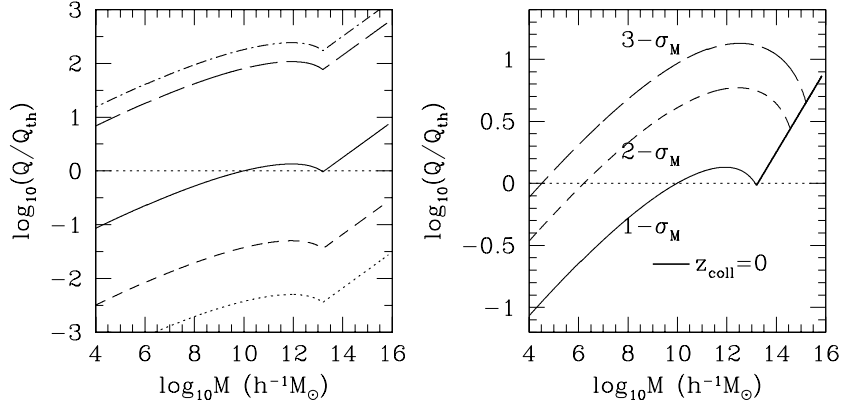


Figure 3.5: Left: Q vs. mass of halos at their typical formation epoch for different σ . From bottom to top, curves correspond to $\sigma = 0.56, 5.6, 218.5, 1.2 \times 10^4, 2.7 \times 10^4$ respectively. They all correspond to $1-\sigma_M$ density peaks (σ_M means the standard deviation of the density fluctuations filtered on mass scale M at the collapse epoch); Right: Q vs. mass of halos at their formation epoch for $\nu-\sigma_M$ ($\nu=1, 2, 3$) fluctuations with $\sigma = 218.5 \text{ cm}^2 \text{ g}^{-1}$. Cluster-sized halos observed at present will be clustered around the crossing point of the $3-\sigma_M$ line and $z_{\text{coll}} = 0$ line.

for halos with $10^6 h^{-1} M_{\odot} < M < 10^{12} h^{-1} M_{\odot}$. Here $Q = 4.31 \times 10^{-7}$ corresponds to $\sigma = 0.56 \text{ cm}^2 \text{ g}^{-1}$ and $M = 10^6 h^{-1} M_{\odot}$, while $Q = 2.39 \times 10^{-5}$ corresponds to $\sigma = 5.6 \text{ cm}^2 \text{ g}^{-1}$ and $M = 10^{11.62} h^{-1} M_{\odot}$.

The simulation results of Davé et al. (2001) reside in the low- Q regime, as seen in equation (3.43). Our solutions allow us to identify a corresponding range of Q -values in the high- Q regime for which the density profiles are indistinguishable from their low- Q counterparts. The range of solutions described by equation (3.43) can be matched by solutions with

$$Q \simeq [1.37 \times 10^{-2} - 0.17] \simeq [18.6 - 231] Q_{\text{th}}, \quad (3.44)$$

or $\sigma \simeq [1.2 \times 10^4 - 2.7 \times 10^4] \text{ cm}^2 \text{ g}^{-1}$. Here $Q = 1.37 \times 10^{-2}$ corresponds to $\sigma = 1.2 \times 10^4 \text{ cm}^2 \text{ g}^{-1}$ and $M = 10^6 h^{-1} M_\odot$, while $Q = 2.7 \times 10^{-2}$ corresponds to $\sigma = 2.7 \times 10^4 \text{ cm}^2 \text{ g}^{-1}$ and $M = 10^{12} h^{-1} M_\odot$.

Therefore, we predict that a cosmological N-body simulation of SIDM with $\sigma \simeq [1.2 \times 10^4 - 2.7 \times 10^4] \text{ cm}^2 \text{ g}^{-1}$ will produce results similar to those of the Davé et al. (2001)'s simulations. The nondimensional core density $D(0)$ corresponding to the range of Q found in this section lies in the range $D(0) \simeq [3.3 \times 10^4 - 7.4 \times 10^5]$, while the nondimensional core temperature $T_{\text{core}} \equiv \frac{3P(0)}{2D(0)}$ is in the range $T_{\text{core}} \simeq [0.11 - 0.41]$. However, in order to obtain observationally acceptable values, we should actually fit the implied rotation curves of our similarity solutions directly to the empirical data. This is the main topic of §3.1.7.3.

3.1.7.3 Rotation curve fitting

In this section, we find best-fitting similarity solutions which match the observed rotation curves of dwarfs and LSBs. To do so, we simply compare our similarity solutions to an empirical fit by Burkert (1995). Burkert found that a density profile given by

$$\rho(r) = \frac{\rho_0 r_0^3}{(r + r_0)(r^2 + r_0^2)}, \quad (3.45)$$

where ρ_0 and r_0 are free parameters which represent the central density and a scale radius, respectively, matches halo density profiles which are derived from the observed rotation curves of dwarf galaxies. Recent studies of high-

resolution H α rotation curves of dwarfs and LSBs confirm this result (Marchesini et al. 2002; see also references therein): they use a “hybrid” of H α and HI rotation curves which can extend from the center to r_{\max} , and find that the Burkert profile is the best fit for this range.

For fitting purposes, one should specify a radius where the circular velocity ($v = \sqrt{Gm/r}$) is the same for different halo models. In other words, local density may vary but the mass enclosed by such a radius – let us denote it by the “normalization radius” r_n – should be the same. We choose $r_n = r_{564}$, the “shock radius” of our similarity solutions, to find the best-fitting similarity solution to the Burkert profile. In this case, the “concentration parameter” $c_{564, \text{Burkert}} \equiv r_{564}/r_0$ is the only free parameter. The goodness of a fit is observed through the relative mean square deviation,

$$\chi^2/\nu \equiv \sum_i \left(\frac{v(r_i) - v_{\text{Burkert}}(r_i)}{v_{\text{Burkert}}(r_i)} \right)^2 / N, \quad (3.46)$$

where r_i is the radius of the i th data point and N is the number of such points.

We find that the solution with $Q = Q_{\text{th}}$ is best fit to the Burkert profile, as seen clearly in Figure 3.6 and Table 3.2⁶⁷. As shown in the right

⁶We find the same answer, that the Q_{th} solution is the best-fit to the Burkert profile, when we relax the constraint $r_n = r_{564}$ and assume that the two parameters, ρ_0 and r_0 , are both free.

⁷The values of χ^2/ν shown in Table 3.2 show the relative quality of the fits of the Burkert profile to our self-similar SIDM profiles for different values of Q . In order to interpret these values in an absolute sense to determine if the fits are acceptable, we need to know the uncertainty of the fit of the Burkert profile to the observational data points. For example, if the 1- σ error bars are all a fraction f of the value of the data points, then the quantity $f^{-2}(\chi^2/\nu)$ should be small, i.e. $\lesssim 1$, for the theoretical curves to be a good fit at the 1- σ level. Since $(\chi^2/\nu)_{Q_{\text{th}}} = 2.06 \times 10^{-4}$, the SIDM profile for $Q = Q_{\text{th}}$ is a good fit to the data as long as $f \gtrsim 0.014$.

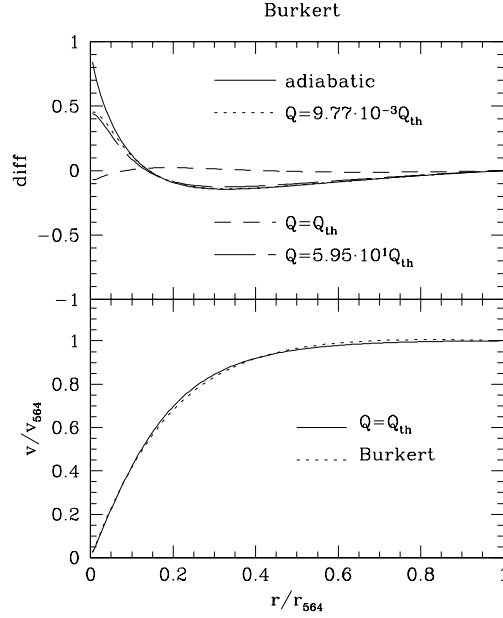


Figure 3.6: Rotation curve fitting. The upper left panel compares several different Q -solutions to the Burkert profile, normalized to r_{564} . The lower left panel shows the best-fitting solution to the Burkert profile, namely the Q_{th} solution. The right panel compares various halo models to the Burkert profile, normalized to r_{max} . It has the Q_{th} profile in r and v in units of $r_{\text{max,Burkert}} = 0.835 r_{564,\text{SIDM}}$ and $v_{\text{max,Burkert}} = 1.01 v_{564,\text{SIDM}}$, respectively, for the same profile as plotted in the lower left panel. In both boxes, the top panel shows the relative difference of a given profile, $(v - v_{\text{Burkert}})/v_{\text{Burkert}}$. The line types of the upper right panel follows the meaning of those in the lower right panel.

Table 3.2: Best-fitting concentration parameter of the Burkert profile and χ^2/ν . χ^2/ν is normalized by the value found for Q_{th} solution, $(\chi^2/\nu)_{Q_{\text{th}}} = 2.06 \times 10^{-4}$, the minimum.

Q/Q_{th}	$c_{564,\text{Burkert}}$	$(\chi^2/\nu)/(\chi^2/\nu)_{Q_{\text{th}}}$
0	5.51	4.72(2)
1.23(-3)	5.51	3.86(2)
9.77(-3)	5.49	1.36(2)
6.16(-2)	4.98	2.51(1)
1	3.95	1
1.70(1)	5.17	1.11(1)
5.95(1)	5.64	9.82(1)
1.86(2)	5.59	2.99(2)
∞	5.51	4.72(2)

panel of Figure 3.6, when $Q = Q_{\text{th}}$, the SIDM halo rotation curve is virtually indistinguishable from the Burkert profile at all radii $r \leq r_{\text{max}}$, by contrast with the strong disagreement at small radii between the Burkert profile and the NFW and Moore profiles, respectively. Since the $Q = Q_{\text{th}}$ solution has the most effective conductivity, which is closest to an isothermal structure among the similarity solutions, we argue that dwarfs and LSBs described by the Burkert profile are systems which are almost fully relaxed. This argument is supported by the fact that the TIS solution is almost identical to the Burkert profile (see Fig. [3.6]; also refer to Iliev & Shapiro 2001). The TIS solution is obtained by assuming that the system has a uniform temperature, isotropic random velocity, and the minimum possible energy, which in effect is equivalent to assuming a fully relaxed system. The solution with $Q = Q_{\text{th}}$ corresponds to the most relaxed system among our similarity solutions.

3.1.7.4 High value of σ : Contradiction with SIDM N-body simulation results?

An attempt to identify the range of SIDM cross section required to produce density profiles in agreement with dwarf galaxy rotation curves was previously made using N-body simulations of SIDM halo formation from Gaussian-random-noise cosmological density fluctuations (Davé et al. 2001; Yoshida et al. 2000b). These N-body results also indicated that, for this range of SIDM cross section, larger mass halos (i.e. from the Milky Way to clusters) produce density profiles with flattened cores which are even more pronounced than those of dwarf galaxies. Since astronomical evidence suggests that such large halos have relatively smaller cores, if any, than dwarf galaxies, this has led to the suggestion that the SIDM cross section must depend upon the relative velocity of the scattering events, decreasing with increasing velocity to suppress this effect in larger halos (e.g. Colín et al. 2002). How do our self-similar solutions for SIDM halo formation compare with these N-body results?

The value of Q in the similarity solutions which best fits the dwarf galaxy rotation curves, Q_{th} , corresponds to a value of the SIDM cross section when we identify the halo mass and redshift to which we apply the similarity solution, as described above in § 3.1.7.1. For halos of mass $M \simeq 10^{10}h^{-1}M_{\odot}$, which roughly represents the mass of dwarfs and LSBs observed, the solution with $Q = Q_{\text{th}}$ implies that $\sigma \simeq 218.5 \text{ cm}^2\text{g}^{-1}$, if the observed galaxies formed at the typical epoch for their mass scale (i.e. $1\text{-}\sigma_M$ fluctuations). This value is significantly larger than the range of acceptable cross section values reported

for the N-body results for SIDM halos by Davé et al. (2001) (equ. [3.43]) and similar results by Yoshida et al. (2000b).

Such discrepancy is observed also in N , the number of scatterings that an SIDM particle experiences during the age of the universe. Yoshida et al. (2000b) report that $N \simeq 1 - 10$ is enough to generate a soft core in their N-body SIDM halos. We have seen in § 3.1.7.3, however, that $Q \approx Q_{\text{th}}$ is required to find acceptably flattened soft cores, and this in turn corresponds to $N \simeq 100$ in the core region as described in § 3.1.5.

We may attribute this discrepancy to the fact that Davé et al. (2001) did not actually perform rotation curve fitting with their N-body results. Davé et al. (2001) instead found their preferred value of σ by constraining the halo density at $r = 1\text{kpc}$ for halos at the present epoch to be in the range $[0.01 - 0.1]M_{\odot}\text{pc}^{-3}$. However, limited numerical resolution prevented them from determining the halo density at radii as small as those required to match the observed rotation curves which show flat-density cores. Our results suggest that, had their simulations been capable of resolving the profile at smaller radii, they would have found that the density continued to rise to a higher value at smaller radii. As seen in Figure 1 of Davé et al. (2001), three halos with $M \simeq 10^9 M_{\odot}$ ($M = (1.7, 0.9, 1.1)10^9 M_{\odot}$) are almost unaffected by the inclusion of SIDM collisionality if $\sigma \simeq [0.56 - 5.6]\text{cm}^2\text{g}^{-1}$, which implies that the NFW-type cuspy profile persists in these halos despite the SIDM interaction.

Conclusions drawn from current N-body simulations of SIDM halo profiles may, therefore, require revision in light of our results. The scattering

cross-section $\sigma \simeq 218.5 \text{ cm}^2 \text{ g}^{-1}$ is in an interesting regime which has not been studied before by N-body simulations. This value may also help to resolve the problem identified by the N-body simulations for smaller cross section, in which larger-mass halos result in relatively larger cores. The small cross section regime corresponds to $Q < Q_{\text{th}}$, for which the effect of SIDM conduction increases with increasing Q . As shown in Figure 3.5, larger-mass halos typically have larger Q -values, since their larger sizes more than offset the lower mean densities which result from their later formation. According to our results, however, halos from dwarf galaxies to clusters are not in the small cross section regime (i.e. low- Q regime). In fact, the dwarf galaxy rotation curves prefer $Q = Q_{\text{th}}$, so large mass galaxies and clusters have $Q > Q_{\text{th}}$, in general (see Fig. [3.5]). According to Figure 3.2, this high- Q regime suppresses conduction, yielding smaller cores (i.e. higher central densities) for higher-mass halos. We predict, therefore, that as long as $\sigma \simeq 218.5 \text{ cm}^2 \text{ g}^{-1}$ is used in an SIDM N-body simulation, a constant value, independent of velocity, will suffice to match both dwarf galaxy rotation curves and the mass profiles of larger-mass halos.

3.1.8 Conclusion/Discussion

CDM particles have been assumed to be collisionless in the standard CDM theory of cosmic structure formation. Despite the success of this standard theory, the elementary particle physics theory necessary to explain the origin and microscopic properties of the particles which comprise this dark

matter is not yet known. It is natural for us to ask if the microscopic nature of CDM particles might lead to further constraints on this theory by astronomical observation. We have focused here on one such microscopic property, that of self-interaction by elastic scattering, and its effect on the internal structure and dynamical evolution of virialized CDM halos during galaxy and large-scale structure formation. The apparent discrepancy between the observed density profiles of the halos of dark-matter dominated dwarf and LSBs and those predicted by N-body simulations of collisionless CDM may well be resolved if one assumes that CDM particles interact with each other non-gravitationally. The self-interacting dark matter (SIDM) hypothesis is an attempt to produce such a nongravitational interaction between dark matter particles.

We have derived the first fully-cosmological similarity solutions for halo formation in the presence of collisionality. This provides an analytical theory of the effect of the self-interacting dark matter (SIDM) hypothesis on CDM halo density profiles as follows:

- We have adopted the spherical infall model of cosmological halo formation, guided by the results of N-body simulations of CDM. The collisional Boltzmann equation for the evolution of the gas of CDM particles yields a set of fluid-like conservation equations under the assumptions of spherical symmetry and isotropic velocity distribution. The effect of self-interaction collisions is accounted for by an effective conductivity term in the energy equation. This conductivity is valid for arbitrarily large or small collision mean free path λ_{mfp} .

- For an Einstein-de Sitter universe (or a flat universe with cosmological constant, at early times when matter dominates), the nonlinear growth of perturbations which leads to halo formation in the spherical infall model can be described by similarity solutions in the absence of conductivity. In the presence of SIDM conductivity, self-similarity is still possible, but only for mass perturbations $\delta M/M \propto M^{-1/6}$. Remarkably, this self-similarity required in our solution is well-motivated and justified by the theory of halo formation from peaks of the Gaussian random noise density fluctuations (Hoffman & Shaham 1985). For galactic halos, which form from density fluctuations whose power spectrum can be approximated by a power law $P(k) \propto k^{-2.5}$, the conditions required for this particular self-similarity naturally arise.
- According to our similarity solutions, collisions of SIDM transport heat from the hotter, outer halo region into the colder core region. This process flattens the central density, and continuous infall pumps energy into the halo which stabilizes the core against gravothermal catastrophe.
- These solutions are characterized by a single dimensionless quantity, the collisionality parameter $Q \equiv \sigma \rho_b r_{\text{vir}} \propto r_{\text{vir}}/\lambda_{\text{mfp}}$, where σ is the scattering cross section per unit mass, ρ_b is the mean matter density, r_{vir} is halo virial radius and λ_{mfp} is the collision mean free path. The maximum flattening of central density occurs for an intermediate value of Q , $Q_{\text{th}} = 7.35 \times 10^{-4}$, at which the halo is maximally relaxed to isothermality.

The density profile of the Q_{th} solution matches that inferred from the observed rotation curves of dwarfs and low surface brightness galaxies (LSB) very well.

- In the low- Q regime ($Q < Q_{\text{th}}$), flattening of the central density profile becomes *stronger* as Q increases. Previous cosmological SIDM N-body simulations with $\sigma \simeq [0.1 - 10]\text{cm}^2\text{g}^{-1}$ lie in this regime (Yoshida et al. 2000b, Davé et al. 2001, Colín et al. 2002). Central density profiles became flatter as they increased the scattering cross-section, which is equivalent to increase in Q , because $Q \propto \sigma$. On the contrary, in the high- Q regime ($Q > Q_{\text{th}}$), flattening of the central density becomes *weaker* as Q increases. This happens because the scattering mean free path becomes shorter as Q increases. SIDM simulations which adopt a fully collisional limit to derive the maximal density flattening, which corresponds to ordinary gas dynamics (Yoshida et al. 2000a; Moore et al. 2000), report that halos obtain density profiles with central cusps as steep as or steeper than those in collisionless N-body simulations. This seemingly puzzling behavior is easily explained: $\sigma \rightarrow \infty$ corresponds to $Q \rightarrow \infty$, and therefore density flattening becomes negligible.
- Under the assumption that dwarfs and LSBs formed at their typical collapse epoch in ΛCDM , $\sigma \simeq 200\text{cm}^2\text{g}^{-1}$ makes $Q = Q_{\text{th}}$, much higher than previous estimates, $\sigma \simeq [0.5 - 5]\text{cm}^2\text{g}^{-1}$, based on N-body experiments. This value of σ , independent of halo mass, would make $Q > Q_{\text{th}}$ for

clusters, which typically formed only recently, resulting in relatively less flattening of their central density profile and a smaller core. A velocity dependent cross-section, $\sigma \propto 1/v$, suggested by Yoshida et al. (2000b) is thus unnecessary.

- According to our similarity solutions, the solution for $Q = Q_{\text{th}}$ represents the solution most relaxed to isothermality inside the virialized postshock region. It is notable, therefore, that the $Q = Q_{\text{th}}$ solution is very similar to the nonsingular TIS solution of Shapiro et al. (1999) for the post-collapse equilibrium structure of virialized halos. The latter yields a mass profile almost indistinguishable from the mass profile of the Burkert fit to the rotation curves of dwarf and LSB galaxies (Iliev & Shapiro 2001), as is the $Q = Q_{\text{th}}$ SIDM profile we have derived here. This suggests that the TIS halo model, which assumes that halos are isothermal, is a natural outcome of the dynamical formation of CDM halos when conductivity causes the halo to relax maximally toward isothermality.

One may improve upon this work by performing a cosmological N-body simulation. As our analysis is based upon self-similarity, or a constant mass accretion rate $\frac{\partial \log M}{\partial \log a} = 6$, when the mass accretion rate deviates from this canonical rate, our analysis is no longer valid. Several authors have investigated a realistic halo formation history both by an analytic approach and by N-body experiments, tracking the history of the “most massive progenitor (MMP)”. Wechsler et al. (2002) performed a cosmological N-body simulation

and tracked the growth of MMP mass in a Λ CDM universe. Nusser & Sheth (1999) calculated the growth of MMP for a power-law power spectrum and van den Bosch (2002) calculated it for a CDM power spectrum, both using the extended Press-Schechter theory. These studies show that mass accretion starts with a fast, rapid merger and ends with smooth, continuous accretion. This trend is clearly seen in equation (2.32), where the logarithmic accretion rate is decreasing linearly with increasing scale factor a . The accretion rate obtained in this way is different from what is expected from HS. For $n = -2.5$ in the matter-dominated era, we find from equation (3.10) that $\frac{\partial \log M}{\partial \log t} = 4$ or $\frac{\partial \log M}{\partial \log a} = 6$. This fast accretion rate captures only the early mass accretion epoch given by equation (2.32), and therefore, one should not apply this rate to the later epoch when mass accretion becomes negligible. This is the moment where the evolution of SIDM halos deviates from the self-similarity we assumed.

For cluster-mass halos, there is another reason that our assumption of self-similarity breaks down and should be improved in future work; the value of n which enters the self-similar infall model in Λ CDM actually depends weakly upon halo mass. The value we have adopted to ensure self-similarity in the presence of SIDM collisionality, $n = -2.5$, is appropriate for the entire range of galactic halo masses. As Figure 2.4 shows, however, n increases with mass, and for clusters with mass above $10^{14} M_{\odot}$, $n > -2$. If $n \neq -2.5$, self-similarity is violated by the presence of SIDM terms in the equations. Since the accretion rate is lower if n is higher (i.e. $\frac{\partial \log M}{\partial \log a} = \frac{3}{n+3}$), the flattening effect of SIDM on

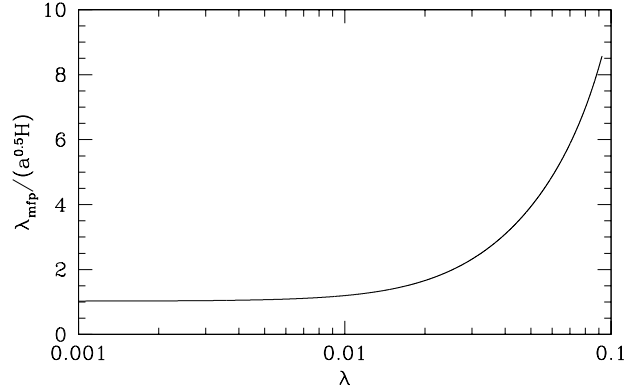


Figure 3.7: Comparison of length scales for the $Q = Q_{\text{th}}$ case. The mean free path λ_{mfp} is comparable to the gravitational scale height H in the core region. However, the ratio of the mean free path to the gravitational scale height becomes larger as the radius increases. See also Figure 3.3, which includes other values of Q .

the halo central density profile may be lower on cluster scales than expected from our self-similar solutions for $n = -2.5$.

Does our prediction of high value of σ , $\sigma \simeq 200\text{cm}^2\text{g}^{-1}$, affect the abundance of dark matter substructure? Gravitational lensing flux anomalies have been interpreted as evidence for the existence of dark matter substructures in the parent halo (Metcalf & Zhao 2002; Dalal & Kochanek 2002; Keeton et al. 2003; Mao et al. 2004). The self-interacting dark matter, if real, would suppress the number of dark matter substructures to some extent. We are not sure at this stage, however, how strong this effect will be: the simple assumption of cold, continuous mass infall prevents us from making any strong prediction. We instead describe, in the following discussion, the complexity

relating to two main mechanisms for suppressing the substructure formation when dark matter is collisional: ram-pressure stripping and thermal evaporation. One should also note that the interpretation of the lensing flux anomalies is not settled yet. Recent analysis indicates that this anomaly may not require any substructure in the primary lens halo, but only the substructure in the intergalactic space (Metcalf 2005).

We now point out some caveats found in previous analyses, which also require more realistic, cosmological analysis. As many previous analytical estimates have been based on either isolated halos or very simplified models, we believe that fully cosmological N-body simulations in the high- Q (σ) regime should be carried out to clarify this issue. For instance, the restriction coming from the susceptibility of SIDM halos to ram-pressure stripping (Furlanetto & Loeb 2002a; Natarajan et al. 2002) may be relaxed if we remove the simplicity in their analysis. They determine the truncation radius of a galaxy in a cluster by the condition

$$\rho_c(r)v_g^2 = \rho_g(r_t)\sigma_g^2, \quad (3.47)$$

where v_g is the velocity of the galaxy inside a cluster, $\rho_c(r)$ is the density of the cluster at radius r , $\rho_g(r_t)$ is the density of the galaxy at its truncation radius r_t , and σ_g is the internal velocity dispersion of the galaxy. Equation (3.47) is valid for highly collisional fluid. They then use the restriction that

$$\frac{\lambda_{\text{mfp}}}{r_t} \simeq \frac{1}{\sigma\Sigma(r_t)} \leq 1 \quad (3.48)$$

where λ_{mfp} is the collision mean free path and $\Sigma(r_t)$, which is 0.024 g cm^{-2} for

their fiducial case, is the surface density of a galaxy at r_t . However, this is a crude way of describing the fluid regime where the equation (3.47) can be applied. There exists a regime where the SIDM can be treated as collisional only at the center because the ratio of the mean free path to the gravitational scale height becomes larger as the radius of a galaxy increases (see Fig. [3.7]; when we express these length scales with dimensionless terms used for our similarity solutions, the scattering mean free path is $L_{\text{mfp}} \equiv \frac{1}{DQ}$, and the gravitational scale height is $H \equiv \frac{\sqrt{3P/2}}{D}$). In such cases, a “global” application of equation (3.47) is not valid. Ram-pressure stripping in this case would not be as severe as in the case of purely collisional fluid, because cluster SIDM particles have a high probability of penetrating an SIDM galactic halo deeply without experiencing collision at $r \gtrsim r_t$. Therefore, to apply equation (3.47), we have to be more conservative in defining the fluid regime, which will relax the constraint $\sigma \lesssim 42\text{cm}^2\text{g}^{-1}$ (Natarajan et al. 2002) set by equation (3.48).

Gnedin & Ostriker (2001) constrained σ from their numerical and semi-analytical calculation of the evaporation time of elliptical galaxies embedded in a cluster environment. According to their analysis, such galactic halos can evaporate within the age of the universe if $\sigma = [0.3 - 10^4]\text{cm}^2\text{g}^{-1}$. However, their analysis is based on a fixed cluster environment. Suppose a cosmological variant of this problem: for instance, an elliptical galaxy may form by a recent merger at $z = 1$ when the temperature of the cluster, which only forms at $z \simeq 0$, is very low. When the evaporation time is about the age of the universe ($\sim 10^{10}\text{yr}$), the elliptical galaxy has a fair chance to survive because

the evaporation time is greater than the time from its formation epoch to the present. The excluded range of σ would then change substantially by shifting the marginal values, $\sigma \simeq 0.3 \text{ cm}^2 \text{ g}^{-1}$ or $\sigma \simeq 10^4 \text{ cm}^2 \text{ g}^{-1}$, which correspond to the evaporation time of the order of the age of the universe. Moreover, their analysis is only valid for either the very long mean free path limit or the very short mean free path limit. They exclude the intermediate regime at $\sigma \simeq 200 \text{ cm}^2 \text{ g}^{-1}$ simply by an extrapolation of these two regimes.

Because of these problems, we assert that a more refined, fully cosmological analysis and new cosmological N-body simulations with a wider range of σ values, including $\sigma \simeq [100 - 500] \text{ cm}^2 \text{ g}^{-1}$, should be performed. Even though our analysis here is fully cosmological, it is restricted by the fact that it is based on a constant logarithmic mass accretion rate (i.e. $\frac{\partial \log M}{\partial \log a} = \frac{1}{\varepsilon} = \frac{3}{n+3} = 6$ for $n = -2.5$) that provides self-similarity. However, a more realistic mass accretion history constructed from merger trees in N-body simulations shows a gradual decrease of the logarithmic mass accretion rate over time, as seen in equation (2.32) (e.g. Wechsler et al. 2002). When the mass accretion rate becomes very small at late times, the underlying halo properties will deviate significantly from self-similarity. Moreover, the relatively high scattering cross-section which we find provides the best-fitting to dwarf galaxy rotation curves – $\sigma \simeq 200 \text{ cm}^2 \text{ g}^{-1}$ – has never been tested in cosmological SIDM N-body simulations. Further study of this regime is warranted.

3.2 511keV Dark Matter and the γ -ray background

3.2.1 Missing Gamma Ray Background Problem

What is the origin of the cosmic γ -ray background? It is usually understood that the cosmic γ -ray background is a superposition of unresolved astronomical γ -ray sources distributed in the universe. Active Galactic Nuclei (AGNs) alone explain most of the background light in two energy regions: ordinary (but obscured by intervening hydrogen gas) AGNs account for the low-energy ($\lesssim 0.5$ MeV) spectrum (Comastri et al. 1995; Zdziarski et al. 1995; Ueda et al. 2003), whereas beamed AGNs (known as Blazars) account for the high-energy ($\gtrsim 20$ MeV) spectrum (Salamon & Stecker 1994; Stecker & Salamon 1996; Pavlidou & Fields 2002). There is, however, a gap between these two regions. While historically supernovae have been a leading candidate for the background up to 4 MeV (Clayton & Ward 1975; The, Leising, & Clayton 1993; Zdziarski 1996; Watanabe et al. 1999), recent studies (Strigari et al. 2005; Ahn, Komatsu, & Höflich 2005) show that the supernova contribution is an order of magnitude lower than observed. The spectrum at 4–20 MeV also remains unexplained (for a review on this subject, see Stecker & Salamon 2001). It is not very easy to explain such high-energy background light by astronomical sources without AGNs or supernovae.

3.2.2 Dark Matter Annihilation Signal?: Galactic Radiation

So, what is the origin of the cosmic γ -ray background at 0.5–20 MeV? On energetics, a decay or annihilation of particles having mass in the range

of $0.5 \text{ MeV} \lesssim m_X \lesssim 20 \text{ MeV}$ would produce the background light in the desired energy band. Since both lower- and higher-energy spectra are already accounted for by AGNs almost entirely, too lighter or too heavier (e.g., neutralinos) particles should be excluded. Is there any evidence or reason that such particles should exist? The most compelling evidence comes from 511 keV line emission from the central part of our Galaxy, which has been detected and mapped by the SPI spectrometer on the INTERnational Gamma-Ray Astrophysics Laboratory (INTEGRAL) satellite (Jean et al. 2003; Knödlseeder et al. 2003). This line should be produced by annihilation of electron-positron pairs, and one of the possible origins is the dark matter particles annihilating into electron-positron pairs (Boehm et al. 2004b). This proposal explains the measured injection rate of positrons as well as morphology of the signal extended over the bulge region. Intriguingly, popular astronomical sources such as supernovae again seem to fail to satisfy the observational constraints (Hooper et al. 2004). Motivated by this idea, in Ahn & Komatsu (2005), we have calculated the γ -ray background of redshifted 511 keV lines from extragalactic halos distributed over a large redshift range. We have shown that the annihilation signal makes a substantial contribution to the low-energy spectrum at $< 0.511 \text{ MeV}$, which constrains m_X to be heavier than 20 MeV in order for the sum of the AGN and annihilation contributions not to exceed the observed signal.

3.2.3 Background from Continuum Annihilation Signal

In this work, we extend our previous analysis (Ahn & Komatsu 2005) to include continuum emission accompanying annihilation. The emerging continuum spectrum should of course depend on the precise nature of dark matter particles, which is yet to be determined. Recently, an interesting proposal was made by Beacom, Bell, & Bertone (2005): radiative corrections to annihilation, $XX \rightarrow e^+e^-$, should lead to emission of γ -rays via the internal bremsstrahlung, the emission of extra final-state photons during a reaction, $XX \rightarrow e^+e^-\gamma$. They have calculated the spectrum of the internal bremsstrahlung expected for annihilation in the Galactic center, compared to the Galactic γ -ray data, and obtained a constraint on mass as $m_X \lesssim 20$ MeV. A crucial assumption in their analysis is that the cross section of internal bremsstrahlung is linearly proportional to the annihilation cross section, and the constant of proportionality is independent of the nature of annihilation, as is found for related processes (Crittenden et al. 1961; Martyn 1990; Berends & Bohm 1998; Bergström et al. 2005). More specifically, they assumed that the cross section of $XX \rightarrow e^+e^-\gamma$ would be calculated by that of $e^+e^- \rightarrow \mu^+\mu^-\gamma$ with the muon mass replaced by the electron mass. Although the equivalence between these two processes/cross-sections has not been demonstrated as yet, we adopt their procedure into our calculations.

We calculate the background intensity, I_ν , by

$$I_\nu = \frac{c}{4\pi} \int \frac{dz P_\nu([1+z]\nu, z)}{H(z)(1+z)^4}, \quad (3.49)$$

where ν is an observed frequency, $H(z)$ is the expansion rate at redshift z , and $P_\nu(\nu, z)$ is the volume emissivity (in units of energy per unit time, unit frequency and unit proper volume):

$$P_\nu = \frac{1}{2} h\nu \langle \sigma v \rangle n_X^2 \left[\frac{4\alpha g(\nu)}{\pi \nu} \right], \quad (3.50)$$

where $\alpha \simeq 1/137$ is the fine structure constant, n_X is the number density of dark matter particles, and $\langle \sigma v \rangle$ is the thermally averaged annihilation cross section. To fully account for WMAP's determination of mass density of dark matter (Spergel et al. 2003), $\Omega_X h^2 = 0.113$, by cold relics from the early universe, one finds $\langle \sigma v \rangle = [3.9, 2.7, 3.2] 10^{-26} \text{ cm}^3 \text{ s}^{-1}$ for $m_X = [1, 10, 100] \text{ MeV}$, respectively (e.g., see Eq. [1] in Boehm, Enßlin, & Silk 2004a). We have assumed that $\langle \sigma v \rangle$ is velocity-independent (S-wave annihilation). One might add a velocity-dependent term (such as P-wave annihilation) to the cross-section; however, such terms add more degrees of freedom to the model, making the model less predictable. While Boehm et al. (2004b) argue that the S-wave cross section overpredicts the γ -ray flux from the Galactic center, we have shown in Ahn & Komatsu (2005) that it is still consistent with the data for $m_X \gtrsim 20 \text{ MeV}$ and the Galactic density profile of $\rho \propto r^{-0.4}$ or shallower. (We shall discuss an issue regarding the density profile later.) Finally, a dimensionless spectral function, $g(\nu)$, is defined by

$$g(\nu) \equiv \frac{1}{4} \left(\ln \frac{s'}{m_e^2} - 1 \right) \left[1 + \left(\frac{s'}{4m_X^2} \right)^2 \right], \quad (3.51)$$

where $s' \equiv 4m_X(m_X - h\nu)$. This function is approximately constant for $h\nu <$

m_X , and then sharply cuts off at $h\nu \sim m_X$. Thus, one may approximate it as

$$g(\nu) \approx \ln \left(\frac{2m_X}{m_e} \right) \vartheta(m_X - h\nu) \quad (3.52)$$

for the sake of an order-of-magnitude estimation. (Note that we have also assumed $m_X \gg m_e$.)

Since the number density is usually unknown, we use the mass density, $\rho_X \equiv n_X/m_X$, instead. After multiplying by ν , one obtains

$$\begin{aligned} \nu I_\nu &= \frac{\alpha h\nu \langle \sigma v \rangle}{2\pi^2 m_X^2} \int_0^\infty \frac{dz \, cg[(1+z)\nu]}{H(z)} \langle \rho_X^2 \rangle_z \\ &\simeq 3.800 \text{ keV cm}^{-2} \text{ s}^{-1} \text{ str}^{-1} \\ &\quad \times \left(\frac{\langle \sigma v \rangle}{10^{-26} \text{ cm}^3 \text{ s}^{-1}} \right) \left(\frac{h\nu \text{ 1 MeV}}{m_X^2} \right) \\ &\quad \times \int dz \frac{g[(1+z)\nu](1+z)^2(\Omega_X h^2)^2 C_X(z)}{\sqrt{\Omega_m h^2(1+z)^3 + \Omega_\Lambda h^2}} \frac{1}{10^3}, \end{aligned} \quad (3.53)$$

where $\langle \rho_X^2 \rangle_z$ is the average of ρ_X^2 over proper volume at z , and $C_X(z) \equiv \langle \rho_X \rangle_z^2 / \langle \rho_X^2 \rangle_z$ is the dark matter clumping factor. (We have used $\langle \rho_X \rangle_z = 10.54 \Omega_X h^2 (1+z)^3 \text{ keV cm}^{-3}$.) While equation (3.53) is exact, one may obtain a better analytical insight of this equation by using the approximation to $g(\nu)$ (Eq. [3.52]),

$$\begin{aligned} \nu I_\nu &\simeq 3.800 \text{ keV cm}^{-2} \text{ s}^{-1} \text{ str}^{-1} \\ &\quad \times \ln \left(\frac{2m_X}{0.511 \text{ MeV}} \right) \left[\frac{(\Omega_X h^2)^2}{\sqrt{\Omega_m h^2}} \right] \left(\frac{\langle \sigma v \rangle}{10^{-26} \text{ cm}^3 \text{ s}^{-1}} \right) \\ &\quad \times \sqrt{\frac{1 \text{ MeV}^2}{h\nu m_X}} \int_{h\nu/m_X}^1 dy \, y^{1/2} \frac{C_X[(m_X/h\nu)y]}{10^3}, \end{aligned} \quad (3.54)$$

where $y \equiv h\nu(1+z)/m_X$. Here, we have also assumed that the integral is dominated by $1+z \gg (\Omega_\Lambda/\Omega_m) = 2.3$.

We follow the method developed in Ahn & Komatsu (2005) for calculating the clumping factor of dark matter, $C_X(z)$. We have shown that $C_X(z)$ at $z \lesssim 20$ is approximately a power law,

$$C_X(z) = C_X(0)(1+z)^{-\beta}, \quad (3.55)$$

and β depends on adopted dark matter halo profiles. For example, a cuspy profile such as the Navarro-Frenk-White (NFW) profile (Navarro et al. 1997), $\rho_X(r) \propto r^{-1}$, gives $C_X(0) \simeq 10^5$ and $\beta \simeq 1.8$, while a flat profile such as the Truncated Isothermal Sphere (TIS: Shapiro et al. 1999; Iliev & Shapiro 2001), $\rho_X(r) \propto r^0$, gives $C_X(0) \simeq 10^3$ and $\beta \simeq 0$ (see Figure 2 of Ahn & Komatsu 2005). Using a power-law evolution of $C_X(z)$, one obtains an approximate shape of the spectrum as

$$\nu I_\nu \propto \frac{h\nu \ln(2m_X/m_e)}{(\beta - 3/2)m_X^2} \left[1 - \left(\frac{h\nu}{m_X} \right)^{\beta-3/2} \right] \vartheta(m_X - h\nu), \quad (3.56)$$

for $m_X \gg m_e$. If $\beta < 3/2$ (e.g., TIS), $\nu I_\nu \propto (h\nu)^{\beta-1/2} (\ln m_X) / m_X^{\beta+1/2} \vartheta(m_X - h\nu)$, whereas if $\beta > 3/2$ (e.g., NFW), $\nu I_\nu \propto h\nu [\ln(2m_X/m_e)] / m_X^2 \vartheta(m_X - h\nu)$. Note that the shape of the spectrum becomes insensitive to halo profiles for the latter case (while the amplitude still depends on profiles).

Henceforth we shall adopt the NFW profile as the fiducial model, as it fits the mean central halo profiles in numerical simulations well. Following the previous paper, we take into account a scatter in halo profiles by integrating over a probability distribution of halo concentration; thus, our model effectively incorporates significantly less concentrated (such as our Galaxy) or

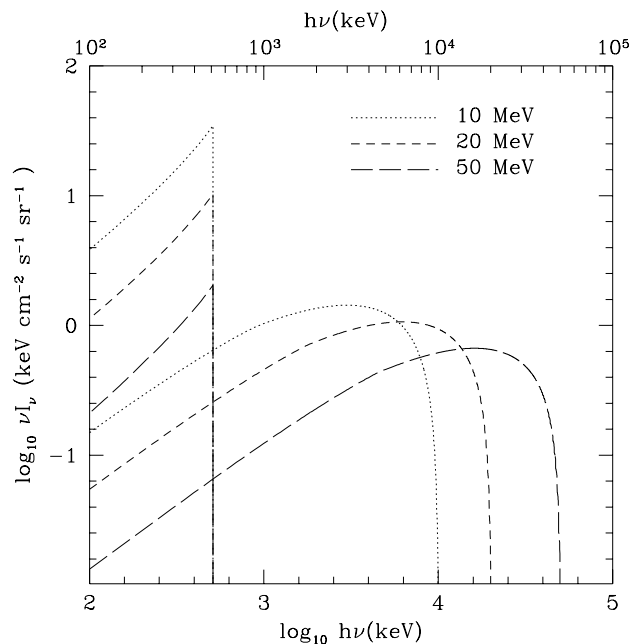


Figure 3.8: Cosmic γ -ray background from dark matter annihilation. The dotted, short-dashed, and long-dashed lines show $m_X = 10, 20,$ and 50 MeV, respectively. The curves which sharply cut off at 511 keV represent background light from line emission (Ahn & Komatsu 2005), while the others which extend to higher energy represent the internal bremsstrahlung.

more concentrated profiles than the average NFW. One might argue that our model based on the NFW profile is unable to explain γ -ray emission from the Galactic center, which requires $\rho \propto r^{-0.4}$ (or shallower). If desired, one might use this profile and recalculate the γ -ray background spectrum; however, we continue to use the NFW profile, assuming that our Galaxy is not a “typical” halo in the universe. If there are so many more galaxies which obey the NFW profile, then the signal should be dominated by those typical halos. Of course, real universe does not have to be the same as numerical simulations,

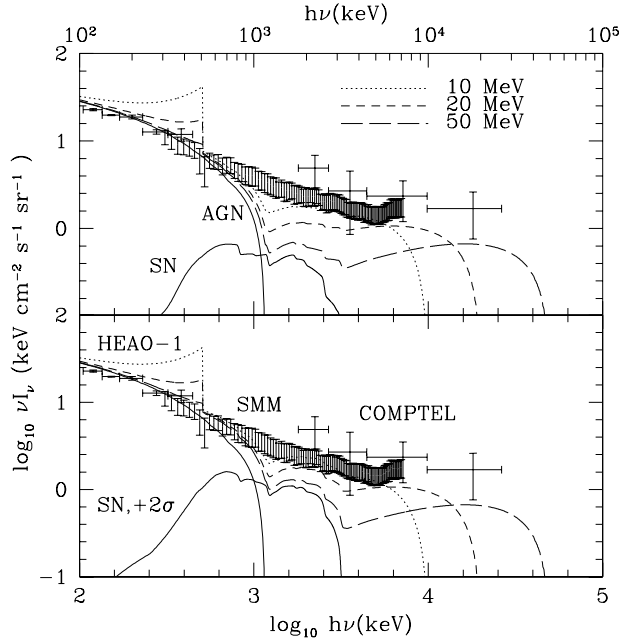


Figure 3.9: The total cosmic γ -ray background produced by dark matter annihilation, AGNs (Ueda et al. 2003), and Type Ia supernovae (Ahn et al. 2005). The dotted, short-dashed, and long-dashed lines show $m_X = 10, 20,$ and 50 MeV, respectively. The supernova contribution depends on the observed supernova rate, and we consider the best-fit rate (upper panel) as well as the 2σ upper limit (lower panel). The data points of HEAO-1 A4 MED (Gruber et al. 1999), SMM (Watanabe et al. 1999), and COMPTEL (Kappadath et al. 1996) experiments are also shown.

and one way to incorporate the uncertainty of halo profiles into our analysis would be to treat $C_X(0)$ and β as free parameters. We shall come back to this point at the end of this work. Figure 3.8 shows the predicted cosmic γ -ray background from dark matter annihilation, including line (Ahn & Komatsu 2005) and continuum emission, for $m_X = 10, 20,$ and 50 MeV. The shape of the internal bremsstrahlung is described well by the approximate formula

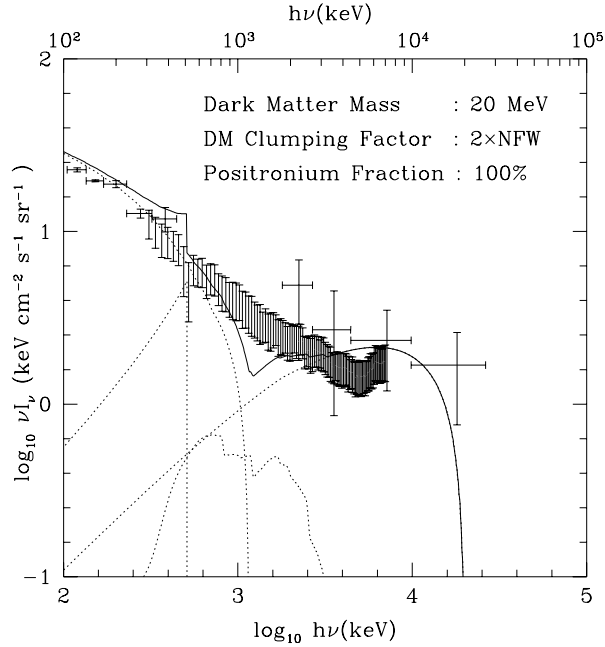


Figure 3.10: The best-fit model of the cosmic γ -ray background. The model assumes (a) $m_X = 20$ MeV, (b) the mean dark matter clumping factor is twice as large as predicted by the NFW profile (due to either a steeper profile or the presence of substructures), and (c) line emission is solely produced via positronium formation. The dashed lines show each contribution separately.

(Eq. [3.56]) with $\beta = 1.8$. As expected, the continuum spectrum extends up to $h\nu \sim m_X$, whereas line emission contributes only at < 0.511 MeV.

Now let us add extra contributions from known astronomical sources and compare the total predicted spectrum with the observational data. Figure 3.9 compares the sum of dark matter annihilation, AGNs (Ueda et al. 2003) and Type Ia supernovae (Ahn et al. 2005) with the data points of HEAO-1 (Gruber et al. 1999), SMM (Watanabe et al. 1999), and COMPTEL (Kappa-

dath et al. 1996) experiments. We find that $m_X \sim 20$ MeV fits the low-energy spectrum (Ahn & Komatsu 2005) and explains about a half of the spectrum at 1–20 MeV. Therefore, the internal bremsstrahlung from dark matter annihilation is a very attractive source of the cosmic γ -ray background in this energy region. It is remarkable that such a simple model provides adequate explanations to two completely different problems: 511 keV line emission from the Galactic center (Boehm et al. 2004b), and missing γ -ray light at 1–20 MeV. (The regular Blazars would dominate the spectrum beyond 20 MeV (Salamon & Stecker 1994; Stecker & Salamon 1996; Pavlidou & Fields 2002).

If desired, one might try to improve agreement with the data in the following way. The continuum (combined with the other contributions) can fully account for the SMM and COMPTEL data, if the clumping factor is twice as large as predicted by the NFW profile. This could be easily done within uncertainty in our understanding of the structure of dark matter halos: for example, a slightly steeper profile, or the presence of substructure (Taylor & Silk 2003). However, a larger clumping factor also increases 511 keV line emission by the same amount, which would exceed the HEAO-1 and SMM data. How do we reduce line emission independent of continuum? The line emission is suppressed by up to a factor of 4, if e^+e^- annihilation occurs predominantly via positronium formation. Once formed, a positronium decays into either two 511 keV photons or three continuum photons. As the branching ratio of the former process is only 1/4, line emission is suppressed by a factor of 4 if all of annihilation occurs via positronium formation. If a fraction, f ,

of annihilation occurs via positronium, then line is suppressed by $1 - 3f/4$ (Beacom et al. 2005); thus, we can cancel the effect of doubling the clumping by requiring that 2/3 of line emission be produced via positronium. Figure 3.10 shows our “best-fit” model, which assumes (a) $m_X = 20$ MeV, (b) the mean clumping factor is twice as large, and (c) line emission is solely produced via positronium ($f = 1$). Note that this is a reasonable extension of the minimal model and makes the model more realistic: we know from simulations that there must exist substructures in halos. Some fraction of line emission must be produced via positronium, as it has been known that more than 90% of 511 keV emission from the Galactic center is actually produced via positronium formation (Kinzer et al. 2001; Churazov et al. 2005). While the model seems to slightly exceed the HEAO-1 and SMM data at low energy, we do not take it seriously as the discrepancy would be smaller than the uncertainty of the AGN model. The AGN model presented here assumes a high-energy cut-off energy of $E_{\text{cut}} = 0.5$ MeV (Ueda et al. 2003). Since current data of AGNs in such a high energy band are fairly limited, uncertainty in E_{cut} is more than a factor of 2. Even a slight reduction in E_{cut} would make our model fit the low-energy spectrum.

The best-fit model is consistent with and supported by all of the current observational constraints: it fits the Galactic γ -ray emission as well as the cosmic γ -ray emission. It might also account for a small difference between theory and the experimental data of the muon and electron anomalous magnetic moment (Boehm & Ascasibar 2004). We stress here that, to the best of

our knowledge, all of these data would remain unexplained otherwise. There is, however, one potential conflict with a new analysis of the SPI data by Ascasibar et al. (2005), which shows that a NFW density profile does provide a good fit to 511 keV line emission from the Galactic center, as opposed to the previous analysis by Boehm et al. (2004b), which indicated a shallower profile than NFW. This new model would have much higher dark-matter clumping and require a substantially (more than an order of magnitude) smaller annihilation cross-section than $\langle\sigma v\rangle \sim 3 \times 10^{-26} \text{ cm}^3 \text{ s}^{-1}$ to fit the Galactic data. Is our Galaxy consistent with NFW? This is a rather complicated issue which is still far from settled (e.g., Binney & Evans 2001; Klypin, Zhao, & Somerville 2002), and more studies are required to understand the precise shape of density profile of our Galaxy. If our Galaxy is described by a steep profile such as NFW, then the dark matter annihilation probably makes a negligible contribution to the γ -ray background, unless dark matter clumping is significantly increased by substructure (Taylor & Silk 2003), compensating a small cross section. On the other hand, if it were confirmed that our Galaxy has a shallow density profile and the contribution of the dark matter annihilation to the γ -ray background is negligible, it would be difficult to explain the Galactic γ -ray signal solely by annihilation of light dark matter particles.

As shown in Figure 3.10, dark matter annihilation produces a distinctive γ -ray spectrum at 0.1–20 MeV. More precise determinations of the cosmic γ -ray background in this energy band will undoubtedly test our proposal. If confirmed, such measurements would shed light on the nature of dark matter,

and potentially open a window to new physics: one implication is that neutralinos would be excluded from a candidate list of dark matter. Phenomenologically, our model may be parameterized by four free parameters: (1) dark matter mass, m_X , (2) a dark matter clumping factor at present, $C_X(0)$, (3) redshift evolution of clumping, β , and (4) a positronium fraction, f . When more precise data are available in the future, it might be possible to perform a full likelihood analysis and constrain properties of dark matter particles as well as dark matter halos.

Finally, the angular power spectrum of anisotropy of the γ -ray background at 1–20 MeV would also offer a powerful diagnosis of the detected signal (see Zhang & Beacom 2004 for the contribution from Type Ia supernovae). Our model predicts that the angular power spectrum should be given by the trispectrum (the Fourier transform of the four-point correlation function) of dark matter halos projected on the sky, as the signal is proportional to ρ^2 . More specifically, the power spectrum should follow precisely that of the dark matter clumping factor. More high-quality data of the cosmic γ -ray background in this energy band are seriously awaited.

Chapter 4

21cm Background from the Cosmic Dark Ages

4.1 Introduction

One of the most promising means by which to observe the high redshift universe in the cosmic “dark ages” is through the 21 cm wavelength hyperfine transition of the neutral hydrogen that is abundant prior to reionization (e.g. Scott & Rees, 1990; Subramanian & Padmanabhan, 1993). Motivated by the prospect of new radio telescopes that will be able to observe such a signal, several specific observational techniques have been proposed. Among these are the angular fluctuations on the sky (e.g. Madau, Meiksin, & Rees 1997; Tozzi et al. 2000; Iliev et al. 2002 – ISFM hereafter; Ciardi & Madau 2003; Iliev et al. 2003; Zaldarriaga, Furlanetto, & Hernquist 2004; Furlanetto, Sokasian, & Hernquist 2004), features in the frequency spectrum of the signal averaged over a substantial patch of the sky (Shaver et al., 1999; Gnedin & Shaver, 2004) and studies of absorption features in the spectra of bright, high-redshift radio sources (Carilli, Gnedin, & Owen 2002; Furlanetto & Loeb 2002b).

Most of these techniques, except for absorption against bright radio sources, depend on the local spin temperature of the gas, T_S , being different from the temperature of the CMB, T_{CMB} . Otherwise, the intensity of the

radiation at the redshifted 21 cm wavelength will be coupled to, and thus indistinguishable from, the CMB at these wavelengths. There are two main physical mechanisms by which the spin temperature is decoupled from the CMB temperature; Ly α pumping by radiation with a wavelength in the Ly α transition (the so-called “Wouthuysen-Field effect” : Wouthuysen 1952; Field 1959), and spin exchange during collisions between neutral hydrogen atoms (Purcell & Field, 1956). The efficiency of Ly α pumping depends upon the intensity of the UV radiation field at the Ly α transition, whereas the efficiency of collisional coupling depends upon the local gas density and temperature.

At very high redshifts ($z > 30$), gas at the mean density is sufficiently dense for collisions to couple the spin temperature to the kinetic gas temperature. At lower redshifts, collisions become negligible for gas at or below the cosmic mean density, and it becomes invisible until its spin temperature is again decoupled from the CMB by Ly α pumping due to an early UV background from the first stars and quasars. Even though the collisional decoupling from the CMB is ineffective for $z < 30$ and gas at the mean density, gas in overdense and/or heated regions can still be collisionally-decoupled. In particular, the gas density within “minihalos” – virialized halos of dark and baryonic matter with virial temperature $T < 10^4 K$ and masses $10^4 \lesssim M \lesssim 10^8 M_\odot$ – is sufficiently high so as to decouple its gas spin temperature from the CMB and the gas temperature is generally higher than T_{CMB} , causing it to appear in emission. ISFM predicted the corresponding fluctuating 21 cm signal from minihalos at redshifts $z > 6$. Iliev et al. (2003) extended these results to in-

clude non-linear biasing effects. These authors concluded that the fluctuations in intensity across the sky created by minihalos were likely to be observable by the next generation of radio telescopes. Such observations could confirm the basic CDM paradigm and constrain the shape and amplitude of the power spectrum at much smaller scales than previously possible. Recently, Furlanetto & Loeb (2004) suggested that the emission signal originating in shocked, overdense gas that is not inside of minihalos is probably much larger than that from minihalos alone as calculated by ISFM. Their conclusion is based on an extension of the Press-Schechter approximation that is used to determine the fraction of the intergalactic medium that is hot and dense enough to produce a 21 cm emission signal.

In this work, we predict the 21 cm signal at $z \gtrsim 8$ due to collisional decoupling from the CMB before the UV background is strong enough to make decoupling due to Ly α pumping important. Because the Ly α pumping efficiency is expected to fluctuate strongly until enough sources form to make the efficiency uniform (Barkana & Loeb e.g. 2004), the results presented here will also be relevant for isolated patches of the universe during reionization itself, which would depend upon the location and abundance of the first sources of UV radiation. Within such regions, we focus on properly resolving the gasdynamics of structure formation at small scales through the use of high resolution gasdynamic and N-body simulations. We test the semi-analytical prediction of the halo model of ISFM for the contribution to the mean signal from gas in minihalos, and investigate the extent to which IGM

gas may provide a non-negligible contribution to the total fluctuating signal, as suggested by Furlanetto & Loeb (2004). The outline is as follows. In § 4.2 we summarize the basic physics of the 21 cm emission and absorption and the analytical model of ISFM. We also describe our cosmological simulations and their initial conditions, and our method for obtaining the 21 cm signal from our simulations. In § 4.3 we present our results, with a discussion in § 4.4. Throughout this work, we use a flat, Λ CDM cosmology with matter density parameter $\Omega_m = 0.27$, cosmological constant $\Omega_\Lambda = 0.73$, baryon density $\Omega_b = 0.043$, Hubble constant $H = 70 \text{ km s}^{-1} \text{ Mpc}^{-1}$, $\sigma_{8h^{-1}} = 0.9$ and the Harrison-Zel’dovich primordial power spectrum.

4.2 The Calculation

4.2.1 Physics of 21 cm signal from neutral hydrogen

The 21 cm signal is due to the spin-flip transition of neutral hydrogen atoms. This hyper-fine structure signal in the radio band is, therefore, useful for probing the abundance of neutral hydrogen atoms. This transition could be excited by collisional excitation and/or Lyman-alpha pumping, which jointly determine the level populations through the “spin temperature,”

$$T_S = \frac{T_{\text{CMB}} + y_\alpha T_\alpha + y_c T_k}{1 + y_\alpha + y_c}, \quad (4.1)$$

where T_{CMB} is the CMB temperature, T_α is the color temperature of the Lyman- α photons, T_k is the kinetic temperature, y_α is the Lyman- α coupling constant, and y_c is the thermal coupling constant (Purcell & Field, 1956; Field,

1959). As seen in equation (4.1), the spin temperature deviates from T_{CMB} only when these couplings exist. Throughout this work, we will consider only the collisionally coupled gas, or the case where $y_\alpha = 0$. This is valid when 1) Lyman- α light sources were nonexistent at very high redshifts or 2) the region of interest is far away from ionizing sources, in regions not yet affected by Lyman- α pumping.

21-cm line can be observed in either absorption or emission against the CMB, with a differential brightness temperature given by

$$\delta T_b = \frac{T_S - T_{\text{CMB}}(z)}{1 + z} (1 - e^{-\tau}), \quad (4.2)$$

where the optical depth is given by

$$\tau = \frac{3\lambda_{10}^3 A_{10} T_* n_{\text{HI}}}{32\pi T_S H(z)}. \quad (4.3)$$

Here $\lambda_{10} = 21$ cm, $A_{10} (= 2.85 \times 10^{-15} \text{s}^{-1})$ is the Einstein A -coefficient for the 21-cm transition, $T_* = 0.068$ K is the excitation temperature, $H(z)$ is the Hubble constant at redshift z , and n_{HI} is the local density of neutral hydrogen. As our interest lies in the matter-dominated epoch, or $1 + z \gg 1$, $H(z) \approx H(0)\sqrt{\Omega_m}(1 + z)^{3/2}$. We also express the neutral hydrogen density in terms of the mean hydrogen density, local over-density $\delta \equiv (\rho - \bar{\rho})/\bar{\rho}$, and ionization fraction x , as $n_{\text{HI}} = n_H(1 - x)(1 + \delta)$. We then obtain the following expression for the local 21 cm optical depth

$$\tau = 1.08 \times 10^{-2} (1 + \delta)(1 - x) \left(\frac{h}{0.7}\right)^{-1} \left(\frac{\Omega_b h^2}{0.024}\right) \left[\left(\frac{1 + z}{10}\right) \left(\frac{0.27}{\Omega_m}\right)\right]^{1/2}, \quad (4.4)$$

where we have assumed that the ratio Ω_b/Ω_m , the baryon fraction in the matter component, follows the mean cosmic value everywhere. In most of the literature, where only linear and quasi-linear structures are considered, equation (4.2) is further approximated by assuming an optically thin limit ($\tau \ll 1$). Nonlinear structures, however, can obtain substantial optical depth (ISFM), and therefore when we apply equation (4.2) for calculating the signal from our simulation box, we do not make such an approximation.

4.2.2 Semi-analytic calculations

Here we briefly summarize parts of the semi-analytic calculation of the 21 cm signal from minihalos by ISFM which are relevant for this study. We also briefly discuss the effect of assuming a different halo mass function on the 21 cm signal, and compare to the signal obtained from an uniform IGM at different redshifts. All results are re-calculated here for the cosmological parameters reported by the Wilkinson Microwave Anisotropy Probe (WMAP), which are slightly different from the ones assumed in ISFM.

The hydrogen gas in minihalos, with $T_{\text{vir}} \leq 10^4 K$ is mostly neutral and sufficiently hot and dense to emit strongly at the 21 cm line. ISFM estimated the emission from individual minihalos and the mean radiation background and its fluctuations contributed by the combined effect of all minihalos. The beam-averaged “effective” differential antenna temperature $\overline{\delta T}_b$ is given by

$$\overline{\delta T}_b = \frac{c(1+z)^4}{\nu_0 H(z)} \int_{M_{\text{min}}}^{M_{\text{max}}} \Delta\nu_{\text{eff}} \delta T_{b,\nu_0} A \frac{dn}{dM} dM, \quad (4.5)$$

where $\Delta\nu_{\text{eff}}$, $\delta T_{b,\nu_0}$ and A are calculated based upon a CDM halo model called the truncated isothermal sphere (TIS) model (Shapiro et al., 1999; Iliev & Shapiro, 2001). The minimum minihalo mass M_{min} is set by the Jeans mass

$$M_{\text{J}} = 5.7 \times 10^3 \left(\frac{\Omega_0 h^2}{0.15} \right)^{-1/2} \left(\frac{\Omega_b h^2}{0.02} \right)^{-3/5} \left(\frac{1+z}{10} \right)^{3/2} M_{\odot}. \quad (4.6)$$

For M_{max} , ISFM used the mass for which the virial temperature is 10^4K :

$$M_{\text{max}} = 3.95 \times 10^7 \left(\frac{\Omega_0 h^2}{0.15} \right)^{-1/2} \left(\frac{1+z}{10} \right)^{-3/2} M_{\odot}. \quad (4.7)$$

The neutral baryonic fraction of halos with mass above M_{max} is uncertain, because hydrogen will be partially ionized due to collisions and photoionization by internal sources. Thus, the mass range from M_{min} to M_{max} naturally defines the mass range of minihalos.

Using equations (4.2) and (4.5) we can find the predictions for the mean 21 cm differential brightness temperature signal from mean, neutral IGM ($\delta = 0$, $x = 0$) and minihalos, respectively. We show the results in Figure 4.1. We consider minihalo mass functions given by both Press-Schechter (Press & Schechter, 1974) and Sheth-Tormen (e.g. Sheth & Tormen, 2002) approximations. The mean differential antenna temperature due to minihalos is of order of a few mK at $z \leq 20$. The mean 21 cm signal at $z \geq 20$ is dominated by the “unperturbed gas” mean IGM signal, which is in strong absorption against the CMB, since the minihalo collapsed fraction, f_{coll} , is very small at this epoch. At $20 < z < 1000$, the spin temperature of neutral hydrogen gas is decoupled from the CMB temperature by strong collisional coupling to the temperature

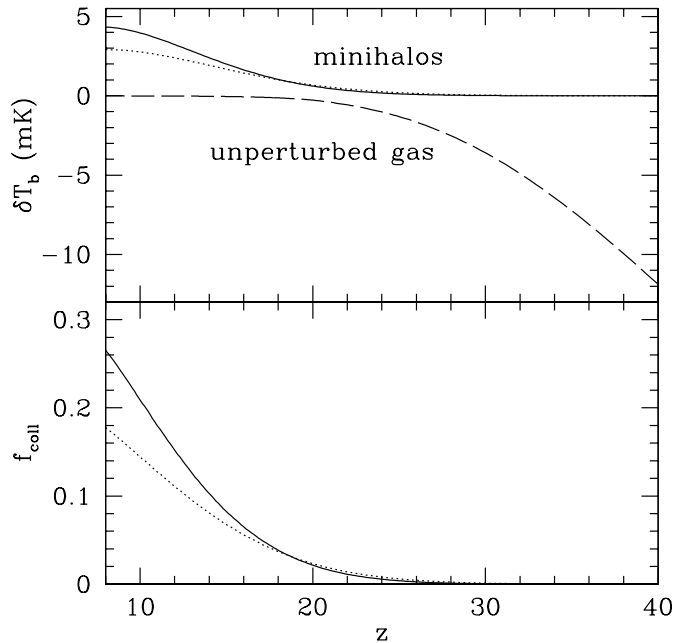


Figure 4.1: Analytical prediction for the mean 21 cm differential brightness temperature due to collisionally-decoupled minihalos and an unperturbed IGM. Shown are the results based on the Press-Schechter (solid) and the Sheth-Tormen (dotted) mass functions for halos and the contribution from the IGM gas with cosmic mean density and temperature (dashed). In the bottom panel we show the minihalo collapse fraction, again based on the Press-Schechter (solid) and the Sheth-Tormen (dotted) mass functions.

of the adiabatically cooled gas. At $z < 20$, the collisional coupling is weak and the spin temperature of unperturbed gas converges to the CMB temperature, making the IGM gas invisible.

4.2.3 Numerical Simulations

We have run series of cosmological N-body and gasdynamic simulations to derive the effect of gravitational collapse and the hydrodynamics on the predicted 21 cm signal from high redshift. Our computational box has a co-moving size of $0.5 h^{-1}$ Mpc, which is optimal for adequately resolving both the minihalos and the small-scale structure-formation shocks. We used the code described in Ryu et al. (1993), which uses the particle-mesh (PM) scheme for calculating the gravity evolution and an Eulerian total variation diminishing (TVD) scheme for hydrodynamics. We generated our initial conditions for the gas and dark matter distributions using the publicly available software COSMICS (Ma & Bertschinger, 1995). The N-body/hydro code uses an N^3 grid and $(N/2)^3$ dark matter particles. In order to check the convergence of our results we ran simulations at different spatial resolutions, with grid sizes 128^3 , 256^3 , 512^3 and 1024^3 , which we denote by C1, C2, C3 and C4, respectively. We report our results in § 4.3 based on our highest-resolution simulation C4 and discuss the convergence of the results in § 4.3.3.

After the decoupling of CMB photons from the baryonic gas, the IGM gas cools adiabatically due to cosmic expansion. For $z < 50$ the evolution of the temperature of the mean, unperturbed IGM gas is well approximated by the expression

$$T_{\text{gas}}(z) = T_{\text{CMB}}(z = 134) \left(\frac{1+z}{1+134} \right)^2. \quad (4.8)$$

For $z \lesssim 50$, equation (4.8) agrees, for instance, with the solution to the equation (1) in Bharadwaj & Ali (2004) which describes how T_{gas} evolves exactly.

This temperature, $T_{\text{gas}}(z)$, was used in the simulation to set the minimum temperature of baryonic gas, to avoid negative temperatures¹. If a gas cell is cooled below $T_{\text{gas}}(z)$, its temperature is set back to $T_{\text{gas}}(z)$. Such a temperature “floor” may overestimate the gas temperature of underdense regions, but because of their low density and temperature, y_c is small in these regions. Since y_c is negligible in such regions, the spin temperature T_S would be very close to T_{CMB} , and their contribution to δT_b would also be negligible, whether the kinetic temperature T_K is calculated accurately or not.

In addition to the total 21 cm signal from our simulations, $\overline{\delta T}_{b,\text{IGM}}$, we are also interested in the relative contribution of the virialized minihalos and the IGM to the total signal, the sum of which gives the total 21 cm signal, $\overline{\delta T}_{b,\text{tot}} = \overline{\delta T}_{b,\text{halo}} + \overline{\delta T}_{b,\text{IGM}}$. First, we calculate the total mean signal as a simple average over the simulation cells, $\overline{\delta T}_{b,\text{tot}} \equiv \sum_i \delta T_{b,i}/N$. The minihalo contribution is given by $\overline{\delta T}_{b,\text{halo}} \equiv \sum_i f_i \delta T_{b,i}/N$, where f_i is the fraction of mass in a cell i which is part of a halo. The IGM contribution can then be obtained as

$$\overline{\delta T}_{b,\text{IGM}} = \overline{\delta T}_{b,\text{tot}} - \overline{\delta T}_{b,\text{halo}} = \sum_i (1 - f_i) \delta T_{b,i}/N. \quad (4.9)$$

In order to calculate the minihalo contribution to the total differential brightness temperature, $\overline{\delta T}_{b,\text{halo}}$, one needs to first identify the halos in the

¹One should, in principle, use the locally varying minimum temperature. However, usage of a global minimum temperature is well justified as described in the text, and it is computationally cheaper than implementing a locally varying minimum temperature.

simulation volume. We identified the halos using a friends-of-friends (FOF) algorithm (Davis et al. 1985) with a linking length parameter of $b = 0.25$. The FOF algorithm applies to the dark matter, rather than the gas. Thus, the minihalo collapsed fraction in each cell, f_i , is determined by the triangular-shaped cloud scheme to assign the dark matter density to the corresponding grid cells.

4.2.3.1 Semi-Analytical Calculation of the Halo Contribution

Our numerical simulations have sufficiently high resolution to find all halos in the computational box and the large-scale structure formation shocks, but not to resolve the internal structure of the minihalos themselves. However, as ISFM have shown, in order to obtain the correct 21-cm signal from minihalos one needs to do a full radiative transfer calculation through each individual minihalo density profile since, unlike the IGM gas, minihalos have a non-negligible optical depth at the 21-cm line. Hence, we can refine our estimate of the minihalo contribution to the total 21-cm signal by combining our numerical halo catalogues with the semi-analytic calculation of individual minihalo contribution as found by ISFM. In their approach, the gas density of each minihalo is assumed to follow a TIS profile Iliev & Shapiro (2001), radiative transfer calculation is performed for different impact parameters, and then finally the face-averaged δT_b is calculated (see Iliev et al., 2002, for details). The halo mass function, dn/dM , is provided by the halo catalogue we construct from the simulation. Each individual halo contribution, $\Delta\nu_{\text{eff}}\delta T_{b,\nu_0}A$, depends

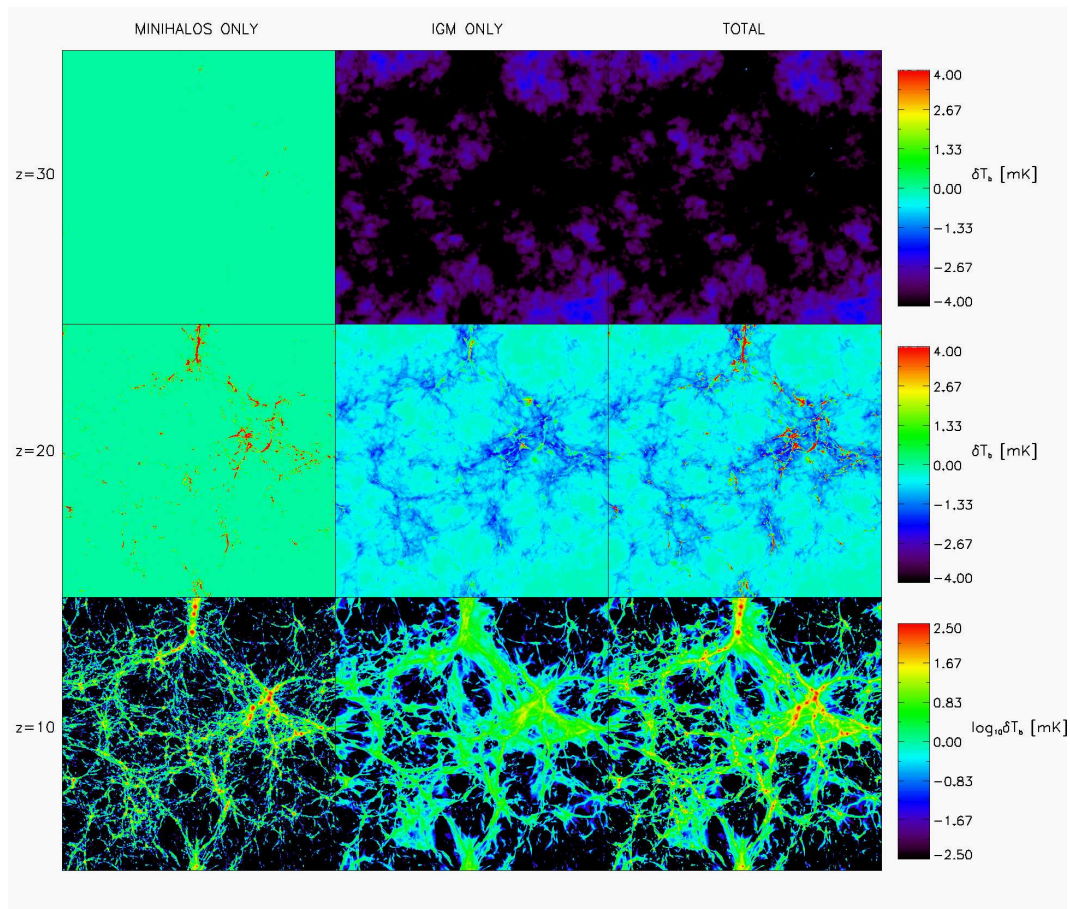


Figure 4.2: Map of the differential brightness temperature δT_b (mK) for the the 21 cm signal obtained from our highest resolution simulation, C4. Rows, top to bottom, show redshifts $z=30$, 20, and 10. columns, left to right, represent contributions from minihalos, the IGM and the total signal. Note that the scale is linear for the upper two rows of images, but logarithmic for the bottom row.

on its mass and redshift of formation (ISFM). Once we calculate $\Delta\nu_{\text{eff}}\delta T_{b,\nu_0}A$, we then obtain the halo contribution using equation (4.5).

In summary, following this prescription allows us to estimate the 21-cm signal more accurately from minihalos, as 1) the minihalo internal density profiles and temperatures are not fully resolved in our simulations and 2) we do not perform an exact radiative transfer through minihalos when obtaining the 21-cm signal from our simulations.

4.3 Results

4.3.1 Numerical 21 cm Brightness Temperature from Minihalos vs. IGM

In this section, we describe the results from our simulations. In Figure 4.2 we show (unfiltered) maps of the differential brightness temperature obtained directly from our numerical data (simulation C4), as described in § 4.2. We show the total signal, as well as the separate contributions from minihalos and IGM, derived as we described in § 4.2.3, at redshifts $z = 30$, 20, and 10. At $z = 30$, the earliest redshift shown (top row), most of the diffuse IGM gas is still in the quasi-linear regime and cold, thus largely in absorption against the CMB. At redshift $z = 20$ (middle row), the diffuse gas is again largely in absorption, while the (relatively few) halos that have already collapsed are in strong emission. The combination of the two contributions creates a complex, patchy emission/absorption map and partial cancellation in the total mean signal. Finally, at $z = 10$ (bottom row) most of the gas,

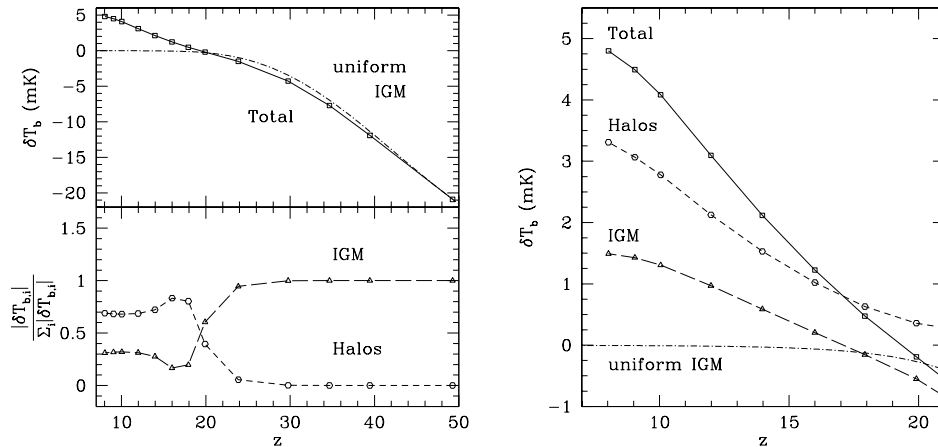


Figure 4.3: 21 cm mean brightness temperature evolution. (a)(left) Evolution of the total 21-cm signal vs. redshift. All data points are directly calculated from our simulation box, with the assumption that optical depth is negligible throughout the box and using simulation C4. (b)(right) δT_b vs. redshift below $z = 20$. Plotted are the contributions from minihalos (labeled Halos, circles), the IGM (triangles) and the total (squares).

including its diffuse component, is heated and in emission against the CMB. The bulk of the 21 cm emission comes from the high-density knots and filaments. Although both the halo and IGM contributions come from roughly the same regions, the minihalo emission is significantly more clustered, while the IGM emission is quite diffuse.

In Figure 4.3 we show the evolution of the mean 21 cm signal averaged over the whole computational box. The evolution roughly follows the naive analytical estimates, as was shown in Figure 4.1. The total signal is in deep absorption, with $\delta T_b < 10$ mK at $z > 37$. The 21 cm signal is completely dominated by the IGM contribution. The absorption signal follows the an-

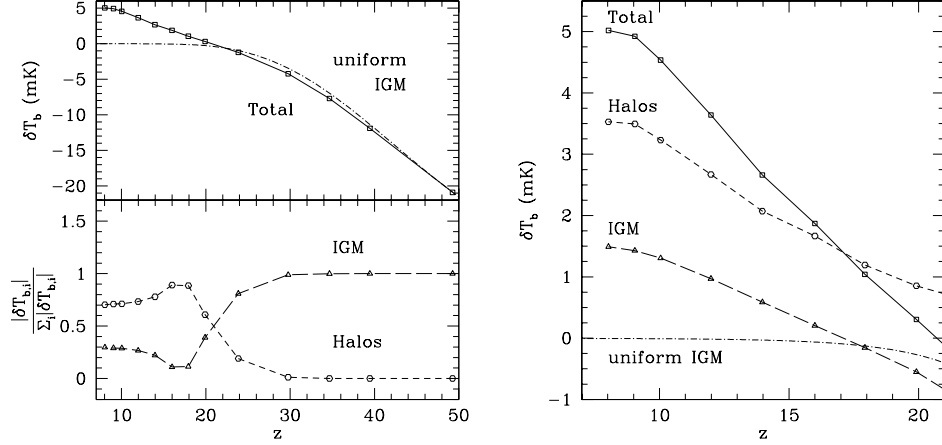


Figure 4.4: Semi-analytical minihalo signal vs. IGM signal. The 21 cm flux from each halo in the simulation is found by modeling the halos as described in § 4.2.3.1, to estimate the halo 21 cm signal more accurately. Same notation as in Figure 4.3. The 21 cm minihalo emission increases compared to the raw minihalo signal in figure 4.3. The IGM signal remains the same.

analytical prediction well, since the density fluctuations are still small and the uniform-density assumption is reasonably accurate. The absorption continually decreases as significant nonlinear structures start forming and portions of the gas became heated due to this structure formation. The signal goes into overall emission after redshift $z \sim 18$, reaching up to ~ 4 mK. The emission signal at $z \lesssim 18$ is due to both collapsed halos and the clumpy, hot IGM gas. In terms of relative contributions, the minihalo signal dominates over the diffuse IGM signal at all times when the overall signal is in emission, below $z \approx 18$. We find that the relative contributions to the total signal, $|\delta T_{b,j}| / (|\delta T_{b,\text{halo}}| + |\delta T_{b,\text{IGM}}|)$ where j means either “halo” or “IGM”, is nearly

constant over two different redshift regimes: for $z > 20$,

$$|\delta T_{b,\text{IGM}}| / (|\delta T_{b,\text{halo}}| + |\delta T_{b,\text{IGM}}|) \approx 1, \quad (4.10)$$

while for $z < 16$,

$$|\delta T_{b,\text{halo}}| / (|\delta T_{b,\text{halo}}| + |\delta T_{b,\text{IGM}}|) \approx 0.7. \quad (4.11)$$

In the transition region, $16 < z < 20$ the relative contributions exhibit more complex behavior, to approximately cancel out, resulting in a total signal which is close to zero.

4.3.2 Refined Estimate of the Simulated Minihalo 21 cm Signal

As we discussed in § 4.2.3.1, we can improve our purely numerical estimate on the minihalo 21 cm signal by replacing each halo’s flux with the value obtained by detailed radiative transfer calculation. We obtain the total minihalo signal from equation (4.5), with the theoretical mass function dn/dM replaced by the halo catalogue obtained from the simulations, and the individual minihalo contributions, $\Delta\nu_{\text{eff}}\delta T_{b,\nu_0}A$, calculated by modeling each halo as a TIS.

We find that the resulting 21 cm signal from halos is stronger than the one obtained directly from the simulated halos and dominates the overall emission signal even more (Fig. [4.4]). This is despite the fact that considering more centrally-concentrated analytical density profiles increases the optical depth of each halo. We attribute this non-intuitive behavior to the fact that

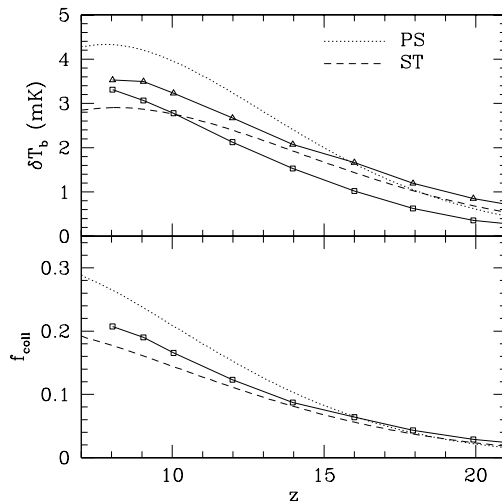


Figure 4.5: (a)(top) Differential brightness temperature of the 21 cm signal from minihalos for semi-analytical model (dotted: with Press-Schechter mass function; dashed: with Sheth-Tormen mass function), simulation C4 numerical result (squares) and semi-analytical calculation (§ 4.2.3.1) based upon simulation C4 mass function (triangles). (b)(bottom) Minihalo collapse fraction from simulation C4 (squares) and analytical mass functions (linetypes follow those of the top panel).

the density profiles of the minihalos found in our simulations are not fully resolved. By modeling the halo density profiles in detail, the local density inside halos is boosted which significantly increases the coupling constant y_c , which in its turn increases the total emission signal, even though the optical depth through each halo also increases simultaneously. Note that we use the same halo abundances for both estimates, and only the internal halo properties are modified.

In Figure 4.5 we show the result obtained from the simulations com-

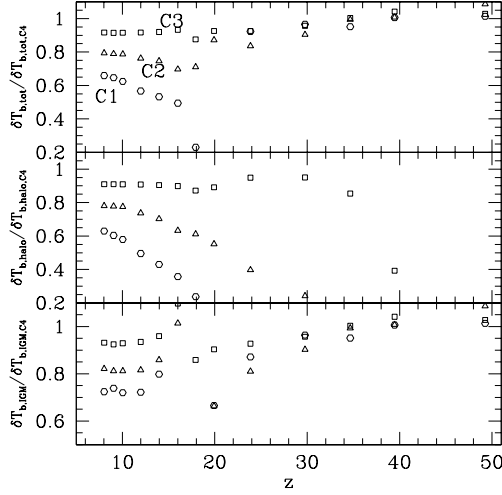


Figure 4.6: Differential brightness temperature signals for simulations C1 (squares), C2 (triangles) and C3 (circles) in units of the corresponding signal obtained from simulation C4. Shown are the total (top panel), halos only (middle panel) and IGM only (bottom panel) 21 cm signal.

pared to the theoretical PS and ST halo mass functions. We also show the minihalo contribution to the total differential brightness temperature signal. We see that the collapsed fraction in minihalos roughly agrees with the theoretical predictions, mostly lying between the PS and ST results. On the other hand, the minihalo contribution to the total 21 cm background obtained directly from the simulation is below the theoretical predictions based on either PS or ST mass functions. The agreement is restored, however, when we replace each minihalo contribution to the total flux by its analytically-modeled value. This once again underscores the importance of resolving the internal halo structure for correct predictions of their 21 cm emission.

4.3.3 Convergence

We now compare cases C1, C2, C3 and C4 to check the robustness of our results with respect to numerical convergence. In Figure 4.6 we show the differential brightness temperature signals for simulations C1, C2 and C3 in terms of the signal obtained from simulation C4. We show the total signal, as well as each separate contribution, from either the halos or the IGM gas. At $z \gtrsim 20$ most of the gas density fluctuations are still linear and a change in the resolution barely affects the results, thus a modest-resolution simulation, or even an analytical estimate, suffices to obtain reliable results. In contrast, at lower redshifts ($z \lesssim 20$) the results depend strongly on the resolution. The low-resolution simulations C1 and C2 underestimate the resulting 21 cm signal significantly, by factors up to a few. The results from these simulations improve somewhat at lower redshifts, below $z = 10$, but results are still below the ones from C4 by factors of $\sim 30 - 50\%$ and $\sim 20\%$ for simulations C1 and C2, respectively. This is justifiable for either the minihalo, IGM or the total signal. The results from our medium-resolution simulation C3, on the other hand, are much closer to the ones from the high-resolution simulation C4, with the two generally agreeing to better than 10%. This indicates convergence of our results to few per cent for simulation C4. Such behavior could be naively expected, since at $z \lesssim 20$ non-linear structures, both collapsed halos and mildly nonlinear, shocked IGM gas, form in abundance at the scales we are investigating, and thus high resolution is required to resolve these properly, as our simulations confirm.

The relative contribution of the minihalo and the IGM signals, on the other hand, shows a more robust convergence. In all cases of different resolutions, we find that the minihalo signal dominates the IGM signal at $z \lesssim 20$, while the IGM signal dominates the minihalo signal at $z \gtrsim 20$. For the purely numerical result, the relative contribution to the emission signal is about 70% at $z < 15$, peaks at $z \approx 18$, and drops to 50% at $z \approx 20$. The exact value of the transition redshift varies slightly with resolution. For $z \lesssim 14$ minihalos contribute $\sim 70\%$ of the emission signal. For the case of semi-analytical calculation of the minihalo contribution based on the simulated halo catalogues, the relative contribution to the emission signal is slightly higher.

4.4 Conclusions

We have run a set of cosmological N-body and hydrodynamic simulations of the evolution of dark matter and baryonic gas at high redshifts ($8 < z < 100$). With the assumption that radiative feedback effects from the first light sources are negligible, we calculated the 21 cm mean differential brightness temperature signal. The mean global signal is in absorption against the CMB above $z \sim 20$ and in overall emission below $z \sim 18$. At $z \gtrsim 20$, the density fluctuations of the IGM gas are largely linear, and their absorption signal is well approximated by the one that results from assuming uniform gas at the mean adiabatically-cooled IGM temperature. At $z \lesssim 20$, nonlinear structures become common, both minihalos and clumpy, hot, mildly nonlinear IGM, resulting in an overall emission at 21 cm with differential brightness

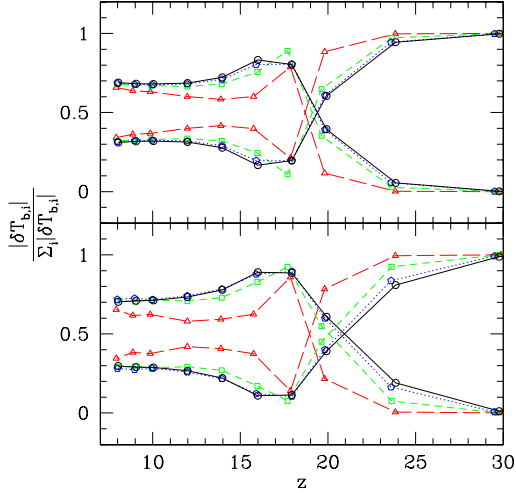


Figure 4.7: Relative contributions of minihalos and diffuse IGM gas to the total 21-cm background. The top panel shows the results obtained directly from simulations (C1: triangle, long-dashed; C2: square, short-dashed; C3: pentagon, dotted; C4: circle, solid). The bottom panel shows the results which were semi-analytically refined (§ 4.2.3.1; point- and line-types follow those of the top panel).

temperature of order a few mK.

By identifying the halos in our simulations, we were able to separate and compare the relative contributions of the halos and the IGM gas to the total signal. We find that the emission from minihalos makes about 70 – 75% contribution to the total emission signal at $z \lesssim 17$, peaking at $z \approx 18$, and balancing the absorption by the IGM gas at $z \approx 20$. In contrast, the absorption by cold IGM gas dominates the total signal for $z \gtrsim 20$.

Throughout this work, we have neglected the Lyman- α pumping. As mentioned earlier, this is true when there are no light sources at very high

redshifts ($z \gtrsim 20$), or when a region of interest is not ionized and is not affected by the Lyman- α pumping. To make a prediction for those regions affected by relevant light sources, one should incorporate the corresponding baryonic physics such as ionization and heating. In the future, we plan to improve upon the current calculation by adopting such complicated physics. We also intend to run simulations with larger simulation boxes, which would allow us to also predict the 21 cm fluctuation signal (e.g. ISFM). The box size we adopted here is too small compared to the length scale of such fluctuation signal. Whether the relative contribution from minihalos to the total signal, which we find to be about 70 - 75 % at $z \lesssim 20$, varies with such fluctuation is not clear at this point. The future work will also allow us to answer this question.

Chapter 5

Second-Generation Star Formation In the Early Universe

5.1 Introduction

The formation and evolution of the first nonlinear structures are strongly affected by complicated baryonic gas physics. Recent theoretical and observational developments have allowed for the study of the formation, evolution, and feedback effects of nonlinear structures on the environment at high redshift universe more accurately. One of the main topics in this field is the study of the formation and evolution of the first stars and their radiative, chemical, and dynamical feedback effects.

The first stars are born in a primordial environment where the extreme case of zero metallicity applies. These stars constitute the Population III (Pop III) stars. Formation of the first stars in the cosmological context has been studied recently using powerful hydrodynamic simulation techniques (Bromm, Coppi, & Larson 1999; Bromm et al. 2002; Nakamura & Umemura 2001; Abel, Bryan, & Norman 2000, 2002; Yoshida et al. 2003). As there are no metals at this stage, hydrogen molecules (H_2) play an important role in cooling the baryonic gas to form protostars and ultimately the first stars (for importance of

H₂ cooling, see Peebles & Dicke 1968; Lepp & Shull 1984; Shapiro & Kang 1987; for formation of the first stars, see Bromm et al. 1999; Abel et al. 2000; Yoshida et al. 2003). With primordial chemistry with H₂ treated properly, these studies find that the first stars gain high mass in the range of $M \gtrsim 100 M_{\odot}$.

The first stars impact their environment with various feedback effects. Due to their mass scale, strong ultraviolet (UV) photons are produced to contribute to the reionization of the universe (e.g. Tumlinson & Shull 2000; Bromm et al. 2001; Schaerer 2002, 2003; Tumlinson, Shull, & Venkatesan 2003; Venkatesan & Truran 2003). The large optical depth to Thomson scattering of the cosmic microwave background (CMB) photons has been interpreted as a signature of an early episode of massive star formation at redshift $z \gtrsim 15$ (Kogut et al. 2003). Supernova (SN) explosions at the end of the lifetime of the first stars could have been responsible for the initial metal enrichment of the intergalactic medium (IGM) (e.g. Shapiro, Giroux, & Babul 1994; Wada & Venkatesan 2003; Yoshida, Bromm, & Hernquist 2004, and references therein).

Much attention has been paid to understanding the radiative feedback effects of these first stars on the formation of second generation of stars. This subject has been a matter of debate in terms of the negative vs. the positive feedback effects on the subsequent formation of H₂. On the one hand, Haiman, Rees, & Loeb (1997), Haiman, Abel, & Rees (2000), Ciardi, Ferrara, & Abel (2000), Machacek, Bryan, & Abel (2001) find that even a feeble UV background would photodissociate and quench further formation of H₂ (negative). On the other hand, Ricotti, Gnedin, & Shull (2002) find that a thin

H_2 shell forms in the IGM ahead of the I-front because the precursor of the I-front provides enough electrons to create H_2 (positive). In the regime where the X-ray background is strong, partial ionization by hard photons would also form H_2 (positive; Haiman, Rees, & Loeb 1996; Glover & Brand 2003).

Recent studies by O’Shea et al. (2005) and Alvarez, Bromm, & Shapiro (2005) address this question for nonlinear structures in the vicinity of Pop III stars. Assuming that nearby halos would be fully ionized by the UV photons from a Pop III star, O’Shea et al. (2005) find that halos embedded in the H II region of a Pop III star would easily form H_2 after the death of the star due to the residual electron fraction from ionization. Alvarez et al. (2005), on the other hand, by tracking the ionization front (I-front), find that the I-front is trapped inside these halos before reaching the high-density region (core) due to the high column density of neutral hydrogen. According to Alvarez et al. (2005), it seems that the initial assumption of full ionization of nearby halos by O’Shea et al. (2005) is invalid. However, it is not clear whether the results of Alvarez et al. (2005) indicate a negative feedback effect.

Motivated by O’Shea et al. (2005) and Alvarez et al. (2005), we study the radiative feedback effects of Pop III stars onto their nearby halos in detail using the 1-D spherical radiation-hydrodynamics code in which we accurately calculate the primordial gas chemistry. In §5.2 we describe the details of the 1-D spherical radiation-hydrodynamics code we have developed. In §5.3, we describe the initial setup of the problem. We describe our results in §5.4, and discuss the results and their implications in §5.5.

5.2 1-D spherical, radiation hydrodynamics code with primordial chemistry network

In this section, we describe in detail the 1-D spherical, Lagrangian, radiation-hydrodynamics code we have developed. Dark matter and baryon shells are allowed to move in the Lagrangian way. This code has four major components, which are coupled in a proper way: A) gravity, B) cooling and heating, C) radiative transfer, and D) nonequilibrium chemistry. We describe each component in the following subsections separately. Finite-differencing scheme used for this code is described in Appendix B. We include the neutral and ionic species of H, He, and H₂, in order to treat the primordial chemistry; for simplicity, we neglect D and Li species¹.

5.2.1 Hydrodynamic Conservation Equations

The baryonic gas is subject to fluid conservation equations,

$$\frac{\partial \rho}{\partial t} + \frac{\partial}{\partial r}(r^2(\rho u)) = 0, \quad (5.1)$$

$$\frac{\partial}{\partial t}(\rho u) + \frac{\partial}{\partial r}(p + \rho u^2) + \frac{2}{r}\rho u^2 = -\rho \frac{Gm}{r^2}, \quad (5.2)$$

$$\frac{De}{Dt} = -\frac{p}{\rho} \frac{\partial}{\partial r}(r^2 u) + \frac{\Gamma - \Lambda}{\rho}, \quad (5.3)$$

¹D and Li components have been usually neglected due to their relatively low abundance, hence the negligible contribution to cooling (e.g. Lepp & Shull 1984; Shapiro & Kang 1987). However, recent study by Johnson & Bromm (2005) indicates that HD cooling might cool strongly-shocked primordial gas to the temperature of the CMB. On the other hand, as the HD cooling process is unimportant in cases where the gas does not go through an ionized phase (Alvarez et al. 2005), we may safely neglect the HD process in our calculation as long as such conditions are met. We will discuss this issue further in §5.4.3.

where $e \equiv (3p)/(2\rho)$ is the internal energy per unit baryon mass, Γ is the external heating rate, and Λ is the external cooling rate. Note that all the variables in equations (5.1) - (5.3) denote the baryonic properties, except for m , the mass enclosed by a radius r , which is composed of both the dark matter mass and the baryon mass.

5.2.2 Gravity

Gravity is contributed both by the dark matter and the baryonic components. Let us first focus on the dark matter component. In order to treat the dark matter gravity under spherical symmetry, almost all previous studies have used either a frozen dark matter potential or a set of self-gravitating dark matter shells in radial motion only (e.g. Thoul & Weinberg 1995). Both methods have their own limitations. The frozen potential approximation cannot address the effect of a possible evolution of gravitational potential. The radial-only dark matter shells suffer from the fact that the corresponding structure has a steeper density profile than that of halos in cosmological, 3-D N-body simulations (§2.4.5).

The fluid approximation we developed (§2.2) was indeed motivated by these limitations. We use the usual fluid conservation equations (equ. [2.20], [2.21], [2.22]) to handle the motion of dark matter particles; see §2.2 for justification. Note that dark matter shells in this code represent a collection of dark matter particles in spherical bins, in order to describe “coarse-grained” properties such as the density (ρ), pressure ($p \equiv \rho (\langle v_r^2 \rangle - \langle v_r \rangle^2) = \rho (\langle v_\theta^2 \rangle - \langle v_\theta \rangle^2)$),

etc. The mass enclosed by a dark matter shell of radius r

$$m(< r) = m_{\text{DM}}(< r) + m_{\text{bary}}(< r) \quad (5.4)$$

enters equation (2.21). In order to compute $m(< r)$ accurately, we properly account for the mismatch of the location of dark matter shells and baryon shells. Note that the gravity acting on baryonic shells are also described by the mass expressed by the equation (5.4), and the corresponding hydrodynamic equations will be described in §5.2.1.

5.2.3 heating / cooling

- *heating*

Photoheating results from thermalization of the residual kinetic energy of electrons after they are photoionized. In general, the photoheating function is described by

$$\Gamma = \sum_i \Gamma_i = \sum_i n_i \int_0^\infty d\nu \frac{4\pi J_\nu \sigma_\nu}{h\nu} (h\nu - h\nu_{i,\text{th}}), \quad (5.5)$$

where individual heating functions ($\{\Gamma_i\}$) of species i are summed to generate the net heating function Γ .

For the cases of an internal point source (§5.2.4.1) and an external, plane wave source (§5.2.4.2), we can easily implement the photon-conserving scheme. For an internal point source,

$$4\pi J_\nu = F_\nu^{\text{int}}, \quad (5.6)$$

where F_ν^{int} is the internal flux incident on the gas at a given radius, and σ_ν is replaced by

$$\sigma_{i,\nu} = \frac{1 - e^{-\Delta\tau_{i,\nu}}}{n_i dr_k}, \quad (5.7)$$

in the photon-conserving way. Similarly, for a plane parallel external source,

$$4\pi J_\nu = F_\nu^{\text{ext}}, \quad (5.8)$$

where F_ν^{ext} is the external flux incident on the gas at a given radius r given by

$$F_\nu^{\text{ext}} = F_\nu(R_*) \left(\frac{D}{R_*} \right)^{-2} e^{-\tau_\nu}. \quad (5.9)$$

D is the distance from the source to the halo ($D \gg \text{size of the halo}$), and

$$\tau_\nu = \sum_i N_i(> r) \sigma_{i,\nu} \quad (5.10)$$

is the optical depth from the edge of the halo to the radius r . A hybrid expression is also possible when both an internal point source and an external plane parallel source are present:

$$\Gamma_i = n_i \int d\nu \frac{F_\nu^{\text{int}}(r_{k-1/2}) + F_\nu^{\text{ext}}(r_{k+1/2})}{h\nu} \cdot \frac{1 - e^{-\Delta\tau_{i,\nu}}}{n_i dr_k} (h\nu - h\nu_{i,\text{th}}). \quad (5.11)$$

For an isotropic external background, as described in §5.2.4.2, it is rather complicated to implement the photon-conserving scheme. Thus, at this stage, we simply use equation (5.5) without replacing $\sigma_{i,\nu}$. In the future, we will implement the photon-conserving scheme for an isotropic external source if we come up with a clearer idea.

- cooling

Cooling occurs through various processes. For atomic species, it comes from collisional excitation, collisional ionization, recombination, free-free emission, and CMB photons scattering off free electrons (Compton cooling/heating). For atomic H and He, cooling is dominated by collisional excitation (for $T \lesssim 2 \times 10^5 \text{K}$) and free-free emission (for $T \gtrsim 2 \times 10^5 \text{K}$). The atomic cooling rate decreases rapidly at $T \lesssim 10^4 \text{K}$, as there are no collisions energetic enough to cause excitation. It is difficult, therefore, to cool gas below $T \approx 10^4 \text{K}$ solely by atomic cooling of primordial gas.

H_2 , however, is able to cool gas below $T \approx 10^4 \text{K}$ down to $T \approx 100 \text{K}$ through its molecular line transitions. An important question to address is how much H_2 is created, maintained, or destroyed in working as an active coolant under the influence of an ionizing and dissociating radiation field. A small fraction, $n_{\text{H}_2}/n_{(\text{H})} \gtrsim 10^{-4}$, is found to be enough to cool gas below 10^4K (e.g. see Shapiro & Kang 1987), but the radiative feedback effect of a background on its abundance is still in debate (§5.1).

We use cooling rates in the parametrized forms given by Anninos et al. (1997). We point out that there exists a slight difference between the case A and case B recombination cooling rates. However, the exact value of the recombination cooling rate is not important, simply because it is not a dominant cooling process. We find by experiment that the temperature profile hardly changes even when we neglect the recombination cooling term.

5.2.4 Radiative transfer

5.2.4.1 Internal source

We treat the internal source as a point source, which is a good approximation if the size of the source is negligible compared to the size of the halo. For instance, such an approximation is valid when a single Pop III star ($R_* \sim$ a few R_\odot) is embedded in a halo of size $R \sim [10 - 100]$ pc. This allows one to use radial-only rays from the source.

Diffuse flux also contributes to the radiative feedback effects. At this stage, we do not explicitly treat the diffuse flux in the code. We instead use the on-the-spot approximation to approximate the effect of the diffuse flux from hydrogen, or equivalently, use the hydrogen case B recombination rate. We neglect the diffuse flux from other species because of their low cosmic abundance.

With such approximations, the solution to the radiative transfer equation of the specific intensity I_ν ($\text{erg s}^{-1} \text{cm}^{-2} \text{ster}^{-1} \text{Hz}^{-1}$),

$$\frac{dI_\nu}{d\tau_\nu} = -I_\nu + S_\nu, \quad (5.12)$$

can then be expressed in terms of a differential flux F_ν^{int} ($\text{erg s}^{-1} \text{cm}^{-2} \text{Hz}^{-1}$) at radius r simply by

$$F_\nu^{\text{int}}(r) = F_\nu^{\text{int}}(R_*) \left(\frac{r}{R_*} \right)^{-2} e^{-\tau_\nu(r)} = \frac{L_\nu^{\text{int}}}{4\pi r^2} e^{-\tau_\nu(r)}, \quad (5.13)$$

where $F_\nu(R_*)$ is the differential flux at the surface ($r = R_*$) of the source, L_ν ($\text{erg s}^{-1} \text{Hz}^{-1}$) is the differential luminosity of the source, and the optical

depth τ_ν is given by

$$\tau_\nu(r) = \sum_i N_i(< r) \sigma_{i,\nu}, \quad (5.14)$$

where $N_i(< r)$ (cm^{-2}) is the column density of species i from the surface of the source to the radius r , and $\sigma_{i,\nu}$ is the absorption cross section for ionization/dissociation of species i at frequency ν . In practice, H, H^- , He, He^+ , H_2 , and H_2^+ are the species considered in equation (5.14). The cross section of the neutral hydrogen atom, $\sigma_{\text{H},\nu}$, may vary depending upon the assumption of case A or case B recombinations.

H_2 photo-dissociating photons can be self-shielded by a high column density of H_2 . Exact calculation of self-shielding requires a full treatment of 76 Lyman-Werner lines, even when only the lowest energy level transitions are included. We use a simple shielding factor parametrized by the molecule column density N_{H_2} ,

$$F_{\text{shield}} = \min \left[1, \left(\frac{N_{\text{H}_2}}{10^{14} \text{cm}^{-2}} \right)^{-3/4} \right], \quad (5.15)$$

following Draine & Bertoldi (1996). The photodissociation rate is then given by

$$k_{\text{H}_2} = 1.38 \times 10^9 (J_\nu)_{h\nu=12.87\text{eV}} F_{\text{shield}}. \quad (5.16)$$

This approximation has been widely used in the study of high redshift structure formation (e.g. Kitayama et al. 2001; Glover & Brand 2001; Yoshida et al. 2003; Kitayama et al. 2004). In the case of an internal point source, the mean intensity J_ν at radius r becomes $J_\nu^{\text{int}}(r) = F_\nu^{\text{int}}(r)/(4\pi)$. F_{shield} in equation (5.15) can also be generalized to the case of an isotropic external source, simply

by averaging F_{shield} over different angles (Kepner, Babul, & Spergel 1997; see also §5.2.4.2).

These radiative rate coefficients, as well as the collisional rate coefficients, either decrease or increase the number density of a given species depending upon the reaction network. For instance, the neutral hydrogen number density changes as

$$\frac{dn_{\text{HI}}}{dt} = -k_1 n_{\text{HI}} n_{e^-} + k_2 n_{\text{HII}} n_{e^-} - k_{24} n_{\text{HI}}, \quad (5.17)$$

where k_1 is the collisional ionization rate, k_2 is the recombination rate, and k_{24} is the photoionization rate (we use the convention that rate coefficients $\{k_i\}$ are positive numbers). We will not list all the relevant processes here. We instead refer curious readers to Shapiro & Kang (1987) and Abel et al. (1997), where detailed descriptions of the rate equations are provided. Note that we used, in practice, the set of equations and the fitting function for rate coefficients implemented in the Fortran77 routine “species_solver.f”, which is included in the primordial chemistry solving package by Abel et al. (1997), publicly available from the “Tom Abel’s Primordial Chemistry” website at <http://cosmos.ucsd.edu/~tabel/PGas/>.

5.2.4.2 External source

- *case A: Isotropic external source*

If radiation fields from individual sources overlap, a nearly isotropic background field will build up. One clear example is the CMB, but one could

also imagine, for instance, a UV background formed by radiation from individual sources such as quasars and the first stars.

For the case in which an object is optically thin to the background, the mean intensity J_ν^{ext} inside the object is uniform. In general, an object can be optically thick to the background, and the mean intensity J_ν^{ext} at a certain point in the object can be different from the background value. Here, we describe how $J_\nu^{\text{ext}}(r)$ and the corresponding ionization and dissociation rate coefficients in a spherically symmetric object are calculated.

Our method to calculate $J_\nu^{\text{ext}}(r)$ is very similar to that of Kepner et al. (1997). The mean intensity at radius r is given by

$$J_\nu^{\text{ext}}(r) = \frac{1}{2} J_\nu(r_{\text{halo}}) \int_{-1}^{+1} \exp[-\tau_\nu(r, \mu)] d\mu, \quad (5.18)$$

where r_{halo} is the outermost radius of the object, $J_\nu(r_{\text{halo}})$ is the background intensity, $\mu = \cos \theta$, and

$$\tau_\nu(r, \mu) = \sum_i \sigma_{i,\nu} N_i(r, \mu). \quad (5.19)$$

The column density of each species along each line of sight is

$$N_i(r, \mu) = \int_0^{l(r, r_{\text{halo}}, \mu)} n_i[r'(x)] dx, \quad (5.20)$$

where $l(r, r_{\text{halo}}, \mu) = r\mu + [r_{\text{halo}}^2 - r^2(1 - \mu)^2]^{1/2}$, $r'(x) = [r^2 + x^2 - 2rx\mu]^{1/2}$ (see Fig. [5.1]). The photoionization and photodissociation coefficients are then given by

$$k_i = 4\pi \int_0^\infty \frac{\sigma_{i,\nu} J_\nu^{\text{ext}}(r)}{h\nu} d\nu. \quad (5.21)$$

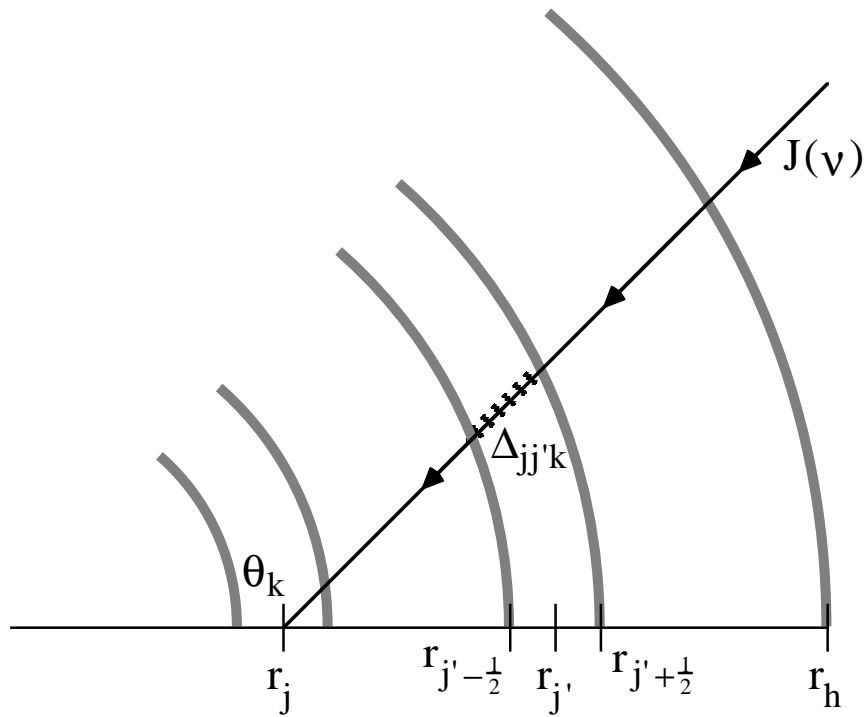


Figure 5.1: Geometry for radiative transfer for an isotropic background of mean intensity $J_\nu(r_{\text{halo}})$ (denoted by $J(\nu)$ in this figure). $\Delta_{jj'k}$, a distance traveled through shell j' by an incoming ray bound for shell j at an angle θ_k , is used to get column densities of various species.

- case B: External source as a plane wave

We also consider a special case of external source, a plane wave incident on a spherical halo. This is an attempt to use our 1-D spherical code to simulate the problem we proposed, namely the radiative feedback effects of a Pop III star onto its nearby halos. We show in this section, even though our code has the limitation of spherical symmetry, that one can tackle such a spherically asymmetric problem if one focuses on a narrow cylindrical (conic, more precisely; see Fig. [5.2]) region connecting the source and the center of the target halo. In this case, the flux at radius r from the center of the target halo is given by

$$F_{\nu}^{\text{ext}}(r) = F_{\nu}^{\text{ext}}(R_{*}) \left(\frac{D}{R_{*}} \right)^{-2} e^{-\tau_{\nu}(>r)} = \frac{L_{\nu}^{\text{ext}}}{4\pi D^2} e^{-\tau_{\nu}(>r)}, \quad (5.22)$$

where $F_{\nu}^{\text{ext}}(R_{*})$ is the flux at the surface of the source star, D is the distance from the source to the target, L_{ν}^{ext} is the luminosity of the source, and $\tau_{\nu}(>r)$ is the optical depth along the line of sight from radius r to the source (see Fig. [5.2]). A better tool for this geometry would be a 2-D azimuthal radiation-hydrodynamics code, but our code has the advantage that we can compute high-resolution problems in a relatively short computational time.

The photoionization and photodissociation coefficients are calculated in the same way as in the case of an internal point source (§5.2.4.1). The optical depth and column densities are now calculated outside-in, as described in Figure 5.2.

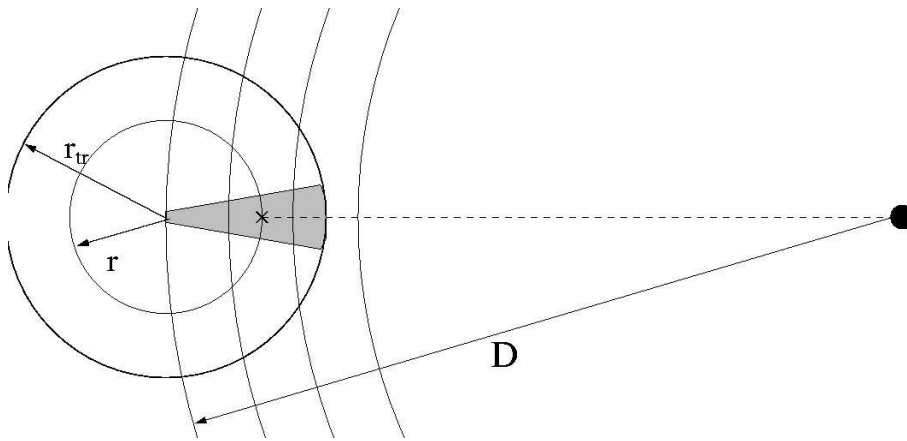


Figure 5.2: Schematic description of an external source illuminating a target halo at distance D . Geometrical dilution of the flux, if the size of the target halo is much smaller than D , is negligible across the target region, and the flux $F_\nu(r)$ can be approximated as $\frac{L_\nu}{4\pi D^2} e^{-\tau_\nu(>r)}$, where $\tau_\nu(>r)$ is the cumulative optical depth along the line of sight (dashed line) from radius r (point x) to the source (black solid circle on the right). r_{tr} is the truncation radius, or the outermost “edge” of the target halo.

5.2.5 Nonequilibrium chemistry

The abundance of different species changes due to ionization, recombination, dissociation, charge exchange, etc. The general rate equation for species i is given by

$$\frac{\partial n_i}{\partial t} = C_i(T, \{n_j\}) - D_i(T, \{n_j\})n_i, \quad (5.23)$$

where C_i is the collective source term for the creation of species i , and the second term is the collective “sink” term for the destruction of species i . We use the set of rate equations compiled by Abel et al. (1997).

We also adopt the rate solving scheme proposed by Abel et al. (1997). It is well known that coupled rate equations in the form of equation (5.23) are “stiff” differential equations, whose numerical solution suffers from instability if explicit ODE solvers are used. Abel et al. (1997) show that their implicit, backward difference scheme provides enough stability. Accuracy of the solution is achieved by updating each species in some specific order, rather than updating all species simultaneously from their values at the last time step. In addition, the abundance of the relatively fast reactions of H^- and H^+ are approximated by their equilibrium values, which are expressed by simple algebraic equations. See Appendix B for the corresponding finite-differencing scheme.

5.2.6 Code test

We tested our code against various problems which have analytic solutions. In most cases, such analytic solutions exist only for fine-tuned problems, such as a static, uniform medium (for ionization front propagation), power-law initial overdensity (for gravitational collapse), uniform density (for Sedov explosion), and so forth. There are hardly any test problems which included gravity, radiative transfer, chemistry and radiative transfer simultaneously.

We believe, therefore, that describing the results of all the test problems we did is not worthwhile. Instead, we simply list the test problems we did.

- Bertschinger solution (Bertschinger 1985): gravitational collapse of initially unperturbed fluid shells in an Einstein-de Sitter universe onto a seed mass, resulting in self-similar structure.
- Fillmore and Goldreich solution (Fillmore & Goldreich 1984): gravitational collapse of fluid shells, initially in a power-law overdensity, resulting in self-similar structure.
- Sedov explosion (Sedov 1959): hydrodynamic response of uniform density gas to a hot gas which is initially confined in a small region, resulting in self-similar structure.
- I-front propagation through a uniform, static medium: propagation of an I-front into a uniform, static medium, resulting in an analytical solution for the location of the I-front at time t .

- Franco et al. solution (Franco, Tenorio-Tagle, & Bodenheimer 1990): propagation of an I-front into a power-law density profile, resulting in an analytical similarity solution for the structure of the ionized region.

Our code passed all the tests described above with an acceptable accuracy.

5.3 Initial Setup

We now describe the initial setup for the problem of radiative feedback effects of Pop III stars on nearby halos at $z \approx 20$. We place a target halo of mass $M = 2 \cdot 10^5 M_\odot$ at five different locations from the source, with proper distance $D = \{180, 360, 540, 1000, 5000\}$ pc, which are all assumed to be affected directly by the radiation field from the source Pop III star of mass $M_* = 120 M_\odot$. We exposed the target halo to the radiation field for the lifetime of the star, $t_*(120 M_\odot) \simeq 2.5$ Myr (Schaerer 2002). The source Pop III star is assumed to be located in a halo of mass $M \simeq 10^6 M_\odot$. The initial time is set to zero: $t_{\text{ini}} = 0$.

This setup is well justified by the cosmological simulation result by Alvarez et al. (2005). By using the GADGET code that combines a tree, hierarchical gravity solver with the smoothed particle hydrodynamics (SPH) method, they simulated the high-redshift structure formation evolving both the dark matter and baryonic components to $z = 20$ from the Λ CDM initial condition at $z = 20$. They then placed a source at the location of the highest density SPH particle in the simulation box, which is located within a halo

of mass $M \simeq 10^6 M_\odot$. They find that, at the end of the lifetime of a star ($\sim [3 - 2] \text{ Myr}$) of mass $M \sim [80 - 200] M_\odot$, the star's HII region reaches a maximum size of radius about 5 kpc^2 (Fig. [8] of Alvarez et al. 2005).

We approximate the spectral energy distribution of the source star by a blackbody spectrum with the temperature given by Schaerer (2002). A Pop III star of mass $M_* \approx 120 M_\odot$, according to Schaerer (2002), has the time-average effective temperature $T_{\text{eff}} \approx 10^{4.981} \text{ K}$ and the luminosity $L = \int_0^\infty d\nu L_\nu \approx 10^{6.243} L_\odot$ with the lifetime $t_* \approx 2.5 \text{ Myr}$. We assume that the source radiates with these time-averaged values throughout its lifetime, then stops.

The target halo is assumed to be in a virial equilibrium, following the TIS model (Shapiro et al. 1999). The virial temperature of the TIS halo with mean molecular weight $\mu (=1.22 \text{ for neutral primordial gas})$ is given by

$$T = 593.5 \left(\frac{\mu}{1.22} \right) \left(\frac{\Omega_0}{0.27} \right)^{1/3} \left(\frac{h}{0.7} \right)^{2/3} \left(\frac{M}{2 \cdot 10^5 M_\odot} \right)^{2/3} \left(\frac{1+z}{1+20} \right) \text{ K}, \quad (5.24)$$

the truncation radius by

$$r_t = 102.3 \left(\frac{\Omega_0}{0.27} \right)^{-1/3} \left(\frac{h}{0.7} \right)^{-2/3} \left(\frac{M}{2 \cdot 10^5 M_\odot} \right) \left(\frac{1+z}{1+20} \right)^{-1} \text{ pc}, \quad (5.25)$$

and the central density by

$$\rho_0 = 4.144 \times 10^{-22} \left(\frac{\Omega_0}{0.27} \right) \left(\frac{h}{0.7} \right)^2 \left(\frac{1+z}{1+20} \right)^3 \text{ g cm}^{-3}, \quad (5.26)$$

²Note that target halos at larger distances from the source are affected by the source for less time, since the I-front reaches the target after a finite amount of time after the source starts to radiate. The intervening IGM can affect the original energy spectrum of the source, in general. We simply assume that the escape fraction of the source field out of the host halo is 1.

which can be expressed in terms of the hydrogen number density by

$$\begin{aligned}
n_{\text{H},0} &= \frac{X(\Omega_b/\Omega_0)\rho_0}{m_{\text{H}}} \\
&= 30 \left(\frac{X}{0.76} \right) \left(\frac{\Omega_b}{0.043} \right) \left(\frac{h}{0.7} \right)^2 \left(\frac{1+z}{1+20} \right)^3 \text{ cm}^{-3}, \quad (5.27)
\end{aligned}$$

where X is the hydrogen mass fraction in the baryon component. In the above expressions, fiducial values for our target halos have been used. Initial hydrostatic equilibrium is assumed for all baryonic and dark matter shells, balanced by the pressure gradient force and the self-gravity. The outermost shell is located at the TIS truncation radius r_t , where the local densities are $1/513$ of ρ_0 and $n_{\text{H},0}$. The initial abundances of atomic and molecular species are assumed to be equal to the abundances of an unperturbed primordial gas in a Λ CDM universe at $z = 20$. We adopt $x_{\text{He}} = 0.0789$, $x_e \simeq x_{\text{H}^+} = 6.73 \times 10^{-4}$, and $x_{\text{H}_2} = 2 \times 10^{-6}$ with the definition $x_i \equiv \frac{n_i}{n_{(\text{H})}}$, where $n_{(\text{H})}$ is the number density of the hydrogen nucleus (e.g. Dodelson 2003). The initial abundances of the other species are set to zero. We indeed find that the initial abundances of these neglected species are unimportant when we compare the corresponding results to those of the setup with a better approximation of primordial abundances of these species. They seem to approach their equilibrium values rather quickly. Even x_e and x_{H_2} deviate from these presumed values, because the density and the temperature environment of the halo itself is different from that of the unperturbed gas in the universe.

In practice, we use 1000 dark matter and fluid shells sampled uniformly (in radius) from the center to the truncation radius r_{tr} . We put a small reflect-

ing core at the center with negligible size, namely $r_{\text{core}} = 5 \times 10^{-4} r_{\text{tr}}$. Such a core is found to be useful in reducing undesirable numerical instability at the center. Our choice is conservative enough not to affect the overall answer.

5.4 Result

5.4.1 Optically thin limit: case study for initially ionized halo

Before describing the results of our full radiative transfer, hydrodynamics calculation, we describe an experiment for an artificial case where the target halo is assumed to be fully ionized in the beginning. Such a setup is equivalent to that of O’Shea et al. (2005), where they find that second-generation star formation is triggered by the cooling by H_2 : high residual electron fraction (due to the assumption of full ionization) allows quick formation of H_2 , which then cools the central region before it gains the escape velocity.

For this experiment, we have set $x_e = 1.14$, $x_{\text{HII}} = 1$, $x_{\text{HeI}} = 6.7 \times 10^{-6}$, $x_{\text{HeII}} = 8.86 \times 10^{-3}$, $x_{\text{HeIII}} = 6.98 \times 10^{-2}$, and assumed zero for other species. Without disturbing the TIS density profile, we also assigned a high temperature $T = 2 \times 10^4 \text{K}$. These values roughly mimic the condition found in typical HII regions where the neutral hydrogen and helium are ionized.

We indeed find that such an initial condition leads to the collapse of the core region due to newly formed H_2 , while the outskirts evaporate outward because gas gains escape velocity there from high pressure gradient. H_2 cooling and adiabatic cooling due to expansion in the outskirts do not reverse the evaporation process (Fig. [5.3]).

In the following sections, however, we will show that the initial condition of O’Shea et al. (2005) is never achieved when one considers the full radiative and hydrodynamic processes from the birth of a source star. We will also show that the formation of protostellar region in the target halo, if any, occurs in the neutral core region where the ionizing photons could not penetrate.

5.4.2 Feedback effect during the lifetime of the source

As described in §5.3, we expose target halos to the blackbody radiation field whose flux is attenuated by the geometrical factor $\left(\frac{D}{R_*}\right)^{-2}$ for different values of D . We denote each case by its distance in units of pc, as C180, C360, C540, C1000, and C5000, respectively. In order to approximate the effect of diffuse flux, we use the hydrogen case B recombination rate in all cases.

5.4.2.1 I-front trapping

We first find that the I-front is trapped well before reaching the halo center, when it makes the transition from a weak R-type (rarefied) I-front to a D-type (dense) front as it decelerates to about twice the sound speed of the ionized gas while climbing up the halo density profile. In all cases, a shock front precedes the I-front shortly after the I-front enters the halo, which occurs within a small fraction of the lifetime of a star. This indicates that the formation of a D-type I-front is a universal behavior for halos exposed to the ionizing radiation from nearby Pop III objects.

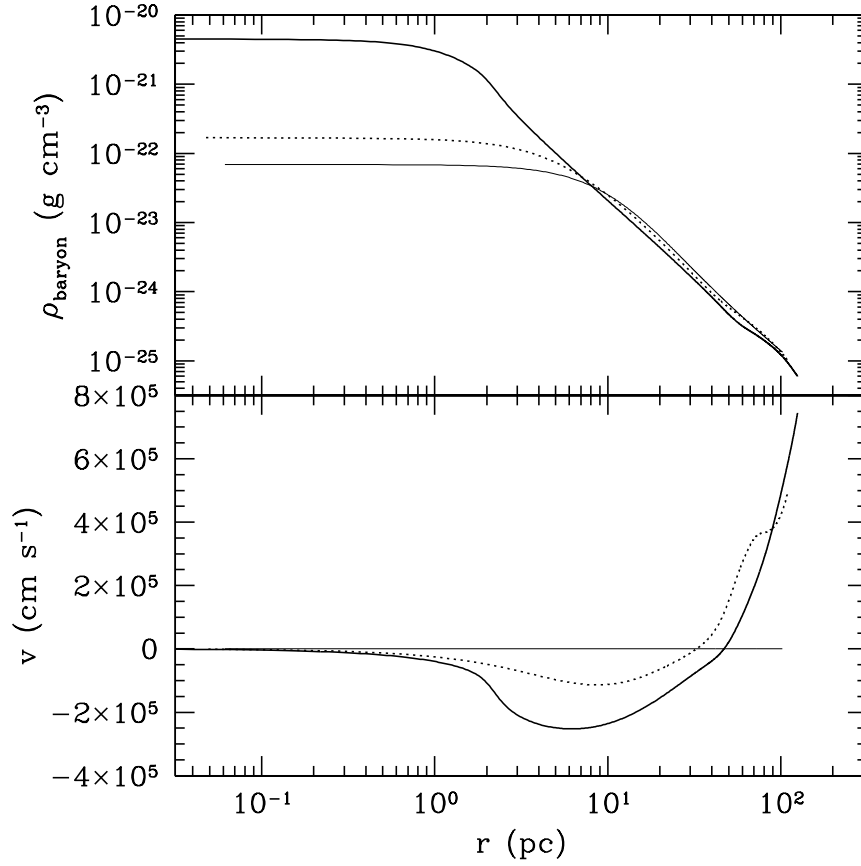


Figure 5.3: Radial profiles of density and velocity of an initially fully-ionized TIS halo at different times: $t = 0$ (thin solid), t_* (dotted) and $2t_*$ (thick solid).

This result agrees with the findings of Alvarez et al. (2005) qualitatively. One could roughly estimate the trapping radius and its corresponding local hydrogen number density with simple assumptions. As our initial setup is rather complicated, we simply quote the estimate by Alvarez et al. (2005) under the assumption of hydrogen-only gas, singular isothermal sphere profile, and the static limit:

$$\frac{r_{\text{trap}}}{r_{\text{vir}}} \approx 0.18 \left(\frac{M_{\text{vir}}}{2 \cdot 10^5 M_{\odot}} \right)^{1/9} \left(\frac{D}{220 \text{ pc}} \right)^{2/3} \left(\frac{\delta_{\text{vir}}}{200} \right)^{5/9} \left(\frac{Q_*}{1.4 \times 10^{50} \text{ s}^{-1}} \right)^{-1/3} \left(\frac{1+z}{1+20} \right)^{5/3}, \quad (5.28)$$

and

$$n_{\text{H,trap}} = 3.6 \text{ cm}^{-3} \left(\frac{M_{\text{vir}}}{2 \cdot 10^5 M_{\odot}} \right)^{-2/9} \left(\frac{D}{220 \text{ pc}} \right)^{-4/3} \left(\frac{\delta_{\text{vir}}}{200} \right)^{-1/9} \left(\frac{Q_*}{1.4 \times 10^{50} \text{ s}^{-1}} \right)^{2/3} \left(\frac{1+z}{1+20} \right)^{-1/3}. \quad (5.29)$$

In Figure 5.4 we plot the radial profiles of x_{H} at the end of the lifetime (t_*) of the star. We define the I-front position r_{I} as the location where $x_{\text{H}} = 0.5$ and across which the distinction of the prefront and postfront regions is evident.

5.4.2.2 Formation of the D-type I-front

The subsonic propagation of the I-front (i.e. subsonic relative to the sound speed of the ionized gas) is referred to as D-type (dense). In this case, as the gas is able to respond to the I-front hydrodynamically, a shock forms ahead of the I-front which compresses the gas so that the I-front speed drops

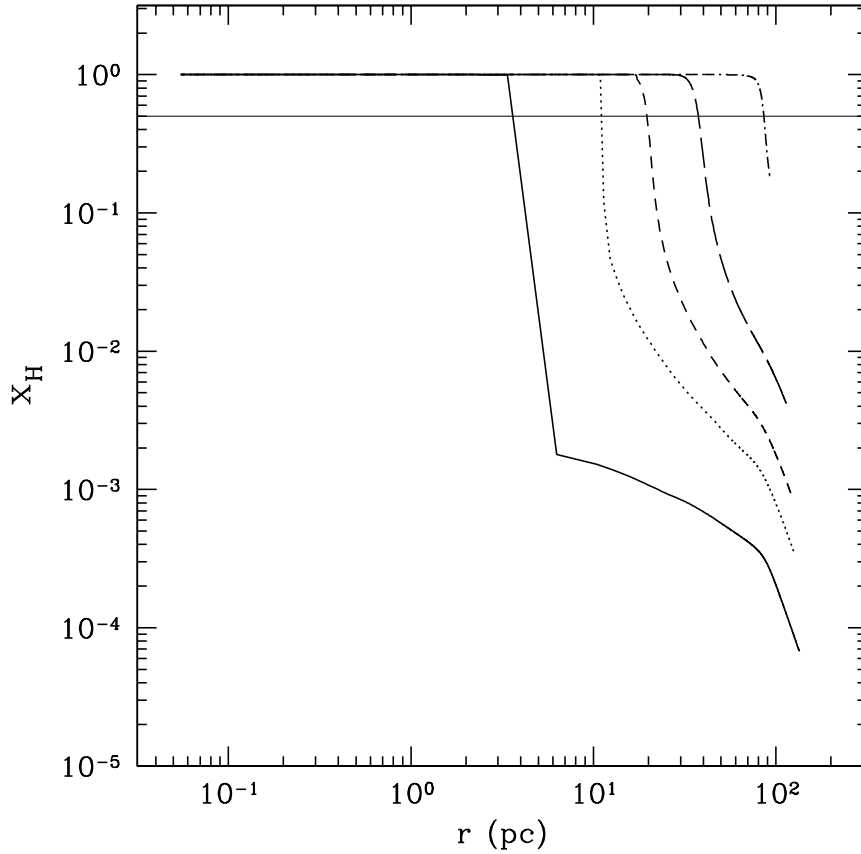


Figure 5.4: Radial profiles of x_{H} at time $t = t_* = 2.5 \text{ Myr}$, for C180 (solid), C360 (dotted), C540 (short-dashed), C1000 (long-dashed) and C5000 (dot-dashed). From this point on, we keep this definition of line types unless otherwise noted. The crossing point of each curve through the thin solid line defines the I-front, where $x_{\text{H}} = 0.5$.

from the R-critical speed to the D-critical speed and below. This D-critical I-front speed is given by

$$u_1 = u_D \equiv c_{1,2} - (c_{1,2}^2 - c_{1,1}^2)^{1/2} \approx \frac{c_{1,2}}{2} \left(\frac{c_{1,1}}{c_{1,2}} \right)^2 \ll c_{1,2}, \quad (5.30)$$

where subscript 1 denotes the pre-front properties, while 2 denotes the post-front (ionized side) properties. We find that D-type fronts are formed in the early stage of the lifetime of the star, soon after the I-front enters the target halo. After the onset of the D-type front, the I-front will remain as D-type because the density of the target halo increases as the I-front propagates toward the center of the halo.

We depict the density structure of target halos at $t = 0.5 t_*$ and at $t = t_*$ in Figures 5.5 and 5.6, respectively. A unique feature is observed just in front of the I-front, where unusually high density and low temperature are obtained (C180, C360, C540). We will investigate, in the following section, this feature in conjunction with the formation of a H_2 shell in front of the I-front.

5.4.2.3 Hydrogen Molecule Formation in Front of the I-Front

We find that a thin shell of H_2 is formed just ahead of the I-front, with peak abundance $x_{\text{H}_2} \approx 10^{-3}$. It happens mainly because the increased electron fraction across the I-front promotes the formation of H_2 . More precisely, the gas ahead of the I-front is ionized to the extent that the electron abundance is large enough to form H_2 , but at the same time too low to be considered as being ionized. Within the broader shell of shocked gas which precedes the

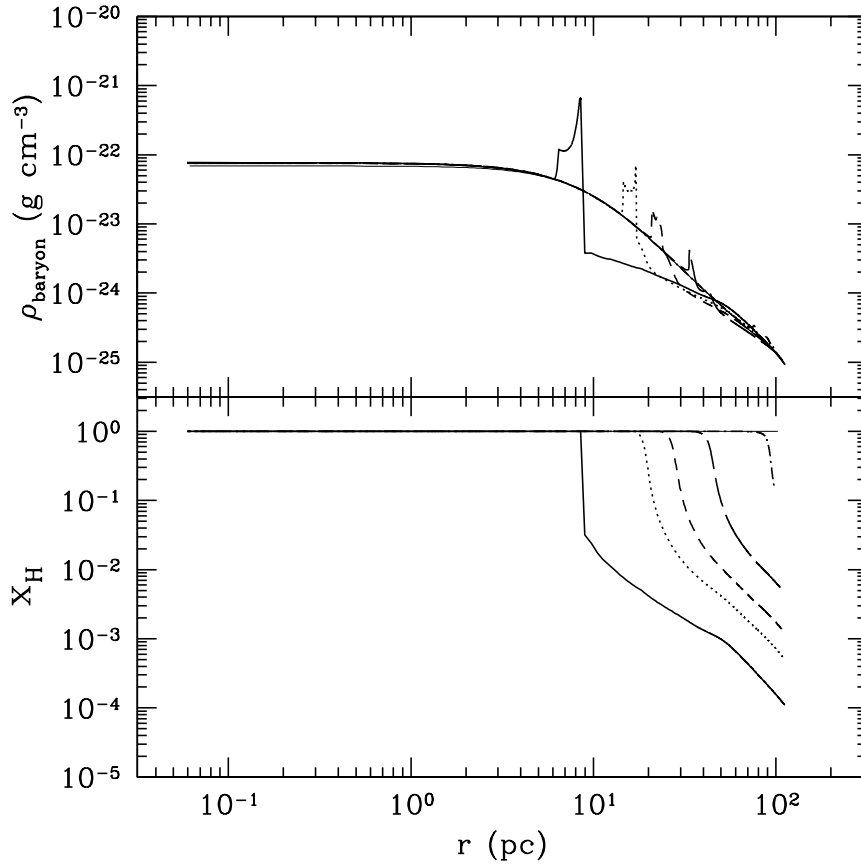


Figure 5.5: Radial profiles of the baryon mass density and the neutral hydrogen abundance at $t = 0.5 t_*$. The existence of the density “bump” ahead of the I-fronts clearly indicates that the I-fronts are D-type. Thin solid lines in both panels represent the initial value at time $t = 0$. Low density in the ionized region is caused by evaporation.

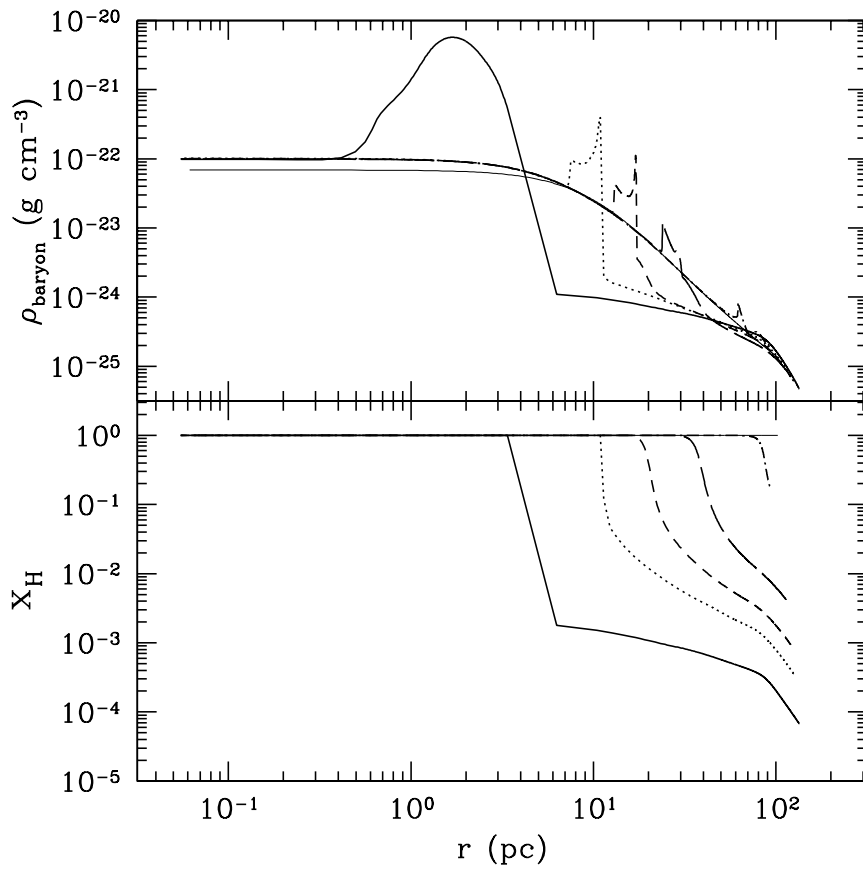


Figure 5.6: Same as Figure 5.5, but for $t = t_*$.

I-front, gas interior to this H₂ shell cannot see any ionizing photons, thus the low electron abundance quenches further formation of H₂ there. The width of this H₂ shell and the amount of H₂ in this region is determined by the hardness of the energy spectrum of the source: the width of the I-front is of the order of the mean free path of the ionizing photons. Pop III stars, in general, produce a large number of hard photons due to their high temperature, which can penetrate deeper into the neutral region than soft photons. We show the structure of these H₂ shells in Figure 5.7 and Figure 5.8. See, also, Figure 5.9, where we plot the radial profile of the abundance of different species for case C540 at $t = 0.5 t_*$. Also note the similarity between our results and the findings by Ricotti, Gnedin, & Shull (2001) for an I-front in the mean IGM (see Fig. [3] in Ricotti et al. 2001).

Existence of the H₂ shell might promote the formation of a collapsing protostellar region in various ways. A) The H₂ shell itself can be a site of star formation due to its cold temperature if it is gravitationally unstable, B) the H₂ shell may self-shield the inner region from dissociating photons, so H₂ formation and cooling may be enhanced in the halo central region, possibly leading to gravitational instability there, and C) gravitational collapse of this H₂ shell towards the center can boost the cooling of the inner region by increasing the density. The location of the H₂ shell may roughly mark the size of the protostellar region, inside of which H₂ is abundant enough to cool the gas and let it free-fall under gravity. The ionized region evaporates due to the boosted pressure gradient by the newly gained high temperature.

We note that H_2 shell indeed provides sufficient self-shielding effect as seen in Figure 5.10. H_2 column density (N_{H_2} changes abruptly across the H_2 shell, crossing the threshold value 10^{14}cm^{-2} for effective self-shielding (equ. [5.15]).

5.4.2.4 Fate of the Neutral Gas After Source Turns Off: Collapse of the Protostellar Region

As described in §5.4.2.3, the location of the H_2 shell roughly marks the size of the protostellar region. However, we need to quantify the protostellar region in a more consistent way. Toward this end, we simply take the Lagrangian radius at which the bulk velocity becomes negative first as the size of the collapsing protostellar region, as one travels along the radial direction outside-in at the end of the lifetime of the source³.

The time at onset of collapse is also an interesting quantity. It is, however, somewhat ambiguous to quantify this value. The usual condition $t_{\text{cool}} < t_{\text{free-fall}}$ may be used, but for simplicity, let us define the onset of the collapse as the time when any point inside the halo achieves a density which is 50 times its initial central value ($7 \times 10^{-23}\text{g cm}^{-3}$). While it might be more appropriate to use a condition based upon the average overdensity interior to

³Note that the neutral region inside the H_2 shell may not undergo a collapse even in the presence of the molecule shell. If the electron abundance in the target halo is much lower than the value we have used initially, $x_e \simeq 6.73 \times 10^{-4}$, the neutral region may not form enough H_2 to cool the gas there below the virial temperature. This may happen when the gas in the target halo recombines before sufficient H_2 formation occurs. One should, in principle, follow the formation history of the target halo from its linear regime in order to establish the structure and the chemical composition when the source turns on.

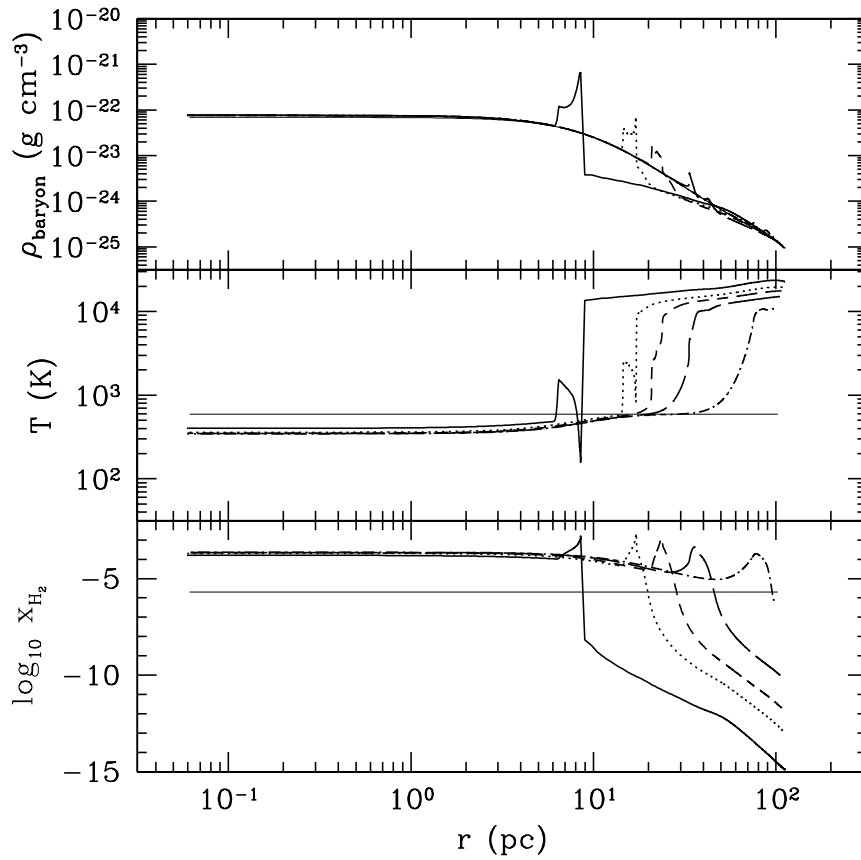


Figure 5.7: Radial profiles of density, temperature, and H_2 abundance at $t = 0.5 t_*$. Thin solid lines represent the initial value at $t = 0$. H_2 shell formation is universal in all cases.

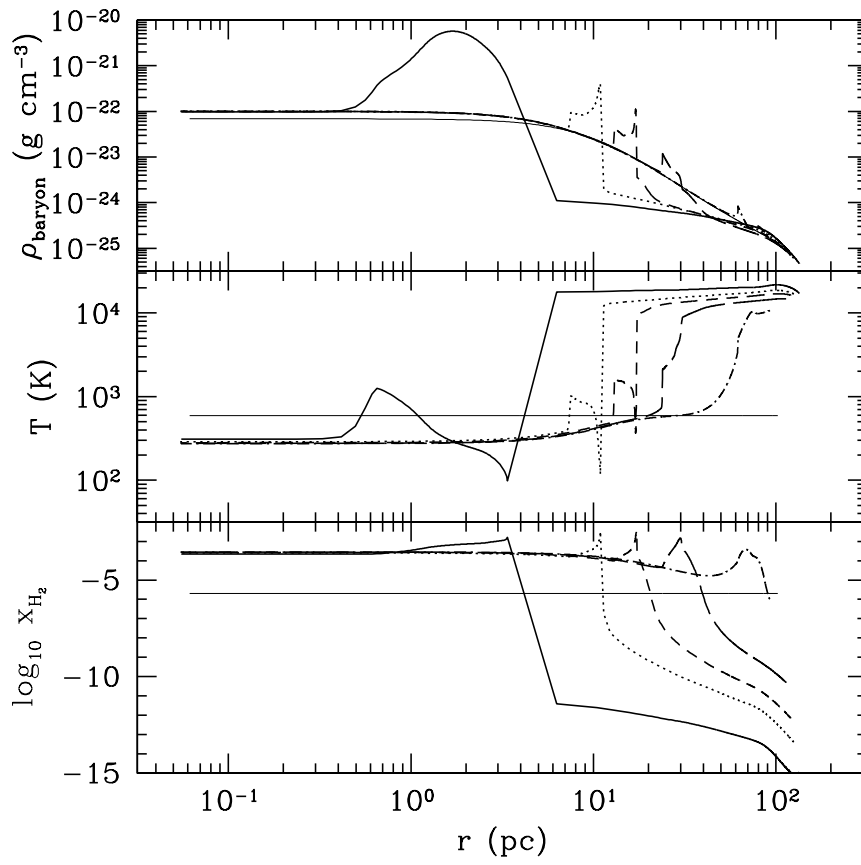


Figure 5.8: Same as figure 5.7, but for $t = t_*$.

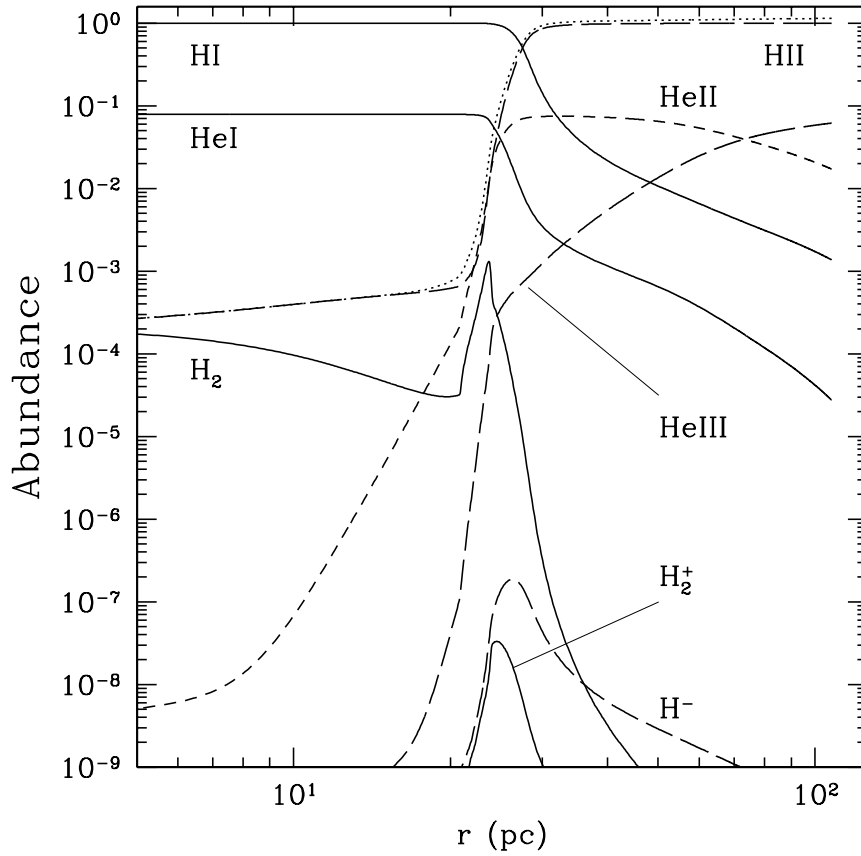


Figure 5.9: Radial profile of abundance of primordial gas species, for case C540 at $t = 0.5 t_*$. Labels are self-explanatory; electron abundance x_e is represented by the dotted curve, which closely follows the HIII abundance. The flux is coming from the right hand side, so this figure can be compared to the mirror image of Figure 3 in Ricotti et al. (2001).

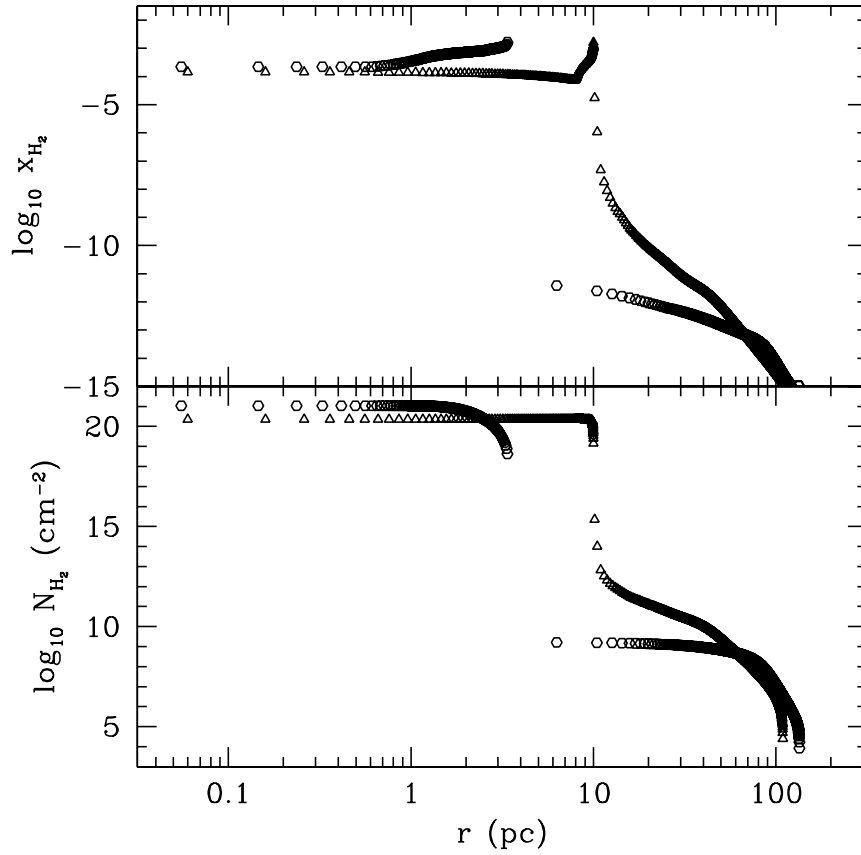


Figure 5.10: Radial profiles of molecule fraction (top) and the molecule column density (bottom) for case C180 at $t = 0.5 t_*$ (triangle) and at $t = t_*$ (hexagon).

radius r for any r , rather than this local overdensity, the answer, it turns out, is the same. Following this definition, we describe the structure of different cases at their onset of collapse in Figure 5.11. In case C180, collapse occurs just at the lifetime of the source, while in other cases collapse occurs after the lifetime. In the cases of C180, C360, C540 and C1000, the onset is earlier than that of a halo which is insulated from any radiation fields. Only in case C5000, the feedback effect is minimal, and the onset of collapse is closest to that of an insulated halo. A peculiar behavior of C5000 at its edge (Fig. [5.11]) is due to the fact that ionization is too weak to evaporate the edge of the halo. This “skin” then recombines to form an H_2 shell which freely collapses onto the inner region.

The hydrodynamic process in the core region seems to expedite the collapse process (Fig. [5.12]). When the shock-front from the D-type I-front propagates in, gas is compressed to higher density and temperature. In the presence of H_2 in the neutral region at a level $x_{\text{H}_2} \gtrsim 10^{-4}$, the gas can cool from the high temperature gained by the adiabatic compression. The thermal energy in the shocked gas will dissipate away by such cooling, then the shock front will fail to bounce off from the center to move the gas outward. Note, however, this process depends on $x_{\text{H}_2} \gtrsim 10^{-4}$. It is important, therefore, to establish the halo formation history to determine the structure and the chemical composition accurately. We will further investigate this issue in the future.

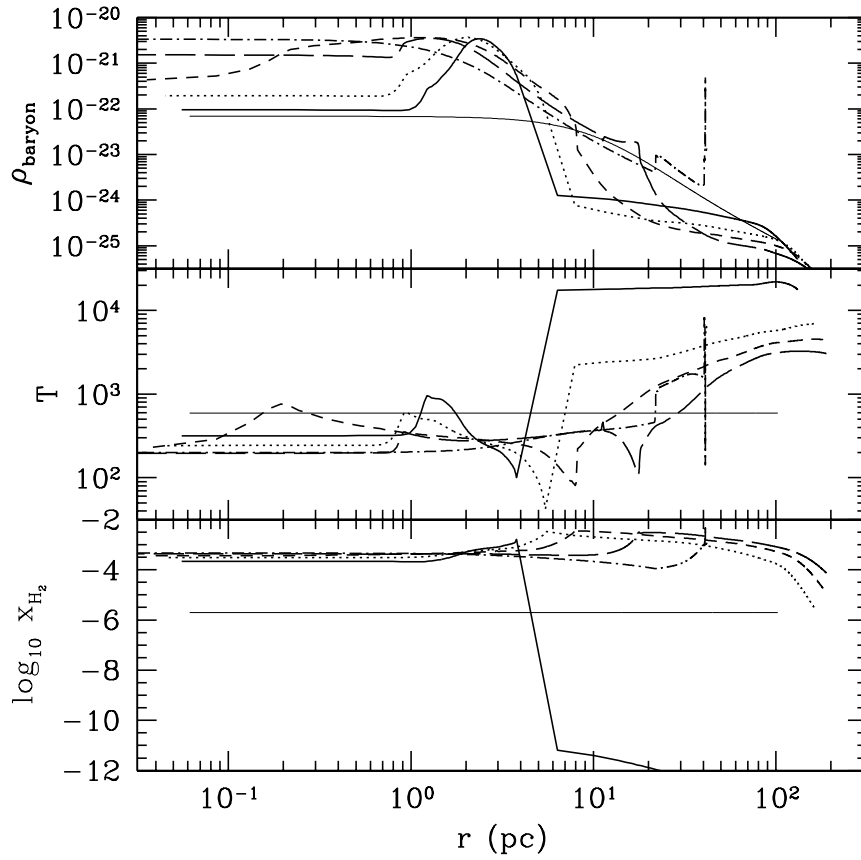


Figure 5.11: Structure of target halos at their onset of collapse, defined as the first moment when a certain point has reached $\rho_{\text{onset}} \equiv 50\rho_{0,\text{init}}$, where $\rho_{0,\text{init}}$ is the central density at $t = 0$.

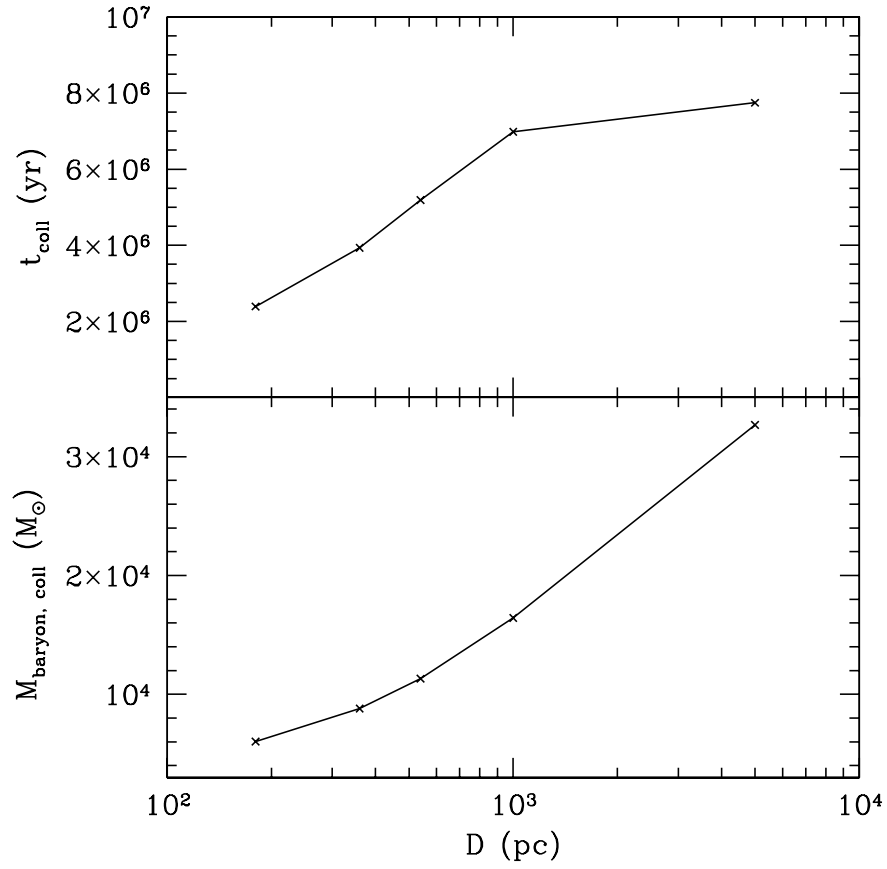


Figure 5.12: Onset of collapse (t_{coll}) and the net baryon mass collapsing ($M_{\text{baryon, coll}}$). Note that $t_* = 2.5 \text{ Myr}$ and $M_{\text{baryon, halo}} = 3.3 \times 10^4 M_{\odot}$.

5.4.3 Fate of the Ionized Gas After Source Turns Off: Evolution After Death of the Source

After death of the source, the ionized gas in target halos gradually recombines without further photo-ionization and dissociation. As discussed by Shapiro & Kang (1987), ionized, atomic gas of primordial composition cools radiatively faster than it recombines, and this nonequilibrium enhancement of the electron density as the temperature falls below 10^4K promotes H_2 formation and cooling. We find, however, that the ionized region keeps expanding outward, even though this nonequilibrium cooling and recombination effect boosts the H_2 abundance. This happens because the ionized gas easily gains an outward velocity which is larger than the escape velocity. This expulsion of the ionized gas outside the I-front is expected based upon studies by Shapiro, Iliev, & Raga (2004) of the photoevaporation of minihalos. Here we find that even after the source turns off, the exodus of the ionized layer continues while it cools and recombines. The neutral interior region, on the other hand, keeps collapsing inward supersonically. One can easily distinguish the collapsing region from the expanding region at this stage, because the contrast of these regions is amplified (Fig. [5.13]).

We could not continue to track the evolution of target halos after their central densities had reached $\sim 10^6$ times its initial value, because the computational time step became too small at this stage. We find that this stage occurs at roughly the same moment as the onset of collapse identified by our density compression criterion described in §5.4.2.4, as expected for supersonic

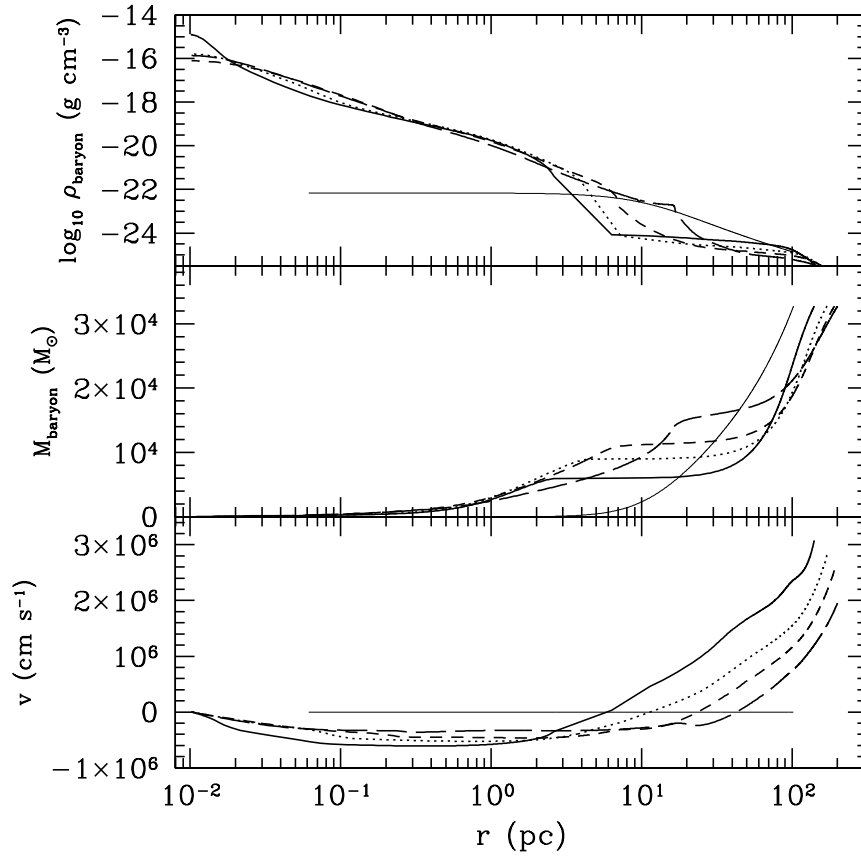


Figure 5.13: Structure of the target halo after the onset of collapse of the neutral core. It is clearly seen that the evaporating wind is detached from the collapsing core. Compare each case to the initial condition (thin solid line). Case C5000 is not plotted here, because the small time step due to the collapsing outer skin (Fig. [5.11]) prevented us from advancing the computation to the degree of central collapse shown in this figure.

infall.

The fate of this collapsing cloud is an interesting question to address. Rotational support, 3-D irregularity, and feedback effects from the second generation of stars would determine the fate of this collapsing region. We will explore this question further in the future.

We finally remark that neglect of HD processes in our calculation is justified *a posteriori* following our results. As noted above, the evaporating and expanding ionized gas is well separated from the collapsing H_2 region. As the collapsing H_2 region has never been fully ionized, the dominating mechanism for the thermal evolution of this region is H_2 chemistry, not HD, according to Johnson & Bromm (2005). The ionized region, on the other hand, may be able to recombine to form HD and cool down to the CMB temperature. However, as described above, because the bulk velocity of the baryonic component in this region exceeds the escape velocity, further cooling by HD would not affect our conclusion that the ionized region would not be able to form the second generation of stars, unless there exists a mechanism able to halt and revert this free expansion. Neglect of HD cooling is, therefore, well justified for our problem.

5.5 Discussion

We have developed a 1-D spherical, radiation-hydrodynamics code suitable for the study of the formation, evolution and feedback effects of nonlinear structures in the high redshift universe where baryonic matter has a primordial

composition. Our code solves the coupled equations of gravity, hydrodynamics, radiative transfer and primordial chemistry, with the ability to handle an internal point source, isotropic external source, and plane parallel external source.

We have used this code to study the hydrodynamic and radiative feedback effects of the first stars (i.e. Pop III stars) on their nearby minihalos. We chose a source star of mass $M_* = 120M_\odot$ embedded in a halo of mass $M = 10^6M_\odot$. We placed a target halo of $M = 2 \times 10^5M_\odot$, approximated by the TIS model, at different distances from the source star, all within HII region created by that star during its lifetime. In all cases, we approximated the incident flux as a plane-parallel wave attenuated by a geometrical factor $\left(\frac{D}{R_*}\right)^{-2}$ from the flux at the surface of the source, where D is the distance from the center of the target to the source, and R_* is the radius of the stellar surface.

We find that implosion (collapse) of the H_2 protostellar cloud occurs through various feedback effects. Because of the hardness of the energy spectrum of the Pop III star, a thin shell of H_2 forms ahead of the I-front, which self-shields the inner H_2 against the dissociating photons. The D-type I-front forms soon after the flux enters the target halo, and the shock-compressed gas propagates inward and becomes unstable in the presence of the intrinsic H_2 abundance. All these processes help to expedite the collapse of the region inside the H_2 shell. Onset of such collapse is faster for targets closer to the source. The mass of the collapsing region, on the other hand, is smaller for

closer targets, because a thicker ionized region is generated and is evaporated.

Our analysis has some caveats. Even though our calculation provides a firm intuitive basis for the feedback effects from the first stars, one should be careful in interpreting the results quantitatively. The assumed spherical symmetry is an obvious limitation, because the real I-front would form a parabolic shape inside target halos (see Shapiro et al. 2004). Hence, our analysis cannot be applied to regions other than the narrow cylindrical (conic, more exactly; see Fig. [5.2]) region along the straight line connecting the center of the target and the source star. The diffuse flux is treated only roughly, adopting the case B recombination rate for H. We have studied only a limited number of cases; to confirm its universality, we need to span a wider range of parameter space of the source mass, the target mass, and the distance. One could also question the initial setup we adopted. Halos form by cosmological mass infall and merger. The structure and chemical abundance of such halos might differ from our initial setup we used in our simulation. The impinging radiation could be substantially different from the assumed blackbody spectrum. The strength and effect of the isotropic background radiation are also uncertain. The direct hydrodynamic effect from the explosion of a star, if any, has not been considered either.

Despite these caveats, our analysis clearly indicates that “positive” feedback effects are very probable in (inner) source-free minihalos in the vicinity of Pop III stars. We have a robust result that a self-shielding H_2 shell forms ahead of the I-front. At this stage, the fate of the neutral region inside this

H_2 shell seems to depend upon the initial condition, especially the electron and the H_2 abundances. We will further explore this problem by spanning a broader parameter space and tracking the formation history of the target halo. The exact prediction of the subsequent star formation rate and its contribution to the cosmological reionization process is also an interesting subject. Further study is warranted.

Appendices

Appendix A

Mass - Wavenumber relation

We show how we got n_{eff} for different mass scales. It is slightly different from the usual way to obtain n_{eff} by differentiating the rms mass fluctuation, σ_M .

Typically, one has

$$n_{\text{eff}} = -3 \left(1 + \frac{d \ln \sigma_M^2}{d \ln M} \right) \quad (\text{A.1})$$

where

$$\sigma_M^2 \equiv \frac{\langle (m - M)^2 \rangle}{M^2} = \frac{1}{2\pi^2} \int_0^\infty P(k) W^2(kR) k^2 dk, \quad (\text{A.2})$$

where m is a mass enclosed by a sphere of radius R which also defines the *unperturbed* mass M through

$$M = \frac{4\pi}{3} R^3 \rho_0, \quad (\text{A.3})$$

where ρ_0 is the present matter density and the average $\langle \rangle$ is taken over all positions of the center of these spheres. This “top-hat” filtering results in a window function

$$W(X) = \frac{3}{X} (\sin(X) - X \cos(X)). \quad (\text{A.4})$$

It is then straightforward to calculate n_{eff} as a function of M using equation (A.1).

However, we are interested in the n_{eff} which is valid if one considers the initial average overdensity around density peaks, $\Delta_0(R)$ (HS). $\Delta_0(R)$ is given by

$$\Delta_0(R) \equiv \frac{\delta M}{M} = \frac{\delta_0}{\sigma^2} \frac{1}{2\pi^2} \int_0^\infty P(k)W(kR)k^2 dk, \quad (\text{A.5})$$

where M and $W(X)$ are defined by equation (A.3) and (A.4), respectively. From equation (A.3) and equation (A.5), we can see that for a power-law power spectrum $P(k) \propto k^n$,

$$\Delta_0(R) \propto R^{-(n+3)} \propto M^{-(n+3)/3}. \quad (\text{A.6})$$

Therefore, one can obtain n_{eff} as follows:

$$n_{\text{eff}} = -3 \left(1 + \frac{d \ln \Delta_0(M)}{d \ln M} \right). \quad (\text{A.7})$$

Appendix B

Finite Differencing in the 1-D Spherical, Radiation-Hydrodynamics Code

Here we describe the finite-difference scheme used for our 1-D spherical, radiation-hydrodynamics code. The subscript, unless noted otherwise, denotes the position of a shell. The superscript denotes the time. For instance, $\rho_{j+1/2}^{n+1}$ is the zone-centered density of shell $j+1$ at time t^{n+1} , and r_j^n is the zone-edge-centered radius of shell j at time t^n .

B.1 Time Steps

Time step for the finite-differencing is chosen such that important fluid variables do not change abruptly. The relevant time scales are the dynamical, sound-crossing (Courant), cooling(heating), and species-change time scales. In addition, to ensure that the fluid shells do not cross, we also adopt a shell-crossing time.

$$dt = \min\{dt_{\text{dyn}}, dt_{\text{Cour}}, dt_{\text{cool}}, dt_{\text{spec}}, dt_{\text{vel}}\} \quad (\text{B.1})$$

$$dt_{\text{dyn}} = \min \left\{ c_d \sqrt{\frac{\pi^2 r_i^3}{4m_i}} \right\}, \quad (\text{B.2})$$

$$dt_{\text{Cour}} = \min \left\{ c_C \left| \frac{r_i - r_{i-1}}{\sqrt{\gamma(\gamma - 1)u_i}} \right| \right\}, \quad (\text{B.3})$$

$$dt_{\text{cool}} = \min \left\{ c_c \left| \frac{u_i \rho_i}{(\Gamma - \Lambda)_i} \right| \right\}, \quad (\text{B.4})$$

$$dt_{\text{spec}} = \min \left\{ c_{\text{sp}} \left| \frac{x_{e,i}}{dx_{e,i}/dt} \right|, c_{\text{sp}} \left| \frac{x_{\text{HI},i}}{dx_{\text{HI},i}/dt} \right| \right\} \quad (\text{B.5})$$

$$dt_{\text{vel}} = \min \left\{ c_v \left| \frac{r_i - r_{i-1}}{v_i - v_{i-1}} \right| \right\}, \quad (\text{B.6})$$

where c_d , c_C , c_c , c_{sp} , and c_v are coefficients that ensure accurate calculation of the finite difference equations. We use $c_d = 0.1$, $c_C = 0.1$, $c_c = 0.1$, $c_{\text{sp}} = 0.1$, and $c_v = 0.05$.

B.2 Radiative Rate Coefficients

We first compute radiative rate coefficients k_i , where we use i to denote species. From this point on, the superscript “int” represents the internal source, and “ext” the outer source. For the radiation field generated from a point source at the center, the radiative rate coefficient of species i at radius r is given by

$$k_i(r) = \int_0^\infty d\nu \frac{\sigma_{i,\nu} F_\nu^{\text{int}}(r)}{h\nu}, \quad (\text{B.7})$$

where $F_\nu^{\text{int}}(r)$ is given by equation (5.13). Finite-differencing this rate coefficient, however, requires caution. For the baryonic shell at position j (smaller j means closer to the center) whose inner edge and outer edge have radii $r_{j-1/2}$ and $r_{j+1/2}$, respectively, the incident differential flux at the inner edge is $F_\nu^{\text{int}}(r_{j-1/2})$, and one could naively calculate the rate coefficient of species i

by

$$k_i(r_j) = \int_0^\infty d\nu \frac{\sigma_{i,\nu} F_\nu^{\text{int}}(r_{j-1/2})}{h\nu}. \quad (\text{B.8})$$

This expression, however, may not yield an accurate result when the a shell k is optically thick. In this case, F_ν may change substantially over the shell width, and equation (B.8) might overpredict the ionization rate by applying a constant flux over the shell width ($\Delta r_j \equiv r_{j+1/2} - r_{j-1/2}$). One may, in principle, choose to set up the initial condition such that all shells are optically thin. However, such a scheme can be very expensive computationally, especially when collapsed halos are treated. In order to resolve this problem, we use the “photon-conserving scheme” by Mellema et al. (2005). In this treatment, the number of photons that are absorbed in a shell is the same as the number of ionization events. Equation (B.8) can then be re-written as

$$\begin{aligned} k_i(r_j) &= \int_0^\infty d\nu \frac{L_\nu^{\text{int}}(r_{j-1/2}) - L_\nu^{\text{int}}(r_{j+1/2})}{h\nu} \cdot \frac{1}{n_i V_{\text{shell},j}} \\ &\simeq \int_0^\infty d\nu \frac{F_\nu^{\text{int}}(r_{j-1/2})}{h\nu} \cdot \frac{1 - e^{-\Delta\tau_{i,\nu}(r_j)}}{n_i \Delta r_j}, \end{aligned} \quad (\text{B.9})$$

where $L_\nu^{\text{int}}(r) = 4\pi r^2 F_\nu^{\text{int}}(r)$, $\Delta\tau_{i,\nu}(r_j) \equiv n_i \Delta r_j \sigma_{i,\nu}$ is the optical depth of a shell k on a species i , and $V_{\text{shell},j} \simeq 4\pi r_j^2 \Delta r_j$ is the volume of the shell. Note that when $\Delta\tau_\nu \ll 1$, equation (B.9) becomes equivalent to equation (B.8).

For the plane-parallel external source, the rate coefficients are obtained in the same way as for the internal point source, except that the relevant column densities for optical depth are now calculated outside-in, namely

$$\tau_\nu(r) = \tau_\nu(r) = \sum_i N_i(> r) \sigma_{i,\nu}, \quad (\text{B.10})$$

and that the flux is given by equation (5.22).

For the isotropic external source, in order to compute the radiative rate coefficients, we first need to calculate $J_\nu^{\text{ext}}(r_j)$, the mean intensity at the center of the shell j , by discrete summation over the angle θ . Kepner et al. (1997) sum each contribution from 20 different angles to achieve enough accuracy. We adopt a more efficient way: we calculate the integral (equ. [5.18]) by using the Gaussian quadrature method. An integral in the form $\int_{-1}^{+1} f(\mu)\mu$ can be evaluated via

$$\int_{-1}^{+1} f(\mu)d\mu = \sum_i^n \omega_i f(\mu_i), \quad (\text{B.11})$$

where μ_i is a designated evaluation point ($\cos\theta_i$ in our case), and ω_i is the “weight” of that point in the sum. The degree of accuracy of the Gaussian quadrature method with n selected points (μ_i ; “abscissa”) is about $2n$, roughly twice the degree of accuracy of simple polynomial methods (such as the Simpson’s rule). We choose $n = 7$, in which case the abscissae $\{\mu_i\}$ are 0, ± 0.405845 , and ± 0.741531 , while the corresponding weights $\{\omega_i\}$ are 0.417959, 0.381830, and 0.279705, respectively. Convergence has been tested by varying n , and we find that $n = 7$ is optimal for accuracy and efficiency. We point out that we do not use the photon-conserving scheme to calculate k_i (equ. [5.21]) for an isotropic external background. We found several complications related to the varying width Δ_{jjk} for different angles and to the way of weighting the photon consumption at each angle θ_k . At this stage, therefore, we simply calculate $k_i(r_j)$ by

$$k_i(r_j) = 4\pi \int_0^\infty \frac{\sigma_{i,\nu} J_\nu^{\text{ext}}(r_j)}{h\nu} d\nu, \quad (\text{B.12})$$

where the mean intensity $J_\nu^{\text{ext}}(r_j)$, as mentioned above, is calculated by

$$J_\nu^{\text{ext}}(r_j) = \frac{1}{2} J_\nu(r_{\text{halo}}) \sum_i^7 \omega_i \exp[-\tau_\nu(r_j, \mu_i)]. \quad (\text{B.13})$$

Finally, the self-shielding of H_2 and the photodissociation coefficient are calculated using the shielding function of Draine & Bertoldi (1996), through

$$k_{\text{H}_2}(r_j) = 1.38 \times 10^9 (J_\nu^{\text{ext}}(r_j))_{h\nu=12.87\text{eV}} F_{\text{shield}}(r_j), \quad (\text{B.14})$$

where $F_{\text{shield}}(r)$ is now an angle-averaged quantity, given by

$$F_{\text{shield}}(r_j) = \frac{1}{2} \int_{-1}^{+1} F_{\text{shield}}(r_j, \mu) d\mu \approx \frac{1}{2} \sum_i^7 \omega_i F_{\text{shield}}(r_j, \mu_i). \quad (\text{B.15})$$

$F_{\text{shield}}(r_j, \mu_i)$ is given by equation (5.15), where N_{H_2} , in this case, is the H_2 column density along the line of sight of angle θ_i (see Fig. [5.1]).

B.3 Nonequilibrium Chemistry

As described in § 5.2.5, in order to update the abundance of species i , we adopt the finite difference scheme by Abel et al. (1997). Based upon equation (5.23), each species i is updated by

$$n_j^{n+1} = \frac{C_i^{n+1}(T, \{n_j\}) dt^{n+1/2} + n_j^n}{1 + D_i^{n+1}(T, \{n_j\}) dt^{n+1/2}}, \quad (\text{B.16})$$

where the species $\{n_j\}$ is the previously updated value in the order given by Abel et al. (1997) (note that the letter n ($n + 1/2$, $n + 1$) in subscript denotes the time t^n ($t^{n+1/2}$, t^{n+1}). The order they find to be optimal is H, H^+ , He, He^+ , He^{++} and e^- , followed by the algebraic equilibrium expressions for H^- and H^+ , and finally H_2 , again by equation (B.16).

B.4 Heating/Cooling and Hydrodynamics

Hydrodynamic conservation equations for the baryonic component (eqs. [5.1] - [5.3]) are solved following the finite-difference scheme by Thoul & Weinberg (1995). We first update the velocity and position using the so-called “leap-frog” scheme, so that the velocity and the position are staggered in time:

$$v_j^{n+1/2} = v_j^{n-1/2} - \left[4\pi(r_j^n)^2 \frac{p_{j+1/2}^n - p_{j-1/2}^n}{dm_j} + \frac{m_j^n}{(r_j^n)^2} \right] dt^n, \quad (\text{B.17})$$

and

$$r_j^{n+1} = r_j^n + v_j^{n+1/2} dt^{n+1/2}, \quad (\text{B.18})$$

which are second-order accurate. As the mass of each shell is conserved for such a Lagrangian scheme, density is updated following

$$\rho_{j+1/2}^{n+1} = \frac{dm_{j+1/2}}{(4/3)\pi[(r_{j+1}^{n+1})^3 - (r_j^{n+1})^3]}. \quad (\text{B.19})$$

In these equations,

$$dt^n = \frac{1}{2}(dt^{n-1/2} + dt^{n+1/2}), \quad (\text{B.20})$$

and

$$dm_j = \frac{1}{2}(dm_{j-1/2} + dm_{j+1/2}). \quad (\text{B.21})$$

We then advance the energy by

$$e_{i+1/2}^{n+1} = e_{i+1/2}^n - p_{i+1/2}^n \left(\frac{1}{\rho_{i+1/2}^{n+1}} - \frac{1}{\rho_{i+1/2}^n} \right) + \frac{(\Gamma - \Lambda)_{i+1/2}^n}{\rho_{i+1/2}^{n+1}} dt^{n+1/2}. \quad (\text{B.22})$$

Shocks are treated with the usual artificial viscosity technique. The pressure in the momentum and energy conservation equations is replaced by $P = p + q$, where

$$q_{i+1/2}^{n+1} = -c_q \frac{2}{1/\rho_{i+1/2}^{n+1} - 1/\rho_{i+1/2}^n} \left| v_{i+1}^{n+1/2} - v_i^{n+1/2} \right| \times (v_{i+1}^{n+1/2} - v_i^{n+1/2}), \quad (\text{B.23})$$

if $v_{i+1}^{n+1/2} - v_i^{n+1/2} < 0$, and $q = 0$ otherwise. We use $c_q = 4$, which spreads the shock fronts over four or five cells.

Dark matter shells are also updated according to equations (B.17) - (B.23), except that the heating/cooling term is zero in equation (B.22). This treatment is based upon the fluid approximation for dark matter dynamics described in § 2.2, and is different from the radial-shell scheme used by Thoul & Weinberg (1995). Note that the dark matter shells are allowed to have effective shock in our fluid approximation, and therefore we need to compute the artificial viscosity when dark matter shells are converging (equ. [B.23]), as in the case of the baryonic gas component.

Bibliography

- Abadi, M. G., Bower, R. G., & Navarro, J. F. 2000, *Mon. Not. R. Astron. Soc.* , 314, 759
- Abel, T., Anninos, P., Zhang, Y., & Norman, M. L. 1997, *New Astronomy*, 2, 181
- Abel, T., Bryan, G. L., & Norman, M. L. 2000, *Astrophys. J.* , 540, 39
— 2002, *Science*, 295, 93
- Ahn, K., & Komatsu, E. 2005, *Phys. Rev. D* , 71, 021303
- Ahn, K., Komatsu, E., & Höflich, P. 2005, *Phys. Rev. D* , 71, 121301
- Alvarez, M. A., Ahn, K., & Shapiro, P. R. 2003, in *Revista Mexicana de Astronomia y Astrofisica Conf. Ser.*, 4
- Alvarez, M. A., Bromm, V., & Shapiro, P. R. 2005, *ArXiv Astrophysics e-prints*. [arXiv:astro-ph/0507684](https://arxiv.org/abs/astro-ph/0507684)
- Anninos, P., Zhang, Y., Abel, T., & Norman, M. L. 1997, *New Astronomy*, 2, 209
- Ascasibar, Y., Jean, P., Boehm, C., & Knoedlseder, J. 2005, *ArXiv Astrophysics e-prints*. [arXiv:astro-ph/0507142](https://arxiv.org/abs/astro-ph/0507142)

- Balberg, S., & Shapiro, S. L. 2002, *Phys. Rev. Lett.* , 88, 101301
- Balberg, S., Shapiro, S. L., & Inagaki, S. 2002, *Astrophys. J.* , 568, 475
- Bardeen, J. M., Bond, J. R., Kaiser, N., & Szalay, A. S. 1986, *Astrophys. J.* , 304, 15
- Barkana, R., & Loeb, A. 2004, *Astrophys. J.* , 609, 474
- Barnes, J., & Efstathiou, G. 1987, *Astrophys. J.* , 319, 575
- Beacom, J. F., Bell, N. F., & Bertone, G. 2005, *Phys. Rev. Lett.* , 94, 171301
- Berends, F. A., & Bohm, A. 1998, in High Energy Electron-Positron Physics, edited by A. Ali and P. Soding
- Bergström, L., Bringmann, T., Eriksson, M., & Gustafsson, M. 2005, *Phys. Rev. Lett.* , 94, 131301
- Bertschinger, E. 1985, *Astrophys. J. Suppl. Ser.* , 58, 39
- 1998, *Ann. Rev. Astron. Astrophys.* , 36, 599
- Bettwieser, E. 1983, *Mon. Not. R. Astron. Soc.* , 203, 811
- Bharadwaj, S., & Ali, S. S. 2004, *Mon. Not. R. Astron. Soc.* , 352, 142
- Binney, J., & Tremaine, S. 1987, Galactic dynamics (Princeton, NJ, Princeton University Press, 1987, 747 p.)

- Binney, J. J., & Evans, N. W. 2001, *Mon. Not. R. Astron. Soc.* , 327, L27
- Boehm, C., & Ascasibar, Y. 2004, *Phys. Rev. D* , 70, 115013
- Boehm, C., Enßlin, T. A., & Silk, J. 2004a, *Journal of Physics G Nuclear Physics*, 30, 279
- Boehm, C., Hooper, D., Silk, J., Casse, M., & Paul, J. 2004b, *Phys. Rev. Lett.* , 92, 101301
- Bromm, V., Coppi, P. S., & Larson, R. B. 1999, *Astrophys. J. Lett.* , 527, L5
- 2002, *Astrophys. J.* , 564, 23
- Bromm, V., Kudritzki, R. P., & Loeb, A. 2001, *Astrophys. J.* , 552, 464
- Bullock, J. S., Dekel, A., Kolatt, T. S., Kravtsov, A. V., Klypin, A. A., Porciani, C., & Primack, J. R. 2001a, *Astrophys. J.* , 555, 240
- Bullock, J. S., Kolatt, T. S., Sigad, Y., Somerville, R. S., Kravtsov, A. V., Klypin, A. A., Primack, J. R., & Dekel, A. 2001b, *Mon. Not. R. Astron. Soc.* , 321, 559
- Burkert, A. 1995, *Astrophys. J. Lett.* , 447, L25
- 2000, *Astrophys. J. Lett.* , 534, L143
- Carilli, C. L., Gnedin, N. Y., & Owen, F. 2002, *Astrophys. J.* , 577, 22

- Carlberg, R. G., Yee, H. K. C., Ellingson, E., Morris, S. L., Abraham, R., Gravel, P., Pritchett, C. J., Smecker-Hane, T., Hartwick, F. D. A., Hesser, J. E., Hutchings, J. B., & Oke, J. B. 1997, *Astrophys. J. Lett.* , 485, L13
- Churazov, E., Sunyaev, R., Sazonov, S., Revnivtsev, M., & Varshalovich, D. 2005, *Mon. Not. R. Astron. Soc.* , 357, 1377
- Ciardi, B., Ferrara, A., & Abel, T. 2000, *Astrophys. J.* , 533, 594
- Ciardi, B., & Madau, P. 2003, *Astrophys. J.* , 596, 1
- Clayton, D. D., & Ward, R. A. 1975, *Astrophys. J.* , 198, 241
- Colín, P., Avila-Reese, V., Valenzuela, O., & Firmani, C. 2002, *Astrophys. J.* , 581, 777
- Colín, P., Klypin, A., Valenzuela, O., & Gottlöber, S. 2004, *Astrophys. J.* , 612, 50
- Colín, P., Klypin, A. A., & Kravtsov, A. V. 2000, *Astrophys. J.* , 539, 561
- Comastri, A., Setti, G., Zamorani, G., & Hasinger, G. 1995, *Astron. Astrophys.* , 296, 1
- Crittenden, R. R., Walker, W. D., & Ballam, J. 1961, *Physical Review*, 121, 1823

- Czoske, O., Moore, B., Kneib, J.-P., & Soucail, G. 2002, *Astron. Astrophys.* , 386, 31
- Dalal, N., & Kochanek, C. S. 2002, *Astrophys. J.* , 572, 25
- Davé, R., Spergel, D. N., Steinhardt, P. J., & Wandelt, B. D. 2001, *Astrophys. J.* , 547, 574
- Davis, M., Efstathiou, G., Frenk, C. S., & White, S. D. M. 1985, *Astrophys. J.* , 292, 371
- de Blok, W. J. G., & Bosma, A. 2002, *Astron. Astrophys.* , 385, 816
- de Blok, W. J. G., McGaugh, S. S., Bosma, A., & Rubin, V. C. 2001, *Astrophys. J. Lett.* , 552, L23
- Diemand, J., Moore, B., & Stadel, J. 2004, *Mon. Not. R. Astron. Soc.* , 353, 624
- Dodelson, S. 2003, *Modern cosmology* (Modern cosmology / Scott Dodelson. Amsterdam (Netherlands): Academic Press. ISBN 0-12-219141-2, 2003, XIII + 440 p.)
- Draine, B. T., & Bertoldi, F. 1996, *Astrophys. J.* , 468, 269
- Eke, V. R., Navarro, J. F., & Frenk, C. S. 1998, *Astrophys. J.* , 503, 569
- El-Zant, A., Shlosman, I., & Hoffman, Y. 2001, *Astrophys. J.* , 560, 636

- El-Zant, A. A., Hoffman, Y., Primack, J., Combes, F., & Shlosman, I. 2004, *Astrophys. J. Lett.* , 607, L75
- Field, G. B. 1959, *Astrophys. J.* , 129, 536
- Fillmore, J. A., & Goldreich, P. 1984, *Astrophys. J.* , 281, 1
- Flores, R. A., & Primack, J. R. 1994, *Astrophys. J. Lett.* , 427, L1
- Franco, J., Tenorio-Tagle, G., & Bodenheimer, P. 1990, *Astrophys. J.* , 349, 126
- Frenk, C. S., White, S. D. M., Bode, P., Bond, J. R., Bryan, G. L., Cen, R., Couchman, H. M. P., Evrard, A. E., Gnedin, N., Jenkins, A., Khokhlov, A. M., Klypin, A., Navarro, J. F., Norman, M. L., Ostriker, J. P., Owen, J. M., Pearce, F. R., Pen, U.-L., Steinmetz, M., Thomas, P. A., Villumsen, J. V., Wadsley, J. W., Warren, M. S., Xu, G., & Yepes, G. 1999, *Astrophys. J.* , 525, 554
- Fukushige, T., Kawai, A., & Makino, J. 2004, *Astrophys. J.* , 606, 625
- Fukushige, T., & Makino, J. 2001, *Astrophys. J.* , 557, 533
- 2003, *Astrophys. J.* , 588, 674
- Furlanetto, S. R., & Loeb, A. 2002a, *Astrophys. J.* , 565, 854
- 2002b, *Astrophys. J.* , 579, 1
- 2004, *Astrophys. J.* , 611, 642

- Furlanetto, S. R., Sokasian, A., & Hernquist, L. 2004, *Mon. Not. R. Astron. Soc.* , 347, 187
- Gavazzi, R., Fort, B., Mellier, Y., Pelló, R., & Dantel-Fort, M. 2003, *Astron. Astrophys.* , 403, 11
- Glover, S. C. O., & Brand, P. W. J. L. 2001, *Mon. Not. R. Astron. Soc.* , 321, 385
- 2003, *Mon. Not. R. Astron. Soc.* , 340, 210
- Gnedin, N. Y., & Shaver, P. A. 2004, *Astrophys. J.* , 608, 611
- Gnedin, O. Y., & Ostriker, J. P. 2001, *Astrophys. J.* , 561, 61
- Griffiths, R. E., Casertano, S., Im, M., & Ratnatunga, K. U. 1996, *Mon. Not. R. Astron. Soc.* , 282, 1159
- Gruber, D. E., Matteson, J. L., Peterson, L. E., & Jung, G. V. 1999, *Astrophys. J.* , 520, 124
- Haiman, Z., Abel, T., & Rees, M. J. 2000, *Astrophys. J.* , 534, 11
- Haiman, Z., Rees, M. J., & Loeb, A. 1996, *Astrophys. J.* , 467, 522
- 1997, *Astrophys. J.* , 476, 458
- Hayashi, E., Navarro, J. F., Power, C., Jenkins, A., Frenk, C. S., White, S. D. M., Springel, V., Stadel, J., & Quinn, T. R. 2004, *Mon. Not. R. Astron. Soc.* , 355, 794

- Hennawi, J. F., & Ostriker, J. P. 2002, *Astrophys. J.* , 572, 41
- Hernquist, L. 1990, *Astrophys. J.* , 356, 359
- Hoffman, Y., & Shaham, J. 1985, *Astrophys. J.* , 297, 16
- Holley-Bockelmann, K., Weinberg, M., & Katz, N. 2003, ArXiv Astrophysics e-prints. [arXiv:astro-ph/0306374](https://arxiv.org/abs/astro-ph/0306374)
- Hooper, D., Ferrer, F., Boehm, C., Silk, J., Paul, J., Evans, N. W., & Casse, M. 2004, *Phys. Rev. Lett.* , 93, 161302
- Iliev, I. T., Scannapieco, E., Martel, H., & Shapiro, P. R. 2003, *Mon. Not. R. Astron. Soc.* , 341, 81
- Iliev, I. T., & Shapiro, P. R. 2001, *Mon. Not. R. Astron. Soc.* , 325, 468
- Iliev, I. T., Shapiro, P. R., Ferrara, A., & Martel, H. 2002, *Astrophys. J. Lett.* , 572, L123
- Jean, P., Knödseder, J., Lonjou, V., Allain, M., Roques, J.-P., Skinner, G. K., Teegarden, B. J., Vedrenne, G., von Ballmoos, P., Cordier, B., Caraveo, P., Diehl, R., Durouchoux, P., Mandrou, P., Matteson, J., Gehrels, N., Schönfelder, V., Strong, A. W., Ubertini, P., Weidenspointner, G., & Winkler, C. 2003, *Astron. Astrophys.* , 407, L55
- Jing, Y. P., & Suto, Y. 2000, *Astrophys. J. Lett.* , 529, L69
- 2002, *Astrophys. J.* , 574, 538

Johnson, J. L., & Bromm, V. 2005, ArXiv Astrophysics e-prints. [arXiv: astro-ph/0505304](https://arxiv.org/abs/astro-ph/0505304)

Kappadath, S. C., Ryan, J., Bennett, K., Bloemen, H., Forrest, D., Hermsen, W., Kippen, R. M., McConnell, M., Schoenfelder, V., van Dijk, R., Varendorff, M., Weidenspointner, G., & Winkler, C. 1996, *Astron. Astrophys. Suppl. Ser.* , 120, C619+

Keeton, C. R., Gaudi, B. S., & Petters, A. O. 2003, *Astrophys. J.* , 598, 138

Kepner, J. V., Babul, A., & Spergel, D. N. 1997, *Astrophys. J.* , 487, 61

Kinzer, R. L., Milne, P. A., Kurfess, J. D., Strickman, M. S., Johnson, W. N., & Purcell, W. R. 2001, *Astrophys. J.* , 559, 282

Kitayama, T., Susa, H., Umemura, M., & Ikeuchi, S. 2001, *Mon. Not. R. Astron. Soc.* , 326, 1353

Kitayama, T., Yoshida, N., Susa, H., & Umemura, M. 2004, *Astrophys. J.* , 613, 631

Klypin, A., Kravtsov, A. V., Bullock, J. S., & Primack, J. R. 2001, *Astrophys. J.* , 554, 903

Klypin, A., Kravtsov, A. V., Valenzuela, O., & Prada, F. 1999, *Astrophys. J.* , 522, 82

Klypin, A., Zhao, H., & Somerville, R. S. 2002, *Astrophys. J.* , 573, 597

- Knödlseher, J., Lonjou, V., Jean, P., Allain, M., Mandrou, P., Roques, J.-P., Skinner, G. K., Vedrenne, G., von Ballmoos, P., Weidenspointner, G., Caraveo, P., Cordier, B., Schönfelder, V., & Teegarden, B. J. 2003, *Astron. Astrophys.* , 411, L457
- Kochanek, C. S., & White, M. 2001, *Astrophys. J.* , 559, 531
- Kogut, A., Spergel, D. N., Barnes, C., Bennett, C. L., Halpern, M., Hinshaw, G., Jarosik, N., Limon, M., Meyer, S. S., Page, L., Tucker, G. S., Wollack, E., & Wright, E. L. 2003, *Astrophys. J. Suppl. Ser.* , 148, 161
- Larson, R. B. 1970, *Mon. Not. R. Astron. Soc.* , 147, 323
- Lepp, S., & Shull, J. M. 1984, *Astrophys. J.* , 280, 465
- Lynden-Bell, D., & Eggleton, P. P. 1980, *Mon. Not. R. Astron. Soc.* , 191, 483
- Ma, C., & Bertschinger, E. 1995, *Astrophys. J.* , 455, 7
- Machacek, M. E., Bryan, G. L., & Abel, T. 2001, *Astrophys. J.* , 548, 509
- Madau, P., Meiksin, A., & Rees, M. J. 1997, *Astrophys. J.* , 475, 429
- Mao, S., Jing, Y., Ostriker, J. P., & Weller, J. 2004, *Astrophys. J. Lett.* , 604, L5

- Marchesini, D., D’Onghia, E., Chincarini, G., Firmani, C., Conconi, P., Molinari, E., & Zacchei, A. 2002, *Astrophys. J.* , 575, 801
- Martyn, H. U. 1990, in Quantum Electrodynamics, edited by T. Kinoshita
- Mellema, G., Iliev, I., Alvarez, M., & Shapiro, P. R. 2005, Submitted to New Astronomy
- Metcalf, R. B. 2005, *Astrophys. J.* , 622, 72
- Metcalf, R. B., & Zhao, H. 2002, *Astrophys. J. Lett.* , 567, L5
- Moore, B. 1994, *Nature* , 370, 629
- 2001, in AIP Conf. Proc. 586: 20th Texas Symposium on relativistic astrophysics, 73
- Moore, B., Gelato, S., Jenkins, A., Pearce, F. R., & Quilis, V. 2000, *Astrophys. J. Lett.* , 535, L21
- Moore, B., Ghigna, S., Governato, F., Lake, G., Quinn, T., Stadel, J., & Tozzi, P. 1999a, *Astrophys. J. Lett.* , 524, L19
- Moore, B., Governato, F., Quinn, T., Stadel, J., & Lake, G. 1998, *Astrophys. J. Lett.* , 499, L5
- Moore, B., Quinn, T., Governato, F., Stadel, J., & Lake, G. 1999b, *Mon. Not. R. Astron. Soc.* , 310, 1147

- Nakamura, F., & Umemura, M. 2001, *Astrophys. J.* , 548, 19
- Natarajan, P., Loeb, A., Kneib, J., & Smail, I. 2002, *Astrophys. J. Lett.* , 580, L17
- Navarro, J. F., Eke, V. R., & Frenk, C. S. 1996, *Mon. Not. R. Astron. Soc.* , 283, L72
- Navarro, J. F., Frenk, C. S., & White, S. D. M. 1997, *Astrophys. J.* , 490, 493
- Navarro, J. F., Hayashi, E., Power, C., Jenkins, A. R., Frenk, C. S., White, S. D. M., Springel, V., Stadel, J., & Quinn, T. R. 2004, *Mon. Not. R. Astron. Soc.* , 349, 1039
- Nusser, A., & Sheth, R. K. 1999, *Mon. Not. R. Astron. Soc.* , 303, 685
- O'Shea, B. W., Abel, T., Whalen, D., & Norman, M. L. 2005, *Astrophys. J. Lett.* , 628, L5
- Pavlidou, V., & Fields, B. D. 2002, *Astrophys. J. Lett.* , 575, L5
- Peebles, P. J. E., & Dicke, R. H. 1968, *Astrophys. J.* , 154, 891
- Power, C., Navarro, J. F., Jenkins, A., Frenk, C. S., White, S. D. M., Springel, V., Stadel, J., & Quinn, T. 2003, *Mon. Not. R. Astron. Soc.* , 338, 14
- Press, W. H., & Schechter, P. 1974, *Astrophys. J.* , 187, 425

- Primack, J. R. 2003, ArXiv Astrophysics e-prints. [arXiv:astro-ph/0312549](https://arxiv.org/abs/astro-ph/0312549)
- Purcell, E. M., & Field, G. B. 1956, *Astrophys. J.* , 124, 542
- Reif, F. 1965, Fundamentals of Statistical and Thermal Physics (New York, McGraw-Hill, 1965)
- Richstone, D. O., & Tremaine, S. 1984, *Astrophys. J.* , 286, 27
- Ricotti, M. 2003, *Mon. Not. R. Astron. Soc.* , 344, 1237
- Ricotti, M., Gnedin, N. Y., & Shull, J. M. 2001, *Astrophys. J.* , 560, 580
- 2002, *Astrophys. J.* , 575, 49
- Ryu, D., Ostriker, J. P., Kang, H., & Cen, R. 1993, *Astrophys. J.* , 414, 1
- Salamon, M. H., & Stecker, F. W. 1994, *Astrophys. J. Lett.* , 430, L21
- Sand, D. J., Treu, T., Smith, G. P., & Ellis, R. S. 2004, *Astrophys. J.* , 604, 88
- Schaerer, D. 2002, *Astron. Astrophys.* , 382, 28
- 2003, *Astron. Astrophys.* , 397, 527
- Scott, D., & Rees, M. J. 1990, *Mon. Not. R. Astron. Soc.* , 247, 510

- Sedov, L. I. 1959, *Similarity and Dimensional Methods in Mechanics* (Similarity and Dimensional Methods in Mechanics, New York: Academic Press, 1959)
- Shapiro, P. R., Giroux, M. L., & Babul, A. 1994, *Astrophys. J.* , 427, 25
- Shapiro, P. R., Iliev, I. T., & Raga, A. C. 1999, *Mon. Not. R. Astron. Soc.* , 307, 203
- 2004, *Mon. Not. R. Astron. Soc.* , 348, 753
- Shapiro, P. R., & Kang, H. 1987, *Astrophys. J.* , 318, 32
- Shaver, P. A., Windhorst, R. A., Madau, P., & de Bruyn, A. G. 1999, *Astron. Astrophys.* , 345, 380
- Sheth, R. K., & Tormen, G. 2002, *Mon. Not. R. Astron. Soc.* , 329, 61
- Simon, J. D., Bolatto, A. D., Leroy, A., & Blitz, L. 2003, *Astrophys. J.* , 596, 957
- Spergel, D. N., & Steinhardt, P. J. 2000, *Phys. Rev. Lett.* , 84, 3760
- Spergel, D. N., Verde, L., Peiris, H. V., Komatsu, E., Nolta, M. R., Bennett, C. L., Halpern, M., Hinshaw, G., Jarosik, N., Kogut, A., Limon, M., Meyer, S. S., Page, L., Tucker, G. S., Weiland, J. L., Wollack, E., & Wright, E. L. 2003, *Astrophys. J. Suppl. Ser.* , 148, 175
- Stecker, F. W., & Salamon, M. H. 1996, *Astrophys. J.* , 464, 600

- 2001, ArXiv Astrophysics e-prints. [arXiv:astro-ph/0104368](https://arxiv.org/abs/astro-ph/0104368)
- Strigari, L. E., Beacom, J. F., Walker, T. P., & Zhang, P. 2005, *Journal of Cosmology and Astroparticle Physics* (4), 017
- Subramanian, K., Cen, R., & Ostriker, J. P. 2000, *Astrophys. J.* , 538, 528
- Subramanian, K., & Padmanabhan, T. 1993, *Mon. Not. R. Astron. Soc.* , 265, 101
- Swaters, R. A., Madore, B. F., van den Bosch, F. C., & Balcells, M. 2003a, *Astrophys. J.* , 583, 732
- Swaters, R. A., Verheijen, M. A. W., Bershady, M. A., & Andersen, D. R. 2003b, *Astrophys. J. Lett.* , 587, L19
- Tasitsiomi, A., Kravtsov, A. V., Gottlöber, S., & Klypin, A. A. 2004, *Astrophys. J.* , 607, 125
- Taylor, J. E., & Silk, J. 2003, *Mon. Not. R. Astron. Soc.* , 339, 505
- Teyssier, R., Chieze, J., & Alimi, J. 1997, *Astrophys. J.* , 480, 36
- The, L., Leising, M. D., & Clayton, D. D. 1993, *Astrophys. J.* , 403, 32
- Thomas, P. A., Colberg, J. M., Couchman, H. M. P., Efstathiou, G. P., Frenk, C. S., Jenkins, A. R., Nelson, A. H., Hutchings, R. M., Peacock, J. A., Pearce, F. R., & White, S. D. M. 1998, *Mon. Not. R. Astron. Soc.* , 296, 1061

- Thoul, A. A., & Weinberg, D. H. 1995, *Astrophys. J.* , 442, 480
- Tormen, G., Bouchet, F. R., & White, S. D. M. 1997, *Mon. Not. R. Astron. Soc.* , 286, 865
- Tozzi, P., Madau, P., Meiksin, A., & Rees, M. J. 2000, *Astrophys. J.* , 528, 597
- Tumlinson, J., & Shull, J. M. 2000, *Astrophys. J. Lett.* , 528, L65
- Tumlinson, J., Shull, J. M., & Venkatesan, A. 2003, *Astrophys. J.* , 584, 608
- Tyson, J. A., Kochanski, G. P., & dell'Antonio, I. P. 1998, *Astrophys. J. Lett.* , 498, L107
- Ueda, Y., Akiyama, M., Ohta, K., & Miyaji, T. 2003, *Astrophys. J.* , 598, 886
- van den Bosch, F. C. 2002, *Mon. Not. R. Astron. Soc.* , 331, 98
- van den Bosch, F. C., & Swaters, R. A. 2001, *Mon. Not. R. Astron. Soc.* , 325, 1017
- Venkatesan, A., & Truran, J. W. 2003, *Astrophys. J. Lett.* , 594, L1
- Wada, K., & Venkatesan, A. 2003, *Astrophys. J.* , 591, 38
- Watanabe, K., Hartmann, D. H., Leising, M. D., & The, L.-S. 1999, *Astrophys. J.* , 516, 285

- Wechsler, R. H., Bullock, J. S., Primack, J. R., Kravtsov, A. V., & Dekel, A. 2002, *Astrophys. J.* , 568, 52
- Weinberg, M. D., & Katz, N. 2002, *Astrophys. J.* , 580, 627
- Wouthuysen, S. A. 1952, *Astron. J.* , 57, 31
- Yoshida, N., Abel, T., Hernquist, L., & Sugiyama, N. 2003, *Astrophys. J.* , 592, 645
- Yoshida, N., Bromm, V., & Hernquist, L. 2004, *Astrophys. J.* , 605, 579
- Yoshida, N., Springel, V., White, S. D. M., & Tormen, G. 2000a, *Astrophys. J. Lett.* , 535, L103
- 2000b, *Astrophys. J. Lett.* , 544, L87
- Zaldarriaga, M., Furlanetto, S. R., & Hernquist, L. 2004, *Astrophys. J.* , 608, 622
- Zdziarski, A. A. 1996, *Mon. Not. R. Astron. Soc.* , 281, L9
- Zdziarski, A. A., Johnson, W. N., Done, C., Smith, D., & McNaron-Brown, K. 1995, *Astrophys. J. Lett.* , 438, L63
- Zentner, A. R., & Bullock, J. S. 2002, *Phys. Rev. D* , 66, 043003
- Zhang, P., & Beacom, J. F. 2004, *Astrophys. J.* , 614, 37

Index

- 1-D spherical, radiation hydrodynamics code with primordial chemistry network*, 119
- 21cm Background from the Cosmic Dark Ages*, 94
- 511keV Dark Matter and the γ -ray background*, 81
- Abstract, vii
- Acknowledgments*, v
- Appendices*, 159
- Appendix
 - Finite Differencing in the 1-D Spherical*, 162
 - Mass - Wavenumber relation*, 160
- Application*, 60
- Background from Continuum Annihilation Signal*, 83
- Basic equations and problem solving scheme*, 48
- Bibliography*, 185
- Code test*, 132
- Collisionality parameter as a function of σ and M* , 60
- Comparison with N-body simulation results*, 63
- Conclusion/Discussion*, 71
- Conclusions*, 113
- Convergence*, 112
- Dark Matter Annihilation Signal?: Galactic Radiation*, 81
- Dedication*, iv
- Discussion*, 155
- External source*, 126
- Fate of the Neutral Gas After Source Turns Off: Collapse of the Protostellar Region*, 145
- Fate of the Neutral Gas After Source Turns Off: Evolution After Death of the Source*, 153
- Feedback effect during the lifetime of the source*, 137
- Fluid approximation model*, 31
- Fluid approximation of collisionless CDM dynamics*, 9
- Fluid approximation of SIDM halos*, 44
- Fluid Approximation*, 8
- Formation and Evolution of Cold Dark Matter (CDM) Halos*, 3
- Formation of the D-type I-front*, 139
- Gravity*, 120
- Halo Formation by Non-Self-Similar Infall: Mass Assembly History and the Origin of CDM N-body Halo Profiles*, 26
- Halo Formation by Self-Similar Infall*, 17
- Halo formation from peaks of the Gaussian random noise primordial density fluctuations*, 19

Halo formation from scale-free linear perturbations, 17
Halted infall model, 28
heating / cooling, 121
High value of σ : Contradiction with SIDM N-body simulation results?, 69
Hydrodynamic Conservation equations, 119
Hydrogen Molecule Formation in Front of the I-Front, 141

I-front trapping, 137
Importance of cosmological infall, 60
Initial Setup, 133
Internal source, 124
Introduction, 1
Introduction, 35
Introduction, 94, 116

Meaning of the collisionality parameter Q , 57
Missing Gamma Ray Background Problem, 81
Models and initial Conditions, 26

Nature of Dark Matter, 35
Nonequilibrium chemistry, 131
Numerical 21 cm Brightness Temperature from Minihalos vs. IGM, 106
Numerical Simulations, 102

Optically thin limit: case study for initially ionized halo, 136

Physics of 21 cm signal from neutral hydrogen, 97

Radial orbits model, 31
Radiative transfer, 124
Refined Estimate of the Simulated Minihalo 21 cm Signal, 109
Result, 136
Results, 32, 106
Rotation curve fitting, 65

Second-Generation Star Formation In the Early Universe, 116
Self-Interacting Dark Matter, 35
Self-similar halos: an analytical model for CDM N-body results, 20
Self-similar model for SIDM halos in the matter-dominated era, 47
Self-similarity of SIDM halos, 47
Semi-analytic calculations, 99
Semi-Analytical Calculation of the Halo Contribution, 104
Shock jump conditions, 46

The Calculation, 97
The effect of SIDM collisionality, 44
Toward an Analytical Understanding of Cold Dark Matter Halo N-body Simulations, 3

Vita

Kyungjin Ahn was born in Seoul, Korea on 2 Dec 1970, the son of Byungsang Ahn and Jeonghee Hwang. He received the Bachelor of Science degree in Physics from the Pohang University of Science and Technology in 1993. He also served in the Korean Army from May 1994 to Jul 1996. He moved to the United States of America and registered in the physics department of Texas A&M University, where he served as a TA for two years. He moved to Austin to register in the astronomy department of The University of Texas at Austin, where he has served as a TA and a RA. After graduation, he will fill the postdoctoral fellow position for Dr. Paul R. Shapiro.

Permanent address: Dept. of Astronomy, 1 University Station, C1400
Austin, Texas 78712

This dissertation was typeset with \LaTeX^\dagger by the author.

[†] \LaTeX is a document preparation system developed by Leslie Lamport as a special version of Donald Knuth's \TeX Program.